Defect engineering of lead-free ferroelectric ceramics BaTiO3 through acceptor doping

Zechao Li

université PARIS-SACLAY

Defect engineering of lead-free ferroelectric ceramics $BaTiO_3$ through acceptor doping

Ingénierie des défauts des céramiques ferroélectriques sans plomb $BaTiO_3$ par dopage accepteur)

Thèse de doctorat de l'Université Paris-Saclay

École doctorale n° 573 : interfaces : matériaux, systèmes, usages (INTERFACES)
Spécialité de doctorat : Physique
Graduate School : Sciences de l'ingénierie et des systèmes
Référent : CentraleSupélec

Thèse préparée dans le Laboratoire SPMS (Université Paris-Saclay, CNRS), sous la direction de Pierre-Eymeric Janolin, Professeur

Thèse soutenue à Paris-Saclay, le 06 Juillet 2022, par

Zechao LI

Composition du jury

Yves Dumont Professeur, Université Paris-Saclay	Président
Cecile Autret-Lambert Enseignant chercheur, Université de Tours	Rapporteuse & Examinatrice
Julia Glaum Professeure, Norwegian University of Science and Technology (NTNU)	Rapporteuse & Examinatrice
Yves Dumont Professeur, Université Paris-Saclay	Examinateur
Maël Guennou Assistant professor, Université du Luxembourg	Examinateur
Pierre-Eymeric Janolin Professeur, Université Paris-Saclay, CNRS	Directeur ou Directrice de thèse

THESE DE DOCTORAT

NNT : 2022UPAST098

université PARIS-SACLAY | ÉCOLE DOCTORALE Interfaces: matériaux, systèmes, usages

Titre : Ingénierie des défauts des céramiques ferroélectriques sans plomb $BaTiO_3$ par dopage accepteur

Mots clés : Ferroélectriques, Céramiques sans plomb, Dopage, Murs de domaine, Vacances d'oxygène

Résumé : Les ferroélectriques sont célèbres pour leurs multiples propriétés, notamment leur grande permittivité, leur réponse piézoélectrique élevée, leurs propriétés pyroélectriques et optiques, etc. Afin d'améliorer l'application des ferroélectriques dans les applications commerciales et de répondre aux exigences de miniaturisation et aux besoins d'une société respectueuse de l'environnement, le ferroélectrique sans plomb $BaTiO_3$ a été développé intensivement grâce à des efforts de recherche continus dans le monde entier. Une ingénierie microstructurale massive et des modifications chimiques ont été étudiées pour améliorer les propriétés du $BaTiO_3$ ferroélectrique sans plomb. Dans ce travail de thèse, nous introduirons des accepteurs et des vacances d'oxygène pour former des dipôles de défauts, les rotations du domaine ferroélectrique sont contrôlées, ce qui permet de régler les propriétés des céramiques ferroélectriques sans plomb $BaTiO_3$.

Les accepteurs Cu^{2+} and Fe^{3+} sont sélectionnés pour remplacer les ions Ti sur le site B de la structure pérovskite de $BaTiO_3$ par la méthode traditionnelle de synthèse à l'état solide. Les substitutions de Fe et Cu dans $BaTiO_3$ sont démontrées par les spectres EPR. La structure pérovskite des céramiques de $BaTiO_3$ dopées avec une seule phase tétragonale ($P4mm$) à température ambiante est déterminée en combinaison avec les images MEB, les modèles XRD raffinés par Rietveld et les spectres Raman. Les distributions homogènes de Cu sont observées sur les cartes EDX.

Les vacances d'oxygène, soit piégées par les dopants, soit accumulées aux joints de grains, créent un champ électrique interne, jouant un rôle crucial dans le durcissement des ferroélectriques dopés par des accepteurs. Selon ces deux positions de piégeage des vacances d'oxygène, le mécanisme de durcissement est généralement expliqué par l'effet de volume ou l'effet de surface, respectivement. Le résiscope a mesuré la réduction de la résistance de l'intérieur des grains (ΔR_G) et de la limite des grains lorsque le $BaTiO_3$ dopé au Cu à 0,4 at% est devenu relaxé. La réduction plus importante de la résistance à l'intérieur des grains (ΔR_G) que la réduction de la résistance aux limites des grains (ΔR_{GB}) démontre que l'effet de volume est le principal mécanisme de durcissement dans les ferroélectriques polycristallins dopés par un accepteur. Les mouvements des parois de domaines ferroélectriques sont limités par les dipôles de défauts qui sont créés lorsque les vacances d'oxygène atteignent les positions les plus proches des dopants.

Inspirés par cette interaction dipôle-défaut, nous concevons plusieurs stratégies, dont l'excitation thermique et l'excitation de champ, pour contrôler la migration des vacances d'oxygène et manipuler l'orientation des dipôles de défauts. Par conséquent, les mouvements des parois des domaines sont contrôlés, ce qui fait que les $BaTiO_3$ dopés par l'accepteur présentent différentes boucles d'hystérésis, y compris le processus de vieillissement, le processus de re-vieillissement et le processus de décalage.

Grâce aux calculs DFT, la barrière d'énergie la plus faible du mouvement des vacances d'oxygène suite à la polarisation spontanée des céramiques $BaTiO_3$ dopées par un accepteur rhomboédrique est établie. Ce résultat est cohérent avec le principe de conformité à la symétrie des défauts ponctuels. En outre, les barrières énergétiques de diffusion des vacances d'oxygène dans la céramique $BaTiO_3$ dopée au fer sont plus faibles que dans la céramique $BaTiO_3$ dopée au cuivre, ce qui indique une plus grande mobilité des vacances d'oxygène dans la céramique $BaTiO_3$ dopée au fer. Ces résultats de calcul DFT sont étayés par deux expériences : une mesure de refroidissement par champ et une mesure de fatigue.

Title : Defect engineering of lead-free ferroelectric ceramics $BaTiO_3$ through acceptor doping
Keywords : Ferroelectrics, Lead-free ceramics, Doping, Domain walls, Oxygen vacancies

Abstract :

Ferroelectrics are famous for their multiple properties, including large permittivity, high piezoelectric response, pyroelectric, and optical properties, and so on. To make ferroelectrics better applied in commercial applications and meet miniaturization requirements and needs of an environment-friendly society, lead-free ferroelectric $BaTiO_3$ has been intensively developed through a continuous worldwide research efforts. Massive microstructural engineering and chemical modifications have been investigated to enhance the properties of lead-free ferroelectric $BaTiO_3$. In this PhD work, we shall introduce acceptors and oxygen vacancies to form defect dipoles, the ferroelectric domain rotations are controlled, which enables tuning the properties of lead-free ferroelectric $BaTiO_3$ ceramics.

The acceptors Cu^{2+} and Fe^{3+} are selected to substitute for the Ti ions on the B site of the perovskite structure of $BaTiO_3$ through traditional solid-state synthesis method. The Fe and Cu substitutions in $BaTiO_3$ are demonstrated by the EPR spectra. Combined with the SEM images, Rietveld-refined XRD patterns, and Raman spectra, the perovskite structure of doped $BaTiO_3$ ceramics with a single tetragonal phase ($P4mm$) at room temperature are determined. The homogeneous Cu distributions are observed on the EDX maps.

The oxygen vacancies, either trapped by dopants or accumulated at grain boundaries, create an internal electric field, playing a crucial role to harden acceptor-doped ferroelectrics. According to these two trapping positions for the oxygen vancancies, the hardening mechanism is generally explained by the volume effect or the surface effect, respectively. Resiscope measured the resistance reduction of the interior of the grains (ΔR_G) and grain boundary when hardened 0.4 at%Cu-coped $BaTiO_3$ became the relaxed. The higher reduction of the interior of the grains resistance (ΔR_G) than the reduction of grain boundary resistance (ΔR_{GB}) demonstrates that the volume effect is the principal hardening mechanism in polycrystalline acceptor-doped ferroelectrics. The movements of ferroelectric domain walls are restricted by the defect dipoles that are created as oxygen vacancies reach positions nearest-neighbor to dopants.

Inspired by this defect dipole-domain interaction, we design several strategies including thermal and field excitation to control the oxygen vacancies migration, and manipulate the orientation of defect dipoles. Consequently, the domain walls movements are controlled, which makes the acceptor-doped $BaTiO_3$ present different hysteresis loops, including de-aging process, re-aging process, shifting process.

Through DFT calculations, the lowest energy barrier of oxygen vacancies movement following the spontaneous polarization of rhombohedral acceptor doped $BaTiO_3$ ceramics is established. This result is consistent with the symmetry-conforming principle of point defects. In addition, the lower energy barriers of oxygen vacancies diffusion in Fe-doped $BaTiO_3$ than in Cu-doped $BaTiO_3$ are calculated, which indicates the higher mobility of oxygen vacancies in Fe-doped $BaTiO_3$. These DFT calculation results are backed up by two experiments : field cooling measurement and fatigue measurement.

PUBLISHED BY CENTRALESUPÉLEC

Université Paris-Saclay, CNRS, CentraleSupélec, Laboratoire SPMS, 91190, Gif-sur-Yvette, France.
First printing, May 2022

Acknowledgement

It is this time. In this almost four-year work, with laughter and tears, I have met so many people along the way, and I have learned so much from all of them. This thesis work has been kept on track and has been seen through to completion with their support and encouragement. Here, I would like to express my sincere gratitude to them, including my parents, my girlfriend, my friends, colleagues, and various institutions.

Foremost, I would like to express my sincere gratitude to my advisor Prof. Pierre-Eymeric JANOLIN for the continuous support of my PhD study and research, and for his patience, motivation, enthusiasm, and immense knowledge. He showed me the way forward. Through all the meetings and brainstorming sessions we had together, he taught me how to be an outstanding researcher. He also introduced me to many excellent labs, professors, and researchers. From the bottom of my heart, I am grateful to have him as my mentor. I could not have imagined having a better advisor and mentor for my academic study.

Besides my advisor, I am deeply grateful to the rest of my thesis committee, for their encouragement, insightful comments, and hard questions.

I am extremely thankful to the China Scholarship Council (CSC) for awarding me the scholarship and providing me with the financial support to complete this work.

My sincere thanks also go to Dr. Brahim Dkhil, and Dr. Guilhem Dezanneau. Thank you for teaching me various physics knowledge and for offering me summer school, winter school, and conference opportunities.

I owe my profound thankfulness to Prof. Pascal Chrétien, Dr. Mariana Stefan, Dr. Cecile Autret, and Prof. Jun KANO, who gave me access to the laboratories and research facilities and provided assistance for the majority of my PhD work. Without their precious support, it would not be possible to conduct my research.

I am fortunate to have been a part of the SPMS. I wish to express my warm and sincere thanks to every colleague in the lab: Dr. Charles Paillard, Dr. Maxime Vallet, Dr. Eva Heripre, Pascale Gemeiner, Omar Ibder, Fabienne Karolak, Chengyi Li, Xianwu Jiang, Hainan Liu, Jiacheng Yu, Shenglan Hao, Minghai Yao, Long Cheng, Jingye Zou, Gaëlle Vitali-Derrien, Moazzam Milad, Sabri Houssam, etc, for the valuable knowledge and experience they shared with me, for the experiments supports and discussions, and for all the fun we have had in the last four years. It was great sharing the laboratory with all of you during the last four years.

In addition, my heartfelt thanks to my forever interested, encouraging, and always enthusiastic parents and my little sister, they are always keen to know what I was doing and how I am proceeding, although it is likely that they have never grasped what it is all about! Even though we could not see each other for quite some time due to the pandemic, they always make sure I know how proud they

are of me.

A happy life is a key to success and at this juncture my special thanks to my beloved girlfriend: Siyang Liu, who offers unstinting love, support, and encouragement. Without her, I could not have completed this work.

We can always find something to be thankful for, and here is a big one for which I still feel words were too insufficient to express the complete indebtedness I owe to each individual I have mentioned here and also to whom I have failed to mention by error.

Introduction

Ferroelectric materials are famous for their switchable spontaneous polarization. Besides, they also display large permittivity, high piezoelectric response, pyroelectric, and optical properties. Therefore, ferroelectric materials are abundantly applied in commercial applications. In order to meet miniaturization requirements and needs of environment-friendly society, lead-free ferroelectric $BaTiO_3$ has been intensively developed through a continuous worldwide research efforts. Massive microstructural engineering and chemical modifications have been investigated to enhance the properties of lead-free ferroelectric $BaTiO_3$. In this PhD work, we shall introduce the defect engineering tuning the properties of $BaTiO_3$. By manipulating the migration of oxygen vacancies to align defect dipoles in ferroelectrics, the movements of domain walls are controlled. This enables ferroelectrics performances satisfying the various functional applications. Parts of this work have been published in a review (Refs.[1]), as shown in the Appendices.

The oxygen vacancies are induced in $BaTiO_3$ through acceptor doping. The Cu and Fe ions are chosen as acceptors. Acceptor doping is one of the promising method for tailoring the properties of ferroelectrics. Compared with generic microstructural engineering methods, acceptor doping modifications has simplicity and lower cost. Compared with other chemical modifications, acceptor doping has less modification to the structure and higher controllability of domain walls. These advantages of acceptor doping are demonstrated by measuring structures and properties of Cu-doped and Fe-doped $BaTiO_3$ ceramics, which is shown in Chapter 2.

As oxygen vacancies reach positions nearest-neighbor to dopants, defect dipoles inevitably form. These defect dipoles act as internal bias electric fields restricting the surrounding domains reorientation, hardening $BaTiO_3$ ceramics. This hardening mechanism is decided by the volume effect that is identified in Cu-doped and Fe-doped $BaTiO_3$ ceramics through Resiscope measurement, which is shown in Chapter 3.

Combining volume effect and the symmetry-conforming principle of point defects, the defect dipoles-domains interaction can be clearly understood. Thus, we design several strategies including thermal and field excitations to manipulate the movement of oxygen vacancies, aligning defect dipoles. As a consequence, the movements of ferroelectric domain walls are controlled, which is reflected in different hysteresis loop shapes. This is detailed in Chapter 4.

The defect dipoles can disappear as oxygen vacancies leave the immediate vicinity of the dopants. Consequently, control of the ferroelectric domains will be lost. Hence, the lifetime of defect dipoles has to be considered for engineering properties of acceptor-doped ferroelectrics. In Chapter 5, the experiments backed up by DFT calculations are carried out to investigate the mobility of oxygen vacancies, enabling to compare the lifetime of defect dipoles in Cu-doped and Fe-doped $BaTiO_3$ ceramics.

Introduction (en français)

Les matériaux ferroélectriques sont célèbres pour leur polarisation spontanée commutable. En outre, ils présentent également une grande permittivité, une réponse piézoélectrique élevée, des propriétés pyroélectriques et optiques. Par conséquent, les matériaux ferroélectriques sont abondamment utilisés dans les applications commerciales. Afin de répondre aux exigences de miniaturisation et aux besoins d'une société respectueuse de l'environnement, le $BaTiO_3$ ferroélectrique sans plomb a été développé intensivement grâce à des efforts de recherche continus dans le monde entier. Une ingénierie microstructurale massive et des modifications chimiques ont été étudiées pour améliorer les propriétés du $BaTiO_3$ ferroélectrique sans plomb. Dans ce travail de thèse, nous présenterons l'ingénierie des défauts qui permet de régler les propriétés du $BaTiO_3$. En manipulant la migration des lacunes d'oxygène pour aligner les dipôles des défauts dans les ferroélectriques, les mouvements des parois de domaine sont contrôlés. Cela permet d'obtenir des performances ferroélectriques satisfaisant les diverses applications fonctionnelles. Des parties de ce travail ont été publiées dans une revue (Refs.[1]), comme indiqué dans les annexes.

Les vacances d'oxygène sont induites dans le $BaTiO_3$ par le dopage des accepteurs. Les ions Cu et Fe sont choisis comme accepteurs. Le dopage d'accepteur est une des méthodes prometteuses pour adapter les propriétés des ferroélectriques. Par rapport aux méthodes génériques d'ingénierie microstructurale, les modifications par dopage d'accepteur sont simples et moins coûteuses. Par rapport à d'autres modifications chimiques, le dopage des accepteurs modifie moins la structure et permet de mieux contrôler les parois des domaines. Ces avantages du dopage accepteur sont démontrés en mesurant les structures et les propriétés des céramiques $BaTiO_3$ dopées au Cu et au Fe, comme le montre le chapitre 2.

Lorsque les vacances d'oxygène atteignent les positions les plus proches des dopants, des dipôles de défauts se forment inévitablement. Ces dipôles de défauts agissent comme des champs électriques de polarisation interne qui limitent la réorientation des domaines environnants, durcissant ainsi les céramiques de $BaTiO_3$. Ce mécanisme de durcissement est déterminé par l'effet de volume qui est identifié dans les céramiques $BaTiO_3$ dopées au cuivre et au fer par la mesure du résiscope, comme le montre le chapitre 3.

En combinant l'effet de volume et le principe de symétrie-conformité des défauts ponctuels, l'interaction dipôles-domaines des défauts peut être clairement comprise. Ainsi, nous concevons plusieurs stratégies incluant des excitations thermiques et de champ pour manipuler le mouvement des vacances d'oxygène, alignant les dipôles de défauts. En conséquence, les mouvements des parois des domaines ferroélectriques sont contrôlés, ce qui se traduit par différentes formes de boucles d'hystérésis. Ce point est détaillé au chapitre 4.

Les dipôles des défauts peuvent disparaître lorsque les vacances d'oxygène quittent le voisinage

immédiat des dopants. Par conséquent, le contrôle des domaines ferroélectriques sera perdu. Par conséquent, la durée de vie des dipôles de défauts doit être prise en compte pour les propriétés techniques des ferroélectriques dopés par des accepteurs. Dans le chapitre 5, les expériences soutenues par des calculs DFT sont effectuées pour étudier la mobilité des vacances d'oxygène, permettant de comparer la durée de vie des dipôles de défaut dans les céramiques $BaTiO_3$ dopées au Cu et au Fe.

Contents

1. Basics of ferroelectrics

In this PhD work, the properties of lead-free ferroelecric $BaTiO_3$ are successfully engineered by controlling the orientation of defect dipoles. Before analyzing how it works and showing properties changes, we shall briefly introduce the basics of lead-free ferroelecric $BaTiO_3$ ceramics, including structure, properties, commerical applications, and common property modification methods.

1.1 Ferroelectric materials and their hysteresis loops

1.1.1 Ferroelectrics

The ferroelectric materials, first produced in 1935 by Bush and Scherrer[2], have attracted intensive attention due to their various properties. As a subset of dielectrics, ferroelectrics not only have large permittivity and high piezoelectric response, but also show pyroelectric, electrocaloric, and optical properties. Importantly, they are characterized by a spontaneous polarization that can be switched reversibly between at least two different stable orientations under the application of an electric field.[2, 3, 4, 5] Consequently, ferroelectric materials are exploited in a large number of devices and components, such as resonators, transducers, sensors, actuators, and capacitors.[3, 6, 7, 8, 9] The common ferroelectric materials include lead zirconate titanate ($PbZr_{1-x}Ti_xO_3$, PZT), lead lanthanum zirconate titanate ($Pb_{1-3y}La_{2y}Zr_{1-x}Ti_xO_3$ or $Pb_{1-y}La_y(Zr_{1-x}Ti_x)_{1-0.25y}O_3$), and barium titanate ($BaTiO_3$, BTO or BT). Among them, $BaTiO_3$-based materials have been the focus of intense in scientific research and application fields as it is environmentally friendly (*i.e.* non lead contaminating materials).[2]

In my PhD work, the $BaTiO_3$ ceramics have been chosen. $BaTiO_3$ adopts the perovskite-type (ABO_3) structure, as shown in Figure.1.1. The Ba^{2+} cation occupies the *A* site at the corners of the perovskite unit cell and each *A*-site cation is 12-fold coordinated with the oxygen anions. At the center of the cell (on the *B* site), the Ti^{4+} is surrounded by an oxygen octahedron (6-fold coordination).

At high temperatures (above the Curie temperature T_C), $BaTiO_3$ is paraelectric with a centrosymmetric cubic symmetry ($Pm\bar{3}m$). It undergoes a series of structural phase transitions to ferroelectric phases: first to a tetragonal ($P4mm$) at T_C=395 K, then to an orthorhombic ($Amm2$) phase at T_{T-O}=280 K and finally to a rhombohedral ($R3m$) phase at 185 K[2, 4] (see Figure.1.2). The phase transitions of $BaTiO_3$ are mostly displacive and have been interpreted as a displacement of Ti cations relative to O_6 cage, which directly gives rise to the spontaneous polarization ($\mathbf{P}_s$).[10, 11]

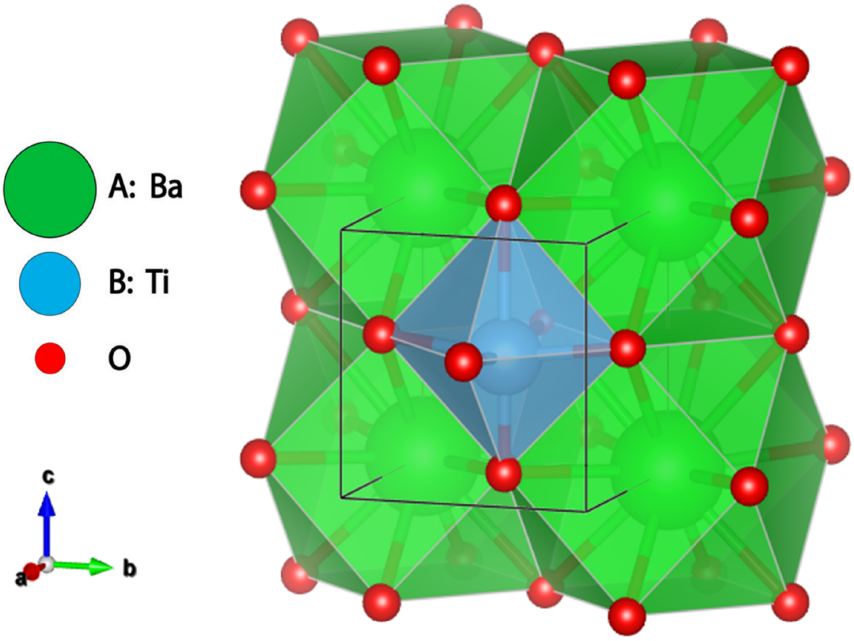

Figure 1.1: Perovskite structure of $BaTiO_3$, A cation (Ba^{2+}) sits at the corners of the cube and B cations (Ti^{4+}) are surrounded by the oxygen octahedron in the center of the cube.

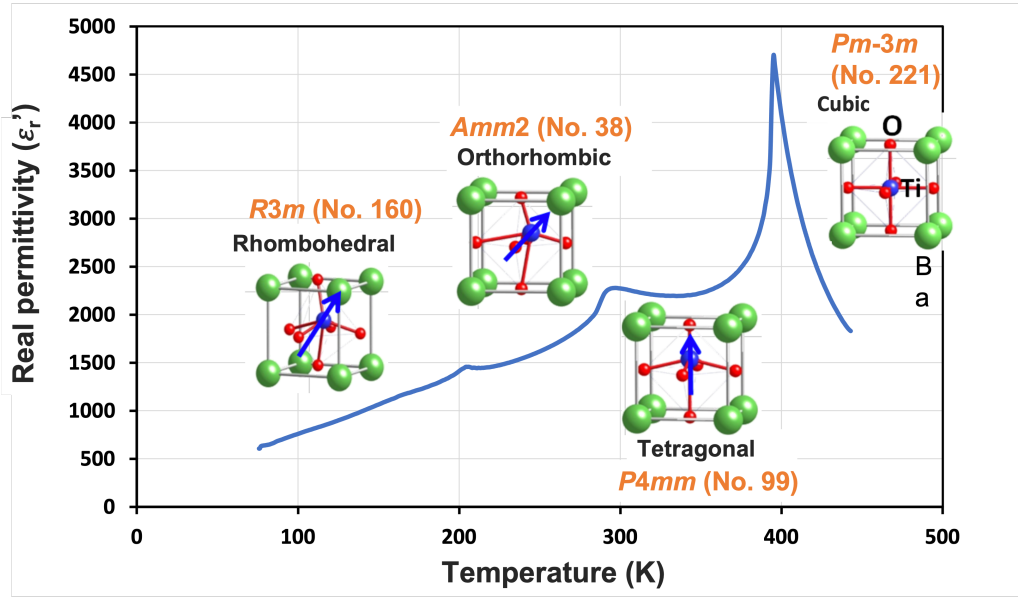

Figure 1.2: The real part of the relative permittivity of $BaTiO_3$ ceramic as a function of temperature. The insets depict the unit cell, its space groups, and crystalline systems together with a representation of the polarization direction (blue arrows). The solid-state-solution-synthesized sample was measured through heating and cooling at 1 °C min^{-1} in cyrofurnace. The impedance analyzer (Agilent 4294A) was applied with 500 mV of oscillation amplitude from 40 to 1.1 MHz.

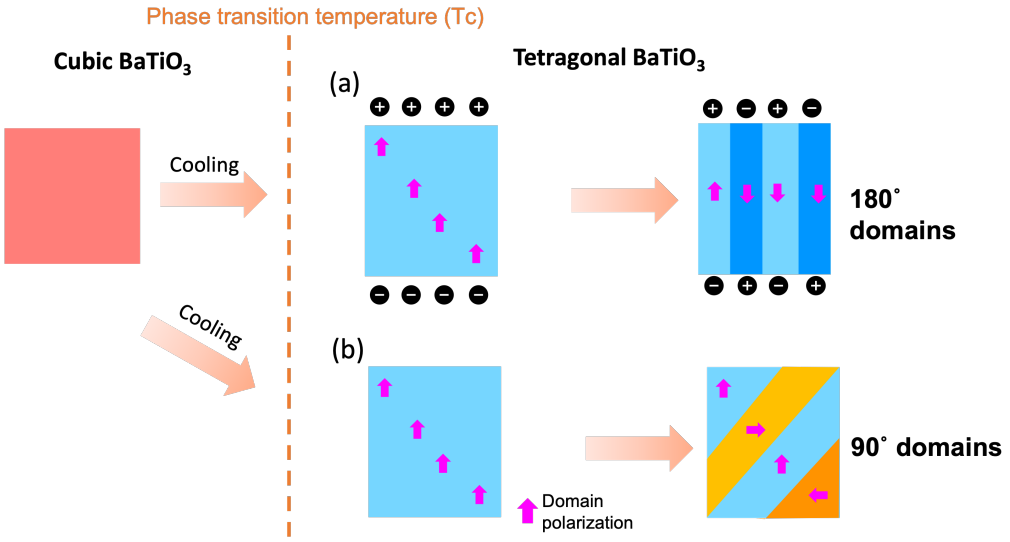

Figure 1.3: Schematic of the formation of 180° (a) and 90° (b) domain in $BaTiO_3$. Cooling below the phase transition temperature, the spontaneous polarisation (pink arrows) of $BaTiO_3$ induces surface charges which cause a depolarizing field. As a result, 180°-domains with opposite polarisation are created to minimize the corresponding electrostatic energy; (b) Simultaneously, 90° domains are created to minimize the mechanical stresses caused by the phase transition.

If some spontaneous polarizations have uniform direction in one local region, this region is called ferroelectric domain. Domain walls separate domains with different orientation of the polarization. In $BaTiO_3$, the 180° and 90° domain walls are always formed as cooling through paraelectric-ferroelectric phase transition to minimize the depolarizing electric field and elastic energy[2, 12, 10], as shown in Figure.1.3

1.1.2 The ferroelectric hysteresis loop, a consequence of domain-walls movements

In response to the electric-field activation, the domains can appear, change the size, rotate, or disappear. These changes correspond to the movements of domain walls.[13] As a consequence, these movements cause changes in the polarization of the ceramcis. The hysteresis loops reveal this polarization-applied electrical field relationship in ferroelectric materials. Figure.1.4 shows the hysteresis loop of pure $BaTiO_3$ ceramics with schematics of the corresponding domains arrangements.

After sintering, $BaTiO_3$ ceramics exhibit a zero net polarization (state 1: "virgin" state) due to the random orientation of the ferroelectric domains. Upon the increasing external electric field, domains gradually align through domain walls movement. This process is also called poling. The polarisation gradually increases and then saturates (up to P_s) under high fields (state 2: polarised state). Upon removal of the external field, not all domains switch back to their original orientation, resulting in a remanent polarization (P_r) in the ceramic (state 3 with remanent polarisation P_r^+). At the negative coercive field (E_c^-), the orientations of the domains cancel each other. Under the opposite external electric field, the domains are aligned again, resulting in polarization reversal.

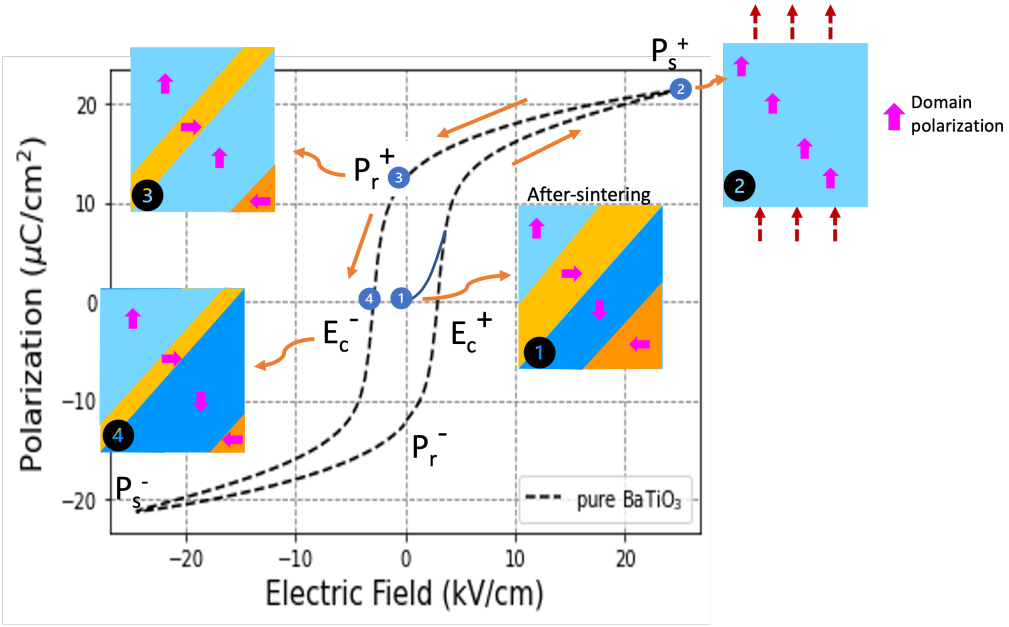

Figure 1.4: Hysteresis loop of pure $BaTiO_3$ at room temperature with corresponding orientations of domain polarization (pink arrows). The initially randomly oriented domains are gradually aligned by the increasing external electric field. $BaTiO_3$ goes from state 1 ("virgin" state) to state 2 (polarized state). Under removal of the field, dipoles partially switch back (state 3 with remanent polarization P_r^+). At the coercive field (E_c^-) the orientations of the dipoles cancel each other. The loop was measured by a Piezoelectric Evaluation System (TF analyzer 2000E with FE-mode, AixAcct) without prepolarization and leakage compensation. The sample pasted by silver was immersed in silicon oil during the test to prevent flashover. A sinusoidal electric field with 5 Hz of frequency was applied.

The different domain-walls movements in ferroelectrics shall induce various polarization switching by electric field.[14, 15, 16, 17, 18] As a result, a variety of hysteresis loops are presented.[19] A slim and sharp hysteresis loop with small P_r and E_c is obtained when the domain becomes mobile and highly responsive to the applied electric field.[20, 21, 22] If domain-walls movements are restricted , a slanted hysteresis loop with large hysteresis is shown.[4] When all the domains are aligned along a single direction, a large electric field along to the opposite direction is needed to switch domains, leading a shifted hysteresis loop with asymmetric E_c 's.[4, 23] More different scenarios of the hysteresis loop are summarised by Schenk, T., *et al.*[19]. We shall display the transformation of hysteresis loop between different shapes by controlling domain walls movement in Chapter 4, such as from pinched to open and from open to humming-bird shape.

1.2 Tailoring ferroelectric hysteresis loop for applications

1.2.1 Energy storage

The development of efficient and reliable electrical energy storage solutions is a major scientific and industrial challenge, considering the growth of both the digital economy and the world population.[24] High energy storage devices would further promote the integration of lightweight miniaturized electronic and electrical systems. Dielectric capacitors, which are one of the major electrical storage technologies, have higher power density and faster charge/discharge time than chemical energy storage devices (batteries), solid oxide fuel cells (SOFCs), or superconducting magnetic energy storage (SMES) systems.[7, 25, 8]

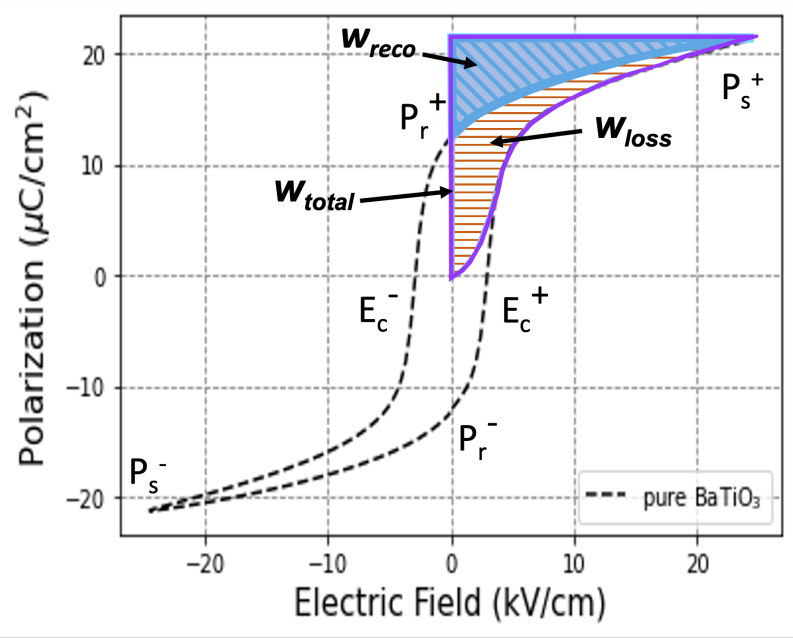

Figure 1.5: Diagram of energy storage density in pure $BaTiO_3$ According to Equation.1.1 and 1.2, the stored energy in ferroelectrics can be obtained by numerical integration of the area between the polarization and the hysteresis loops. The area decorated by diagonal stripes represents the recoverable energy (W_{reco}), the area decorated by transverse stripes is energy loss (W_{loss}) that are used in the polarisation process of the ceramic. The area boxed by violet curve is total energy (W_{total}). It is obvious that if the remanent polarization of ferroelectric could be decreased while maintaining a high saturation polarization, the recoverable energy storage density can be increased. The loop of pure $BaTiO_3$ was measured by a Piezoelectric Evaluation System (TF analyzer 2000E with FE-mode, AixAcct) without prepolarization and leakage compensation. The sample pasted by silver was immersed in silicon oil during the test to prevent flashover. A sinusoidal electric field with 5 Hz of frequency was applied.

$$W_{\text{total}} = \int_0^{P_s} E \cdot \mathrm{d}P \tag{1.1}$$

$$W_{\text{reco}} = \int_{P_r}^{P_s} E \cdot \mathrm{d}P \tag{1.2}$$

Where E is the external applied electrical field, W_{total} is the total energy storage density, and W_{reco} is the recoverable energy storage density.

According to Equation.1.1 and 1.2, the stored energy in ferroelectrics can be easily obtained by numerical integration of the area between the polarization and the hysteresis loops.[26, 8] As shown in Figure.1.5, the area decorated by diagonal stripes represents the recoverable energy (W_{reco}). It corresponds to the total electric energy (W_{total}, boxed by violet curve) brought to the system minus the part used in the polarisation process of the ceramic (W_{loss}, decorated by transverse stripes), represented by the solid blue area inside the hysteresis loop. In the family of bulk dielectric ceramics, ferroelectrics exhibit higher permittivity and polarization values than paraelectrics, and higher breakdown strength than relaxors and antiferroelectrics.[10, 27] However, due to the larger remanent polarization, ferroelectrics have a smaller recoverable energy storage density than other dielectric ceramics[8], including relaxors, anti-ferroelectrics, and linear dielectrics. This disadvantage has

delayed the more widespread use of ferroelectrics.[7] Nevertheless, if the remanent polarization of ferroelectric could be decreased while maintaining a high saturation polarization and high breakdown field, the resulting high energy storage density would widen the applicative prospects of ferroelectrics.[16] We shall see in Chapter 4 that the recoverable energy density (W_{reco}) of $BaTiO_3$ can be increased more than 50% by using the field-excitation strategy.

1.2.2 Sensor, actuator, and transducer

Due to the large piezoelectric response, ferroelectrics are widely used for piezoelectric applications, including sensors, actuators, and transducers.[10] In the ferroelectric materials family, $BaTiO_3$ was first used as a piezoceramic in the 1950s. The piezoelectric coefficient (d_{33}) of $BaTiO_3$ ceramics is 190 pm V^{-1}.[28] However, $BaTiO_3$ ceramics were soon superseded by PZT-based ceramics, which possess a better piezoelectric coefficient (d_{33} from 152 to 590), a wider temperature application range, and higher thermal stability.[29, 30, 31] After decades of the continuous research and development efforts, the piezoelectric properties of $BaTiO_3$-based materials have been drastically improved through using chemical modification and/or microstructural engineering, such as d_{33} of 1250 pm V^{-1} in Cu and W doped $Ba_{0.85}Ca_{0.15}Zr_{0.1}Ti_{0.9}O_3$(BZT-50BCT)[32].

1.2.3 Nonvolatile memory

Bistable polarization of ferroelectrics enables them to be promising candidates for memory applications.[2, 33] The Ferroelectric random access memory (FeRAM) as an alternative for flash memory has lots of advantages, including lower power usage and a much greater maximum number of read-write cycles.[33] Each read operation destroys the current memory state and needs to be followed by a write operation to write the bit back to original state. Lowering the coercive filed (E_c) can make a quick polarization reorientation, resulting in improving read-write performance. However, the low storage density of ferroelectrics limits the information recording capability of FeRAM.

In addition, ferroelectric domain walls movements have a one-to-one correlation with the their charge state. Therefore, a continuous set of resistance states can be realized by changing the inclination angle of domains relative to the polarization direction, which can be used as multilevel data storage.[13]

1.2.4 Other applications

Besides the applications above, ferroelectrics are also proposed to be applied as thermistors and electro-optic devices which include displays, light deflectors, and modulators. The optical properties of ferroelectrics depend on the direction of the remanent polarization. The differences in remanent polarization states enable the material to extinguish or transmit light, functioning as different optical devices.[33, 34] Through introduction of oxygen vacancies or electrons, ferroelectric materials can exhibit variation in electrical conductivity as a function of temperature. This electrical behavior enables ferroelectric material to be applied both as positive[35] as well as negative temperature coefficient thermistors.[36]

1.3 Methods for tailoring the hysteresis loop

According to the short summary of ferroelectrics applications above, the importance of hysteresis loop parameters is underlined. These parameters include remanent polarization (P_r), saturation polarization (P_s), and coercive field (E_c). These parameters are highly dependent on the crystal symmetry, domain walls movement, grain boundary condition, and defect chemistry. Many strategies classified into microstructural engineering and chemical modifications are inspired by these factors to tune ferroelectric hysteresis loops. The generic microstructural engineering includes adjusting grain and domain size, texturing, and core-shell composite approaches.[37, 38,

39] The chemical modifications include the design of solid solutions and doping.[40, 10] Compared with microstructural engineering, chemical modifications are the most used approach due to their simplicity and lower cost.[29]

The distinction has to be made between solid-solution-modified ferroelectrics from *M*-doped ferroelectrics based on whether the *M*-based compound can adopt the structure of the initial ferroelectrics. For example, if $MTiO_3$ (e.g. $SrTiO_3$) or $BaMO_3$ (e.g. $BaZrO_3$) form a stable perovskite, then a solid solution is usually formed. On the contrary, if $MTiO_3$ or $BaMO_3$ do not form a stable perovskite phase, then there is a maximum amount of *M* that can be introduced in the perovskite structure of $BaTiO_3$ (usually a few atomic percent). The resulting compounds constitute the *M*-doped $BaTiO_3$ that are the topic of this PhD work.

1.3.1 Solid solution

Solid solution are generally formed by isovalent substitutions on either the *A* or *B* site of the perovskite. This kind of isovalent substitution can be predicted based on the Goldschmidt tolerance factor and the octahedral factor.[41] The common ions for substituting $BaTiO_3$ on the A site are Sr^{2+} and Ca^{2+}. The Zr^{4+}, Hf^{4+} and Sn^{4+} are generally used for the B-site isovalent substitutions. Within the solid solution, appropriate compounds of different symmetry are chosen to create the pseudo-binary system, pseudo-ternary, or pseudo-quaternary system, such as $BaTiO_3$–$x$$CaTiO_3$[42] and $BaTiO_3$–$x$$SrTiO_3$[43]. The phase transition line in these systems driven by varying the composition is termed a morphotropic phase boundary (MPB)[44, 45], whereas the phase transition line occurring as a result of changes in other thermodynamic variables is termed a polymorphic phase boundary (PPB)[29]. Near these boundaries, the vanishing of the polarization anisotrop and a drastic decrease in domain wall energy can generate adaptive ferroelectric domain states, increasing the dielectric permittivity and piezoelectric response as a result.[46] The disadvantage of solid solution is their complex structures.[45] The complex structures of the material increase the difficulty in understanding the structure-property mechanism, which limits the use of the ferroelectric materials. Hence, we turned our goal to the another chemical modification method to control the hysteresis loop of ferroelectrics: doping.

1.3.2 Doping

Substitutional aliovalent (a.k.a heterovalent) doping is the intentional introduction of dopants with a different valence than the ion they substitute in the base material. The common dopants for $BaTiO_3$ and their valence are shown by green stars (*A*-site doping) and blue circles (*B*-site doping) in Figure.1.6. Aliovalent dopants can be more or less positively charged than the host ion, therefore defining donors or acceptors respectively. Fe ions are common acceptor for doping $BaTiO_3$ and Fe-doped $BaTiO_3$ has been heavily investigated.[47, 48, 49] The Cu ions are selected as acceptor of $BaTiO_3$ in this PhD work for their stable 2+ valence, especially in an octahedral environment. The positions of Cu and Fe substitutions and the effects on the $BaTiO_3$ structure shall be discussed in Chapter 2.

Donor doping improves the mobility of domain walls, and ferroelectrics are consequently "softened". The "softening" mechanism of is ascribed to the reduced internal stress caused by Ba or Ti vacancies and to electron transfer between Ba and Ti vacancies.[10, 51, 52, 53, 54] Therefore, donor-doped ferroelectrics have high permittivity and piezoelectric coefficients.[55, 56] Slimmer hysteresis loops with lower coercive fields are measured, which contributes to increasing the energy storage performance.[51, 53] The problem of donor doping is that the primary charge compensation mechanism in donor-doped ferroelectrics (Ba vacancies, Ti vacancies, free electrons, changes of valence state of Ti ions...)[57, 58, 59] remains as well an open question[60]. This problem makes precise control of domain walls mobility difficult. As a result, the hysteresis loop of donor-doped ferroelectrics can not have the customized morphologies according to the target application. Thereby, we chose the acceptor doping to engineer the properties of ferroelectrics.

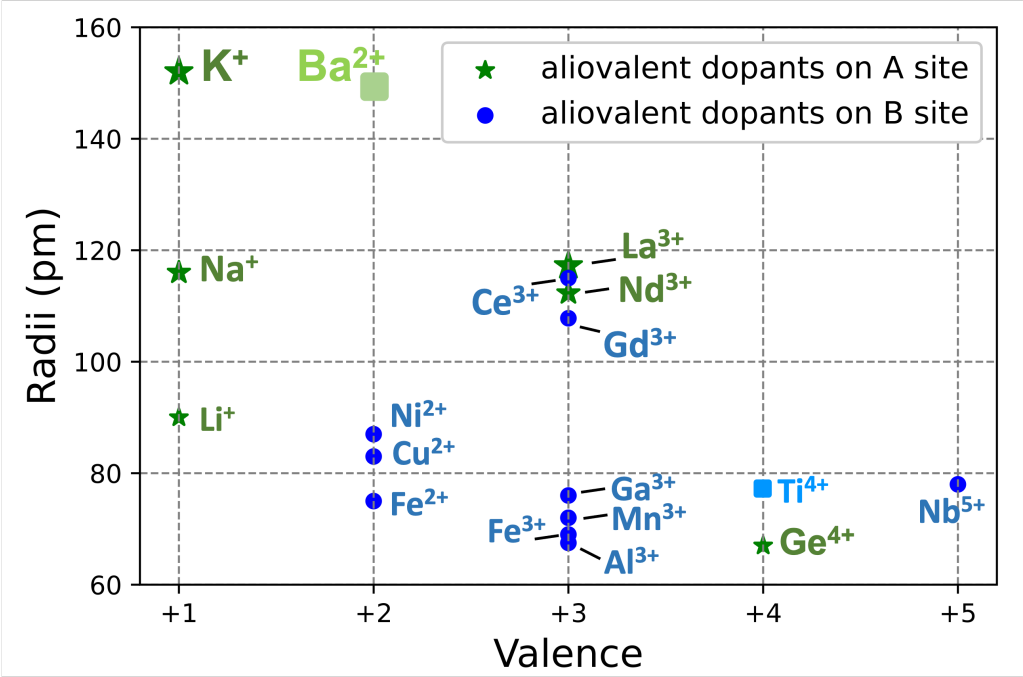

Figure 1.6: The radii[50] and radii of common dopants for $BaTiO_3$. Square symbols present the host ions (Ba^{2+} and Ti^{4+}) and the aliovalent dopants for the *A* site (coordination 12) and *B* site (coordination 6) of $BaTiO_3$ are shown by green stars and blue circles, respectively.

Through acceptor doping, the positively charged oxygen vacancies (($V_O^{\bullet\bullet}$)) are induced in ferroelectric to keep charge neutrality.[61, 62, 63, 64] These oxygen vacancies create internal electric fields, hindering the movement of the surrounding domain walls, and leading to ferroelectrics becoming "hard"[4]. During the polarization switching process, the internal electric fields created by oxygen vacancies act as a restoring force increasing the domain walls mobility during the removal of the applied external field. Hence, because of the oxygen vacancies-domains interaction, we achieve the manipulation of ferroelectric hysteresis loop through acceptor doping.

The oxygen vacancies-domains interaction (hardening mechanism) is generally explained by two main models: the volume effect and surface effect. The volume effect attributes the stabilization of the domain structure to the oxygen vacancies,[65] accompanying acceptor doping through the formation of defect dipoles (*M*-$V_O^{\bullet\bullet}$-Ti).[17] These dipoles act as an internal bias field that pins the domains and therefore stiffens the walls.[66, 23, 67] According to the symmetry-conforming principle of point defects, the orientation of defect dipoles conform to the surrounding domains polarization at thermodynamic equilibrium.[68, 69] With oxygen vacancies hopping between neighboring positions next to dopants, defect dipoles achieve reorientation.[70, 61] The surface effect postulates on the contrary that the oxygen vacancies move to the domain walls or grain boundaries to compensate for the spontaneous polarization discontinuities. Consequently, the accumulation of oxygen vacancies leads to internal electric fields fixing the domain walls.[23, 71, 72] We shall use local resistance measurement (Resiscope) to detect the oxygen vacancies distribution, identifying the principal hardening mechanism in acceptor-doped ferroelectrics in Chapter 3.

1.4 Summary

Summary 1 Ferroelectric materials not only have large permittivity and high piezoelectric

response, but also show pyroelectric, electrocaloric, and optical properties. Importantly, ferroelectrics are famous for their spontaneous polarization that can be switched reversibly between at least two different stable orientations under the application of an electric field. Therefore, ferroelectric materials are applied in a variety of fields, including energy storage, energy harvesting, information memory, piezoelectric sensor, electro-optic devices, and so on. The key factor affecting ferroelectrics performance is the movement of domain walls. The domain walls are formed when cooling ferroelectrics through paraelectric-ferroelectric phase transition to minimize the depolarizing electric field and elastic energy. In response to the external electric-field activation, different domain-walls movements in ferroelectrics shall induce various polarization-switching processes, resulting in changes of hysteresis loop, permittivity, and piezoelectric coefficients. The functional applications of ferroelectrics are consequently affected. Thus, manipulation of the properties of ferroelectrics can be achieved through the control of domain walls movement.

Among the abundant methods for tuning ferroelectric properties, acceptor doping is one of chemical modifications that has simplicity and lower cost, compared with generic microstructural engineering methods. Compared with other chemical modifications such as the design of solid solutions and donor doping, acceptor doping has less impact on to the structure of the base materials and higher controllability of domain walls. Hence, in this PhD work, we select the acceptor doping method to tune the properties of lead-free ferroelectric $BaTiO_3$. Cu and Fe ions are chosen as the acceptors due to their proper valence and ionic radii.

2. Acceptor doping is a desirable tailoring method

Through comparing different methods for tailoring the hysteresis loop, the acceptor doping has been selected due to its comprehensive advantages. In order to prove these advantages of the acceptor doping method, we shall show the synthesis processes, structures of acceptor-doped $BaTiO_3$, and the modified properties of $BaTiO_3$ in this chapter.

2.1 Easy steps to achieve acceptor doping

To implement acceptor doping in $BaTiO_3$, Cu^{2+} ($r_{Cu^{2+}} = 87$ pm) and Fe^{3+} ($r_{Fe^{3+}} = 78.5$ (69) pm for high (low) spin) ions are selected as acceptors because of their lower valences than Ti^{4+}, following chemical reactions:

$$BaCO_3 + (1-x)TiO_2 + xCuO \longrightarrow BaTi_{1-x}Cu_xO_{3-x} \tag{2.1}$$

$$2\,BaCO_3 + (2-2\,x)TiO_2 + xFe_2O_3 \longrightarrow {}_2BaTi_{1-x}Fe_xO_{3-\frac{1}{2}x} \tag{2.2}$$

Different doping concentrations of Cu(0.4, 0.8, 1.2, 1.6 at%)-doped $BaTiO_3$ and Fe(0.5, 1.0, 1.5 at%)-doped $BaTiO_3$ ceramics were prepared by the traditional solid-state method[73, 74], one of the most widely used routes for the synthesis of advanced functional materials. This method is easy to control and consist in three steps: mixing, calcining, and sintering, as shown in Figure.2.1.

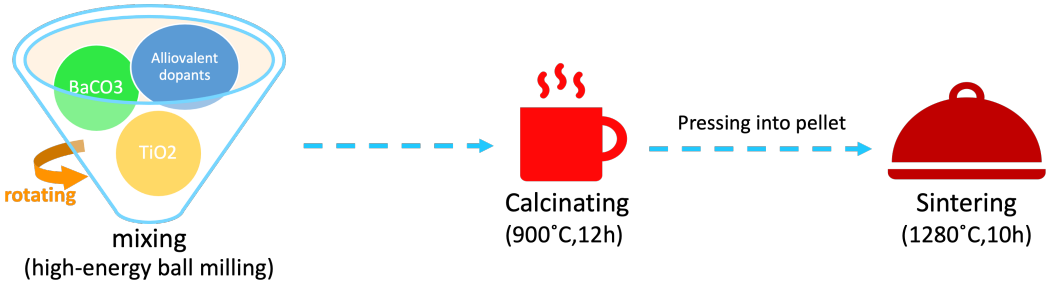

Figure 2.1: Simplified diagram of the traditional solid-state solution to synthesize acceptor-doped ferroelectric ceramics.

$BaCO_3$ (STREM 99.9 %), TiO_2(STREM 99 %, anatase), CuO (SIGMA-ALDRICH 99 %), and Fe_2O_3 (VENTRON 99.9 %) were used as raw materials. First, only $BaCO_3$ was preheated at 500 °C for 5 hours to remove any absorbed moisture. Then, the mixed powders were ball-milled by WC balls in a WC jar at 450 rpm for 8 h for Cu-doped and Fe-doped $BaTiO_3$ and at 150 rpm for 1 h for preparing pure $BaTiO_3$ (BTO). After being cleaned by alcohol for a half-hour, the dried compound was calcined at 900 °C for 12 h in air. The powder samples after calcination are shown in Figure.2.2.

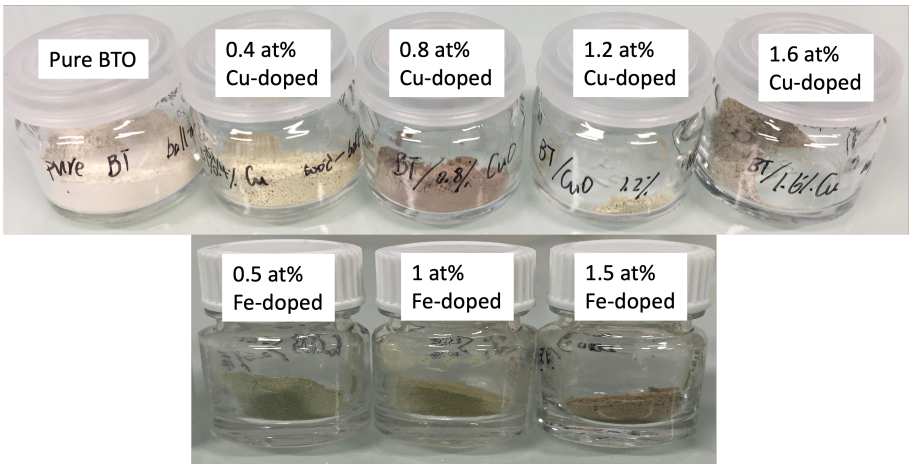

Figure 2.2: Cu-doped and Fe-doped $BaTiO_3$ powders with different doping concentrations after calcination (900 °C for 12 h in air).

Finally, calcined powders were pressed into pellets (under 147 MPa of uniaxial pressure) and sintered at 1280 °C for 10 h in air. After sintering, every pellet was polished with SiC paper and annealed at 500 °C for 1 h to release potential mechanical stresses. The annealed pellet samples are shown in Figure.2.3.

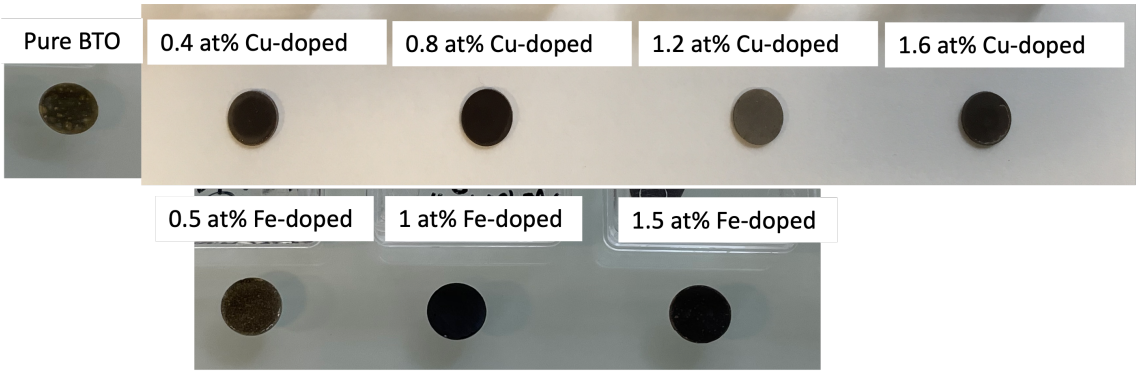

Figure 2.3: Cu-doped and Fe-doped $BaTiO_3$ pellet samples.

As the doping concentrations are low and could not be easily quantified with a sufficient precision, all the compositions is this manuscript are nominal compositions. The relative densities (RD) of the samples and their uncertainties are listed in Table 2.1. Relative densities were calculated by using Equation.2.3 and calculations of the uncertainties in samples densities followed Equation.2.4.

Doping concentration	**relative densities (RD)**	**Uncertainty**
pure BTO	91.2 %	0.0057
0.4 at% Cu	93.6 %	0.0064
0.8 at% Cu	91.9 %	0.0063
1.2 at% Cu	91.0 %	0.0049
1.6 at% Cu	92.4 %	0.0073
0.5 at% Fe	93.9 %	0.0079
1.0 at% Fe	95.8 %	0.0080
1.5 at% Fe	97.9 %	0.0069

Table 2.1: The relative densities (RD) of annealed pellet samples and the uncertainties.

$$RD = \frac{\rho_{pellet}}{\rho_{nominal}} \tag{2.3}$$

Where RD is relative density, ρ_{pellet} is the density of the sample, and $\rho_{nominal}$ is the calculated density of doped $BaTiO_3$ at their nominal doping concentration, which is from the software Jana2006.

$$\frac{\Delta\rho}{\rho} = \frac{\Delta m}{m} + \frac{\Delta V}{V} = \frac{\Delta m}{m} + 2\frac{\Delta d}{d} + \frac{\Delta t}{t} \tag{2.4}$$

Where ρ is the density, m is the mass, V the volume, d the diameter, and t the thickness of the pellet sample.

Besides the relative-density values, the dense structures of acceptor-doped $BaTiO_3$ ceramics can also be observed by using the Scanning Electron Microscope (SEM) (Helios Nanolab 660, FEI Thermofischer). The surface morphologies of acceptor-doped $BaTiO_3$ are shown in Figure.2.4 and Figure.2.5. The grain sizes of Cu-doped $BaTiO_3$ ceramics range from 10 to 140 µm. The Fe-doped $BaTiO_3$ ceramics consist of large grains of 5-180 µm and small grains of 0.2-2.4 µm. The reasons causing for this dual distribution of grain size in Fe-doped $BaTiO_3$ ceramics are still not clear.

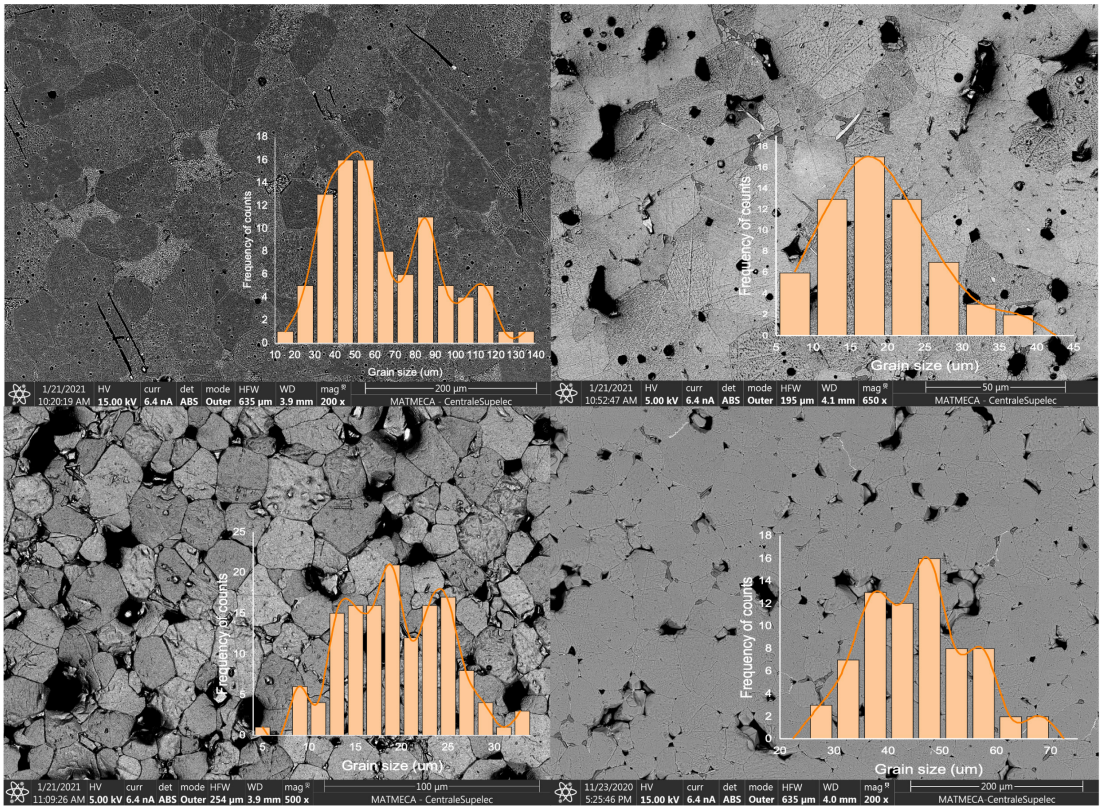

Figure 2.4: SEM images of Cu-doped $BaTiO_3$ showing the dense structure, with the corresponding grain size distribution (insert). (a) 0.4 at%Cu-doped $BaTiO_3$; (b) 0.8 at%Cu-doped $BaTiO_3$; (c) 1.2 at%Cu-doped $BaTiO_3$; (d) 1.6 at%Cu-doped $BaTiO_3$. A Scanning Electron Microscope (SEM) (Helios Nanolab 660, FEI Thermofischer) was used. The grain sizes were measured by using software ImageJ.

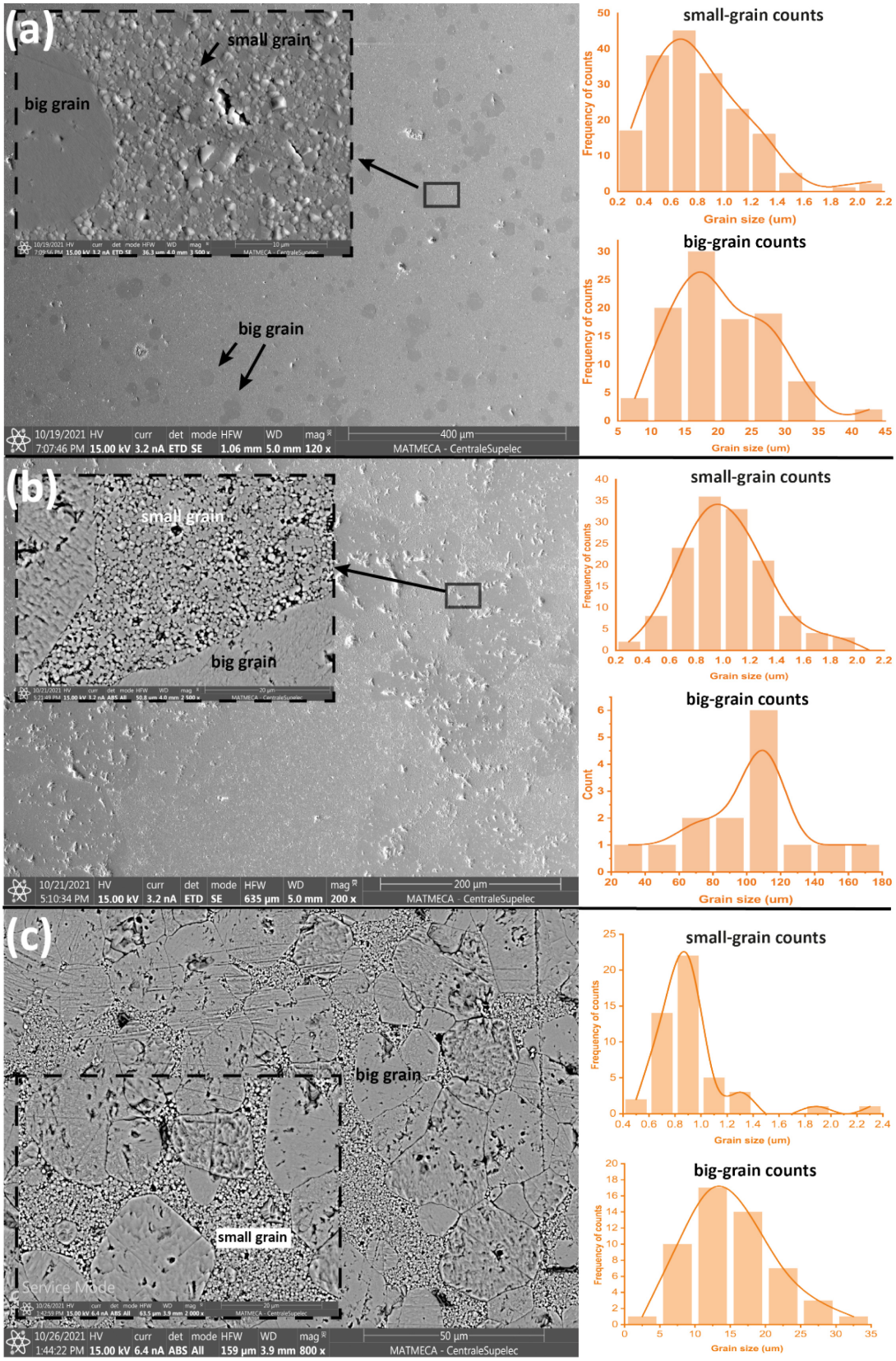

Figure 2.5: SEM images of Fe-doped $BaTiO_3$ showing the dense structure, with the corresponding grain size distributions. (a) 0.5 at%Fe-doped $BaTiO_3$; (b) 1.0 at%Fe-doped $BaTiO_3$; (c) 1.5 at%Fe-doped $BaTiO_3$. A Scanning Electron Microscope (SEM) (Helios Nanolab 660, FEI Thermofischer) was used. The grain sizes were measured by using software ImageJ.

The breakdown fields of 0.4 at%Cu-doped $BaTiO_3$ could be extrapolated from a two-parameter Weibull distribution[7, 75, 76], following Equation.2.5 and 2.6:

$$P(E_i) = 1 - \exp\left[-\left(\frac{E_i}{E_W}\right)^m\right] \tag{2.5}$$

$$\ln\left[\ln\left(\frac{1}{1-P(E_i)}\right)\right] = m\ln\left(\frac{E_i}{E_W}\right) \tag{2.6}$$

Where $P(E_i)$ is cumulative breakdown probability for a certain electric field, E_i is the breakdown field of each sample. E_W is the Weibull characteristic breakdown field, and m is the Weibull modulus. $P(E_i)$ is generally calculated from the median rank (MR)[77]: $(i - 0.3)/(n + 0.4)$, in which, i is the sample number, and n is the total number of samples.

According to the European Standard[78], the breakdown field of each sample (E_i) at room temperature is tested through a 20s step-by-step method. The Piezoelectric Evaluation System (TF analyzer 2000E with FE-mode, AixAcct) was applied on samples with silver paste as electrodes. The voltage profile is shown in Figure.2.6. The samples are immersed in silicon oil during the test to prevent flashover. E_i is based on the highest nominal voltage which is withstood for the 20 s without breakdown.

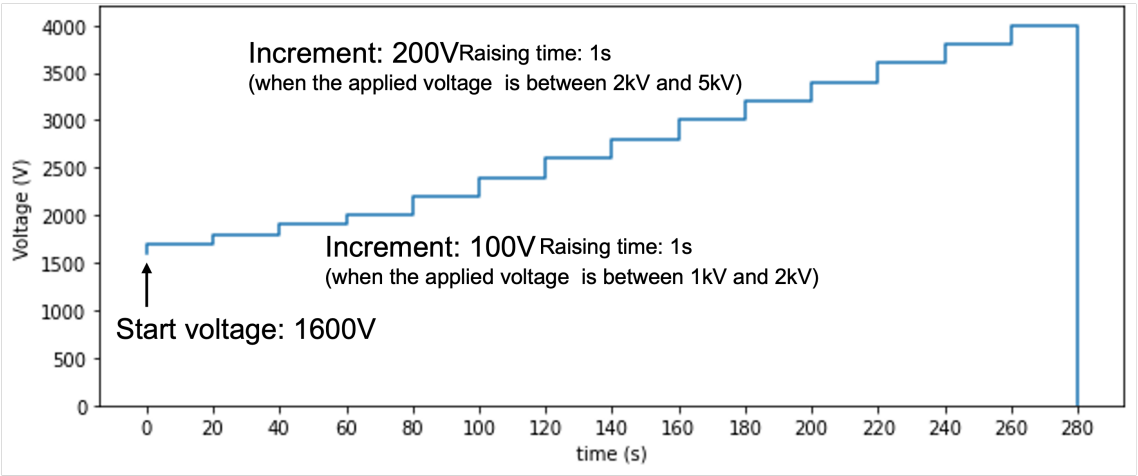

Figure 2.6: The waveform of voltage during the 20 s step-by-step test. 40 % of the probable short-time breakdown voltage (estimated from a preliminary rapid-raise test) is selected as the start voltage. The breakdown field of each sample (E_i) is based on the highest nominal voltage which is withstood for the 20 s without breakdown.

After ranking the E_i data in ascending order, the Weibull characteristic breakdown field (E_W) and Weibull modulus (m) are obtained from a linear fit, as shown in Figure.2.7. The fitted slope of 3.2115 ($\pm$ 0.4277) is the Weibull modulus (m), and the intercept of 3.80 ($\pm$ 0.02) on the x-axis indicates the Weibull characteristic breakdown field (E_W) of 0.4 at% Cu-doped $BaTiO_3$, that is 45 ($\pm$ 1.1) kV cm^{-1}. As the important operative parameter for the $BaTiO_3$ applications, the breakdown field is generally affected by ceramic density and grain size. As shown in Table 2.2, different synthesis processes cause different relative densities of ceramics as well as grain sizes. Therefore, it is difficult to compare directly the breakdown field of 0.4 at% Cu-doped $BaTiO_3$ with the one of undoped $BaTiO_3$, synthesized in the same conditions and with similar grain size. The breakdown field of our doped-$BaTiO_3$ samples is not dramatically inferior to the ones of high-density $BaTiO_3$ samples synthesized by various techniques.

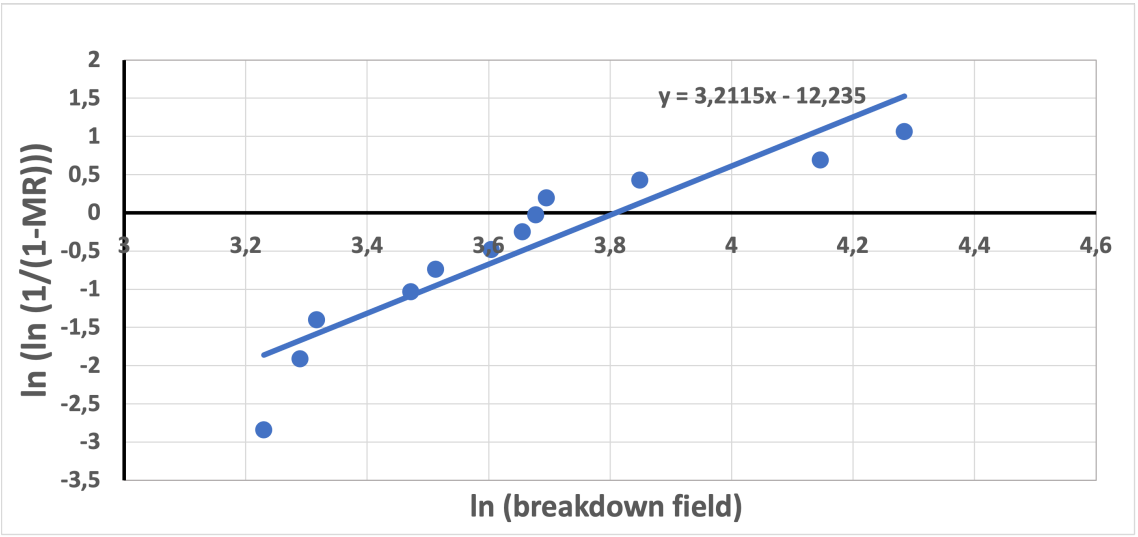

Figure 2.7: Linear fit of the Weibull distribution of the breakdown field for 0.4 at% Cu-doped $BaTiO_3$. The median rank (MR)[77] is calculated by Equation: $(i - 0.3)/(n + 0.4)$. Through the intercept between the x-axis and the linear fitted line (through software Microsoft Excel), the Weibull characteristic breakdown field (E_W) of 45 ($\pm$ 1.1) kV cm^{-1} is obtained.

2.2 Acceptor doping builds simple structures

Through the easy steps of the traditional solid-state method, the compact doped $BaTiO_3$ ceramics are successfully synthesized. Besides the simple synthesis process, the acceptor doping method has as less as possible modification on the structure of the base ferroelectrics. The structures of Cu-doped and Fe-doped $BaTiO_3$ ceramics are determined by using X-ray diffraction (XRD), Raman spectroscopy, EPR spectra, and energy-dispersive X-ray spectroscopy (EDX) mapping measurement.

2.2.1 Doped $BaTiO_3$ keeps tetragonal phase

The crystal structures of Cu-doped $BaTiO_3$ ceramics were characterized using X-ray diffraction (Bruker D2 phaser with Cu-K_α radiation, λ = 1.5406 Å). The 2θ step size was 0.02°, and the acquisition time was 10 s step^{-1}. The synchrotron radiation-based (SPring-8) X-ray diffraction (SR-XRD) was used to measure the crystal structures of Fe-doped samples (Carried out by Dr. Jun Kano, Okayama University Japan). The X-ray energy is 15.48880 keV (0.800578 Å) (Beam diameter is 0.5 mm). The samples were inserted into a capillary glass tube (d=0.3 mm), and linear absorption coefficient was 1.65570 $\times 10^{-3}$ cm^{-1}.

As shown in Figure.2.8, no trace of impurity or secondary phase is detected on the XRD pattern of 0.4 at% Cu-doped $BaTiO_3$. In particular, no sign of a hexagonal phase (such as detected in 0.5 at% Fe-doped $BaTiO_3$[63]) is found. The 0.4 at% Cu-doped $BaTiO_3$ keeps the perovskite structure of pure $BaTiO_3$ with a tetragonal phase at room temperature. The insert of Figure.2.8 shows that the intensity ratio of the (002) and (200) peaks is opposite to the one expected from randomly oriented grains. The corresponding Lotgering factor is 0.133. The 0.4 at%Cu-doped $BaTiO_3$ ceramics, therefore, exhibit a preferential (00l) orientation.[83, 84]

Samples	**Breakdown field** ($kV\,cm^{-1}$)	**Average grain size** (μm)	**Relative density**	**Synthesis process**
Undoped $BaTiO_3$[79]	124	0.126	88.4 %	Dried slurry is calcined at 800 °C for 2 h and sintered at 1200 °C for 10 m and then at 1050 °C for 10 h
Undoped $BaTiO_3$[80]	25	25	95.3 %	$BaTiO(C_2O_4)_2 \cdot 4\,H_2$ is calcined at 1000 °C for 1 h and sintered at 1400 °C for 2 h
Undoped $BaTiO_3$[81]	85	41	95.3 %	High-purity-hydrothermally synthesized powders are sintered at 1400 °C for 2 h
Undoped $BaTiO_3$[82]	225	145	98.8 %	Ball-milled powders are calcined at 800 °C for 2 h and sintered at 1300 °C for 2 h
0.4 at%Cu-doped $BaTiO_3$ (this work)	45	64	93.6 %	Ball-milled powders are calcined at 900 °C for 12 h and sintered at 1280 °C for 10 h

Table 2.2: The breakdown field of $BaTiO_3$ ceramics that are synthesized by different processes.

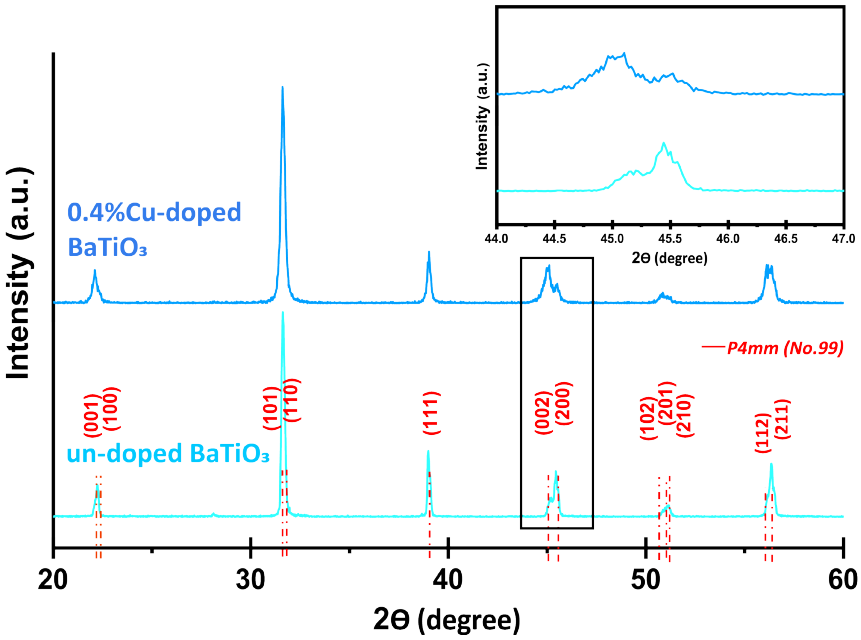

Figure 2.8: XRD patterns of annealed 0.4 at% Cu-doped $BaTiO_3$ at room temperature illustrating the purity of the samples. (insert) The (00l)-preferred orientation is evidenced by the inverse intensity ratio of the (002) and (200) peaks at around 45 ° compared to un-doped $BaTiO_3$. A X-ray diffraction (Bruker D2 phaser with Cu-K$_\alpha$ radiation, λ = 1.5406 Å) was used. The 2θ step size was 0.02°, and the acquisition time was 10 s step^{-1}.

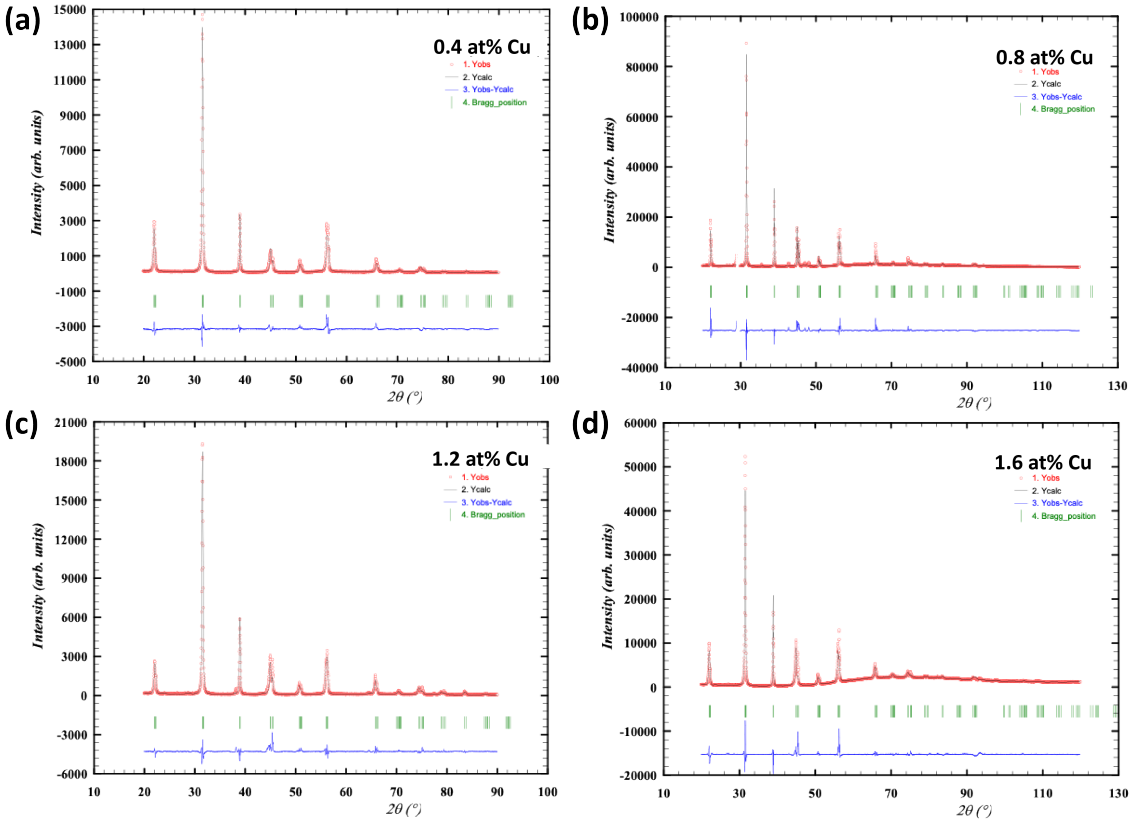

Figure 2.9: Rietveld refined XRD patterns of annealed Cu-doped $BaTiO_3$ pellet samples at room temperature (By using the Fullprof software). The XRD patterns were obtained by using X-ray diffraction (Bruker D2 phaser with Cu-K$_\alpha$ radiation, λ = 1.5406 Å) was used. The 2θ step size was 0.02°, and the acquisition time was 10 s step^{-1}.

The structural purity of doped $BaTiO_3$ ceramics is confirmed by Rietveld refinement (Technique.2.1). The XRD data of Cu-doped and Fe-doped $BaTiO_3$ and pure $BaTiO_3$ samples were refined using JANA 2006 and Fullprof software with the single tetragonal ($P4mm$) structural model. The pseudo-Voigt peak shape function is used, and Legendre polynomial is applied for background. The experimental and fitted XRD patterns of all doped $BaTiO_3$ are shown in Figure.2.9 and Figure.2.10.

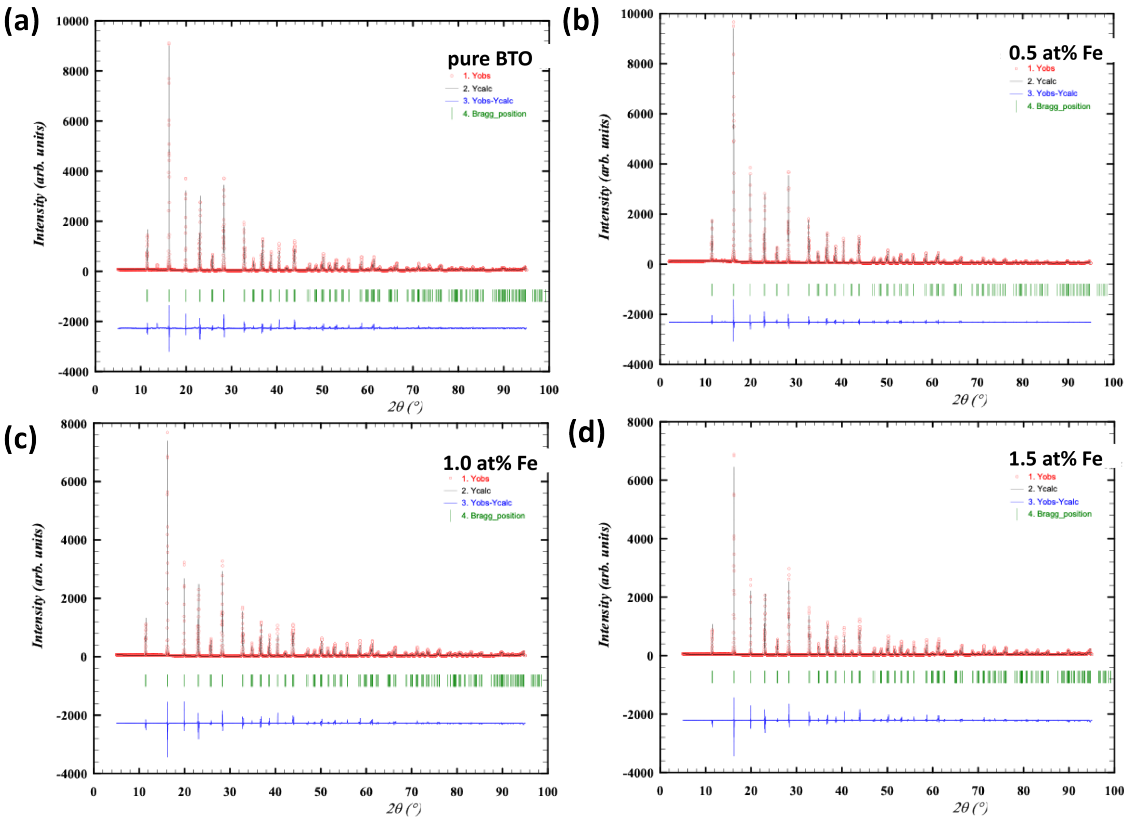

Figure 2.10: Rietveld refined XRD patterns of Fe-doped $BaTiO_3$ (annealed pellets were ground into powder) at room temperature (By using the JANA2006 software). The XRD patterns were measured by using Synchrotron radiation-based X-ray diffraction (SR-XRD) in SPring-8 of Japan (Carried out by Dr. Jun Kano, Okayama University, Japan) The X-ray energy is 15.48880 keV (0.800578 Å) (Beam diameter is 0.5 mm). The samples were inserted into a capillary glass tube (d=0.3 mm), and linear absorption coefficient was 1.65570 $\times 10^{-3}$ cm^{-1}.

Technique 2.1 — Rietveld refinement. Rietveld refinement is a technique used for the analysis of X-Ray diffraction (XRD) data.[85, 86] The Rietveld algorithm uses a least squares approach to fit a calculated profile to experimental data. A reasonable initial approximation of the parameters is required to obtain a meaningful result, including unit cell parameters and atomic coordinates of the crystal structure. Generally, the output parameters of the Rietveld refinement include weighted profile R-factor (R_{wp}), expected R-factor (R_{exp}), goodness-of-fit (GOF or χ), which

follow equations below:

$$W_i = 1/y_{i(obs)} \tag{2.7}$$

$$R_{wp} = [\frac{\sum w_i(y_{i(obs)} - y_{i(cal)})^2}{w_i(y_{i(obs)})^2}]^{1/2} \tag{2.8}$$

$$R_{exp} = [N - P/\sum w_i y_{i(obs)}^2]^{1/2} \tag{2.9}$$

$$GOF = R_{wp}/R_{exp} \tag{2.10}$$

where $y_{i(obs)}$ is observed intensity at the i^{th} step, $y_{i(cal)}$ is calculated intensity at the i^{th} step, N is number of data points, and P is number of parameters. The sum is carried out over all data points. The best fit occurs when $R_{wp} \to 0$ when GOF $\to 1$.[87, 88] It is important to remember that the successful refinement result is directly related to the quality of the data and the quality of the model (including initial approximations).

doping concentration	**a** (Å)	**c** (Å)	Uncertainty	volume (Å^3)	(00l) coefficient	R_{wp}
0 at%	3.9977	4.0307	10^{-5}	64.41	1	15.56
0.4 at%Cu	3.9899	4.0274	10^{-5}	64.11	1.096	19.50
0.8 at%Cu	3.9948	4.0328	10^{-5}	64.36	1.495	20.60
1.2 at%Cu	3.9946	4.0312	10^{-5}	64.33	1.094	19.80
1.6 at%Cu	3.9906	4.0324	10^{-5}	64.22	1.096	17.50
0.5 at%Fe	3.9971	4.0281	10^{-5}	64.42	1	13.11
1.0 at%Fe	4.0000	4.0281	10^{-5}	64.45	1	14.74
1.5 at%Fe	4.0007	4.0223	10^{-5}	64.38	1	14.58

Table 2.3: Rietveld refinement parameters of doped $BaTiO_3$ and pure $BaTiO_3$ (0 at%), including lattice parameter, preferential (00l) orientation (1 for no preferential orientation) and R_{wp}-factor values.

0.4 at% Cu-doped

```
Unit-cell volume = 64.115956 Å^3

Structure parameters

                    x         y         z
  1 Ba  Ba1      0.00000   0.00000  -0.34340
  2 Ti  Ti1      0.50000   0.50000   0.19857
  3 Cu  Cu1      0.50000   0.50000   0.19857
  4 O   O1       0.50000   0.00000   0.02398
  5 O   O2       0.50000   0.50000   0.59115
```

0.8 at% Cu-doped

```
Unit-cell volume = 64.240123 Å^3

Structure parameters

                    x         y         z
  1 Ba  Ba1      0.00000   0.00000  -0.48380
  2 Ti  Ti1      0.50000   0.50000   0.06268
  3 Cu  Cu1      0.50000   0.50000   0.06268
  4 O   O1       0.50000   0.00000  -0.07670
  5 O   O2       0.50000   0.50000  -0.46630
```

1.2 at% Cu-doped

```
Unit-cell volume = 64.325490 Å^3

Structure parameters

                    x         y         z
  1 Ba  Ba1      0.00000   0.00000  -0.36360
  2 Ti  Ti1      0.50000   0.50000   0.17037
  3 Cu  Cu1      0.50000   0.50000   0.17037
  4 O   O1       0.50000   0.00000   0.06245
  5 O   O2       0.50000   0.50000   0.56180
```

1.6 at% Cu-doped

```
Unit-cell volume = 64.288280 Å^3

Structure parameters

                    x         y         z
  1 Ba  Ba1      0.00000   0.00000  -0.34700
  2 Ti  Ti1      0.50000   0.50000   0.17287
  3 Cu  Cu1      0.50000   0.50000   0.17287
  4 O   O1       0.50000   0.00000   0.08350
  5 O   O2       0.50000   0.50000   0.68346
```

Figure 2.11: The Rietveld-refined structure parameters (atomic coordinates of Ba, Ti, O1, and O2) of Cu-doped $BaTiO_3$. O2 is the apical ion nearest neighbor to Ti ion.

The refined perusal parameters, including lattice parameters, atomic coordinates, preferential

(00*l*) orientation (1 for no preferential orientation), and R-factor values, are listed in Table 2.3, Figure.2.11 and Figure.2.12. All the Cu (0.4, 0.8, 1.2, 1.6 at%)-doped $BaTiO_3$ and Fe (0.5, 1.0, 1.5 at%)-doped $BaTiO_3$ ceramics present good fitting results with R_{wp} values below 20, indicating the single tetragonal phase of doped $BaTiO_3$ at room temperature.

un-doped $BaTiO_3$

Unit-cell volume = 64.417059 Å^3

Structure parameters

			x	y	z
1	Ba	Ba	0.00000	0.00000	-0.01853
2	Ti	Ti	0.50000	0.50000	0.50565
3	O	O1	0.50000	0.00000	0.46345
4	O	O2	0.50000	0.50000	-0.02349

0.5 at% Fe-doped

Unit-cell volume = 64.420600 Å^3

Structure parameters

			x	y	z
1	Ba	Ba	0.00000	0.00000	-0.01527
2	Ti	Ti	0.50000	0.50000	0.48455
3	Fe	Fe	0.50000	0.50000	0.48455
4	O	O1	0.50000	0.00000	0.46345
5	O	O2	0.50000	0.50000	-0.02350

1.5 at% Fe-doped

Unit-cell volume = 64.449600 Å^3

Structure parameters

			x	y	z
1	Ba	Ba	0.00000	0.00000	-0.01815
2	Ti	Ti	0.50000	0.50000	0.50323
3	Fe	Fe	0.50000	0.50000	0.50323
4	O	O1	0.50000	0.00000	0.45742
5	O	O2	0.50000	0.50000	-0.01747

1.5 at% Fe-doped

Unit-cell volume = 64.379323 Å^3

Structure parameters

			x	y	z
1	Ba	Ba	0.00000	0.00000	-0.01527
2	Ti	Ti	0.50000	0.50000	0.48455
3	Fe	Fe	0.50000	0.50000	0.48455
4	O	O1	0.50000	0.00000	0.46345
5	O	O2	0.50000	0.50000	-0.02350

Figure 2.12: The Rietveld-refined structure parameters of Fe-doped $BaTiO_3$ and pure $BaTiO_3$ (0 at%). O2 is the apical ion nearest neighbor to Ti ion.

In addition, from the XRD patterns and refinement results, it can be observed that the preferential (00*l*) orientation happens in the Cu-doped samples, not in Fe-doped samples. The preferential orientation generally contributes to the increase of the switchable polarization and piezoelectric coefficients of $BaTiO_3$.[89, 90, 91]. As shown in Figure.2.13, the Cu-doped $BaTiO_3$ ceramics show a higher tetragonality than Fe-doped $BaTiO_3$. More investigations about the effects of preferential (00*l*) orientation on the properties of the Cu-doped $BaTiO_3$ need to be further done.

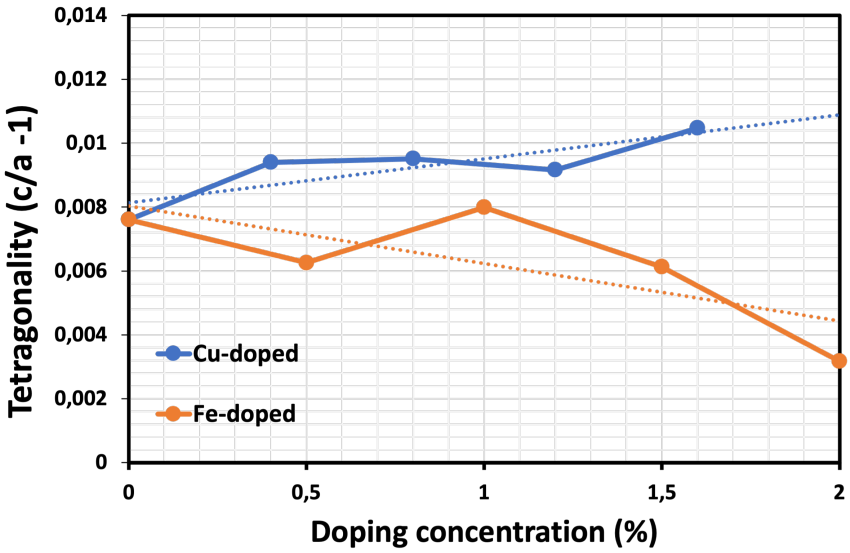

Figure 2.13: The higher tetragonalities of Cu-doped than those of Fe-doped $BaTiO_3$ ceramcis. The lattice parameters (**a** and **c**) are from the Rietveld refinement.

Moreover, a Labram-Horiba spectrometer equipped with a He–Ne, 633 nm laser was used to record the Rama spectrum of the samples at room temperature, as shown in Figure.2.14. The characteristic bands of the $BaTiO_3$ tetragonal phase are observed at about 250, 307, 513, and 714 cm^{-1}. The band at 640 cm^{-1} corresponding to the hexagonal structure is absent. It confirms the purity of the Cu-doped and Fe-doped $BaTiO_3$ ceramics.

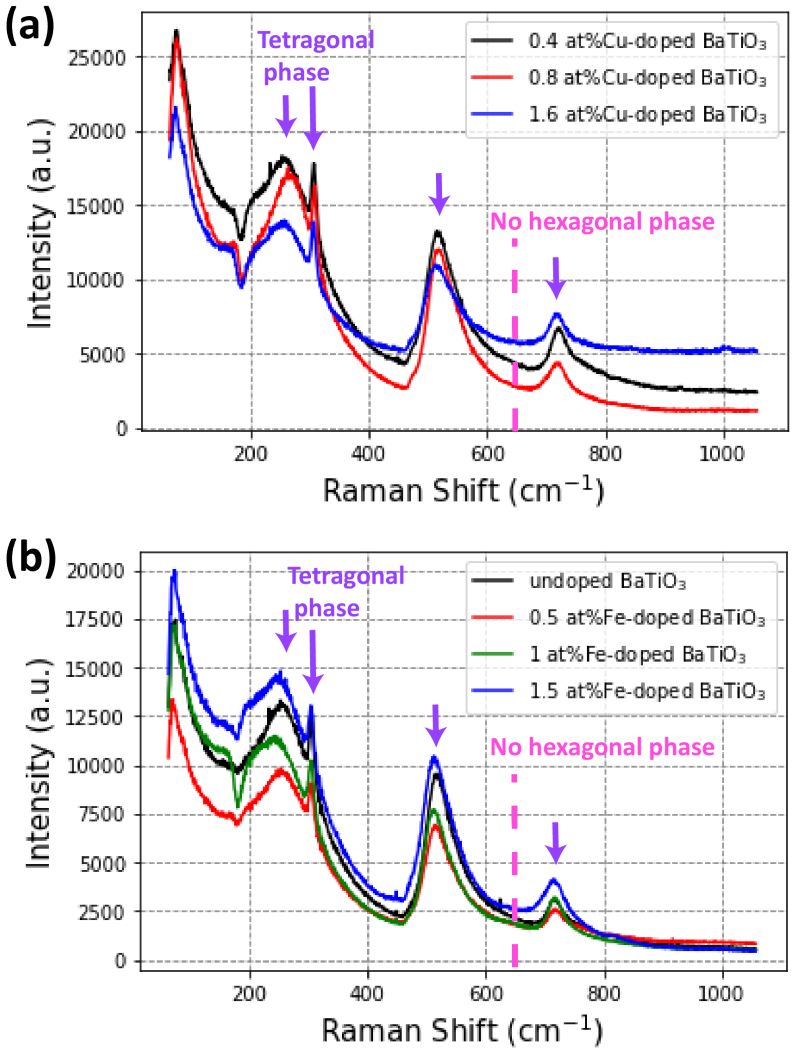

Figure 2.14: Raman spectra of the annealed Cu-doped and Fe-doped $BaTiO_3$ samples at room temperature, which shows the characteristic bands of the tetragonal phase at about 250, 307, 513, and 714 cm^{-1}. The absence of band at about 640 cm^{-1} precludes the existence of a secondary hexagonal phase.

Besides confirming the structures of doped $BaTiO_3$, the substituted positions in the $BaTiO_3$ unit cell of the Cu ions and Fe ions were identified by carrying out EPR measurements. The EPR spectra of Cu-doped $BaTiO_3$ samples in X-band (9.87 GHz) at room temperature are shown in Figure.2.15. The experimental spectra (black curves in Figure.2.15) show the presence of two tetragonal Cu^{2+} centers (CuT and CuX).[92, 61] CuT center consists of the Cu^{2+} localized substitutionally on the B site, and four O^{2-} in the equatorial plane, and the oxygen vacancy on the tetragonal axis (perpendicular to the equatorial plane).[93, 94, 95] From the simulations we determined the spin Hamiltonian parameters (hyperfine coupling constant A and g-factor) of the two centers: CuT center with g = 2.3811 and A = 108; CuX center with g = 2.393 and A = 98.

After quenching treatment disordering the oxygen vacancies, the spectra of quenched samples (red curves in Figure.2.15) show the decreases of CuT spectrum accompanied by the increases of CuX spectrum. We therefore associate the CuT-center signal to the defect dipoles and the CuX-center signal to the oxygen vacancies ($V_O^{\bullet\bullet}$) further away from the Cu ions.

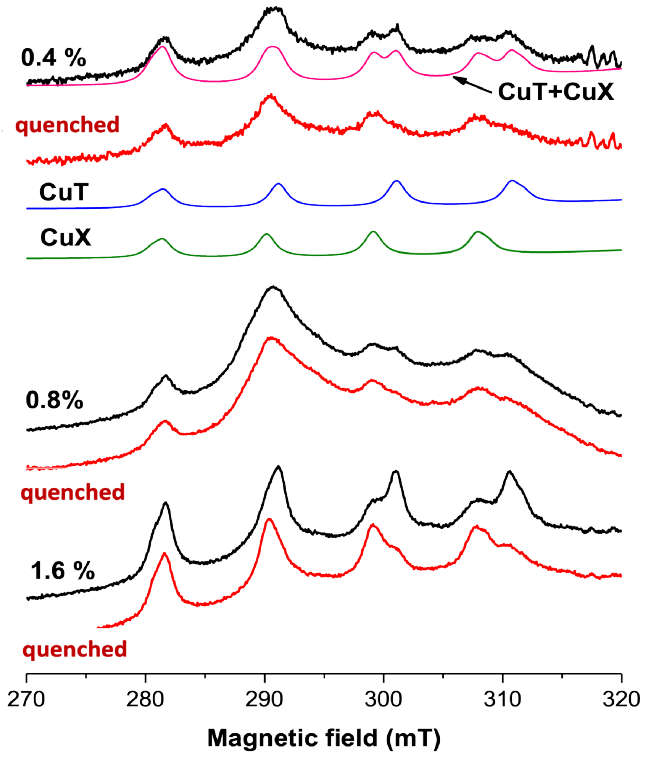

Figure 2.15: EPR spectra of Cu-doped $BaTiO_3$ (annealed pellets were ground into powder) measured in X-band (9.87 GHz) at room temperature. The experimental spectra (black) show the presence of two tetragonal Cu^{2+} centers (CuT center (blue) and CuX center (green)). CuT center (blue) consists of the Cu^{2+} localized substitutionally on the B site, and four O^{2-} in the equatorial plane, and the oxygen vacancy on the tetragonal axis (perpendicular to the equatorial plane).[93, 94, 95] The simulated spectrum is shown as pink. After quenching treatment disordering the oxygen vacancies, the spectra of the quenched samples (red) show the decreases of the CuT spectrum accompanied by the increases of CuX spectrum.

The Figure.2.16 shows the EPR spectra of Fe-doped $BaTiO_3$ samples in X-band (9.87 GHz) at room temperature. By the simulation, two tetragonal Fe^{3+} centers (T1 and T2) are detected[96, 97], which demonstrates that Fe ions have successfully substituted Ti ions on the B site of the perovskite structure. The spin Hamiltonian parameters of T1 center in 0.5 at%Fe-doped $BaTiO_3$ has g = 2.0045 and D (the axial crystal field parameter) = 825×10^{-4} cm^{-1}, T1 center in 1 at%Fe-doped $BaTiO_3$ has g = 2.0045 and D = 720×10^{-4} cm^{-1}. The spin Hamiltonian parameters of T2 center in 0.5 at%Fe-doped $BaTiO_3$ has g = 2.0045 and D = 450×10^{-4} cm^{-1}, T2 center in 1 at%Fe-doped $BaTiO_3$ has g = 2.0045 and D = 450×10^{-4} cm^{-1}. In the tetragonal phase, the axial crystal field parameter D of the Fe ions is related to the tetragonality (c/a - 1) of the unit cell.[96] Thus, the decreased D parameter value of T1 center with increasing the Fe concentration from 0.5 at to 1 at%

are the consequences of the decrease of the tetragonality.[98] This is consistent with the Rietveld refinement results (Figure.2.13).

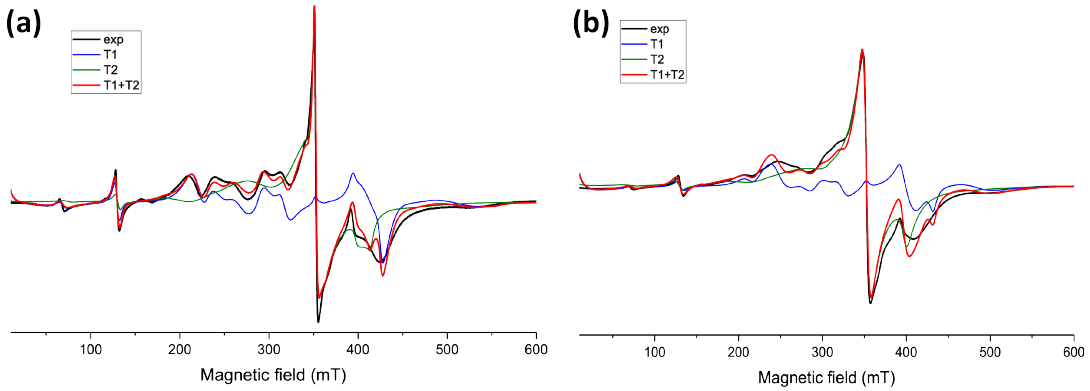

Figure 2.16: EPR spectra of 0.5 at%Fe-doped $BaTiO_3$ (a) and 1 at%Fe-doped $BaTiO_3$ (b) samples (annealed pellets were ground into powder) measured in X-band (9.87 GHz) at room temperature. By the simulation, the experimental spectra (black) show the presence of two tetragonal Fe^{3+} centers (T1 (blue) and T2 (green)), indicating Fe ions have successfully substituted Ti ions on the B site of $BaTiO_3$.

Technique 2.2 — EPR measurement (Carried out by Dr. Mariana Stefan, Laboratory. 50 - LASDAM, National Institute of Materials Physics Romania). Electron paramagnetic resonance (EPR) (or electron spin resonance (ESR)) spectroscopy[97, 99, 100] is powerful technique for studying spins of excited unpaired electrons in the presence of an external magnetic field. An unpaired electron can gain or lose angular momentum leading to change the value of its spin Hamiltonian parameters (g-factor (namely for an electron with both spin and orbital angular momenta), hyperfine coupling constant A, and the axial crystal field parameter D), which are especially significant for chemical systems of material.

In this PhD work, by measuring spin Hamiltonian parameters and observing peaks changes in EPR or ESR spectra, we determine the substitution positions of dopants in the perovskite structure of $BaTiO_3$.

2.2.2 Distribution homogeneity of dopants

Due to the small doping concentration, the transmission electron microscope (TEM,Titan3 G2 80-300, FEI ThermoFisher) equipped energy-dispersive X-ray spectroscopy (EDX) was used to detect the acceptors (Cu and Fe ions) distribution. The TEM-lamella specimens were prepared on Mo grids by focused ion beam milling instrument (MEB-FIB Helios 660, FEI Thermofischer). Then the specimens were placed in a low-background double tilt holder and covered by Al clip and Mo nut during EDX-mapping acquisition.

In the EDX map of 0.4 at%Cu-doped $BaTiO_3$ (Figure.2.17(a)), an homogeneous Cu distribution is observed. Then, several line scans across grain boundary (Figure.2.17(b)) were carried out to detect Cu segregation further. Compared to the three-standard deviations of mean Cu concentration inside the grains, the higher Cu concentration at the boundary is not observed. These EDX analyses indicate homogeneous dopant distribution in 0.4 at%Cu-doped $BaTiO_3$. With increasing Cu concentration to 1.6 at%, the Cu segregation may happen, as shown in Figure.2.18. Even though the EDX map of 1.6 at%Cu-doped $BaTiO_3$ shows homogeneous Cu distribution, the higher Cu concentrations at the grain boundary were detected by line scans (line scan 1 and 2). This dopant

segregation is not detected on the Fe-doped $BaTiO_3$ with the roughly same doping concentration, as shown in Figure.2.19.

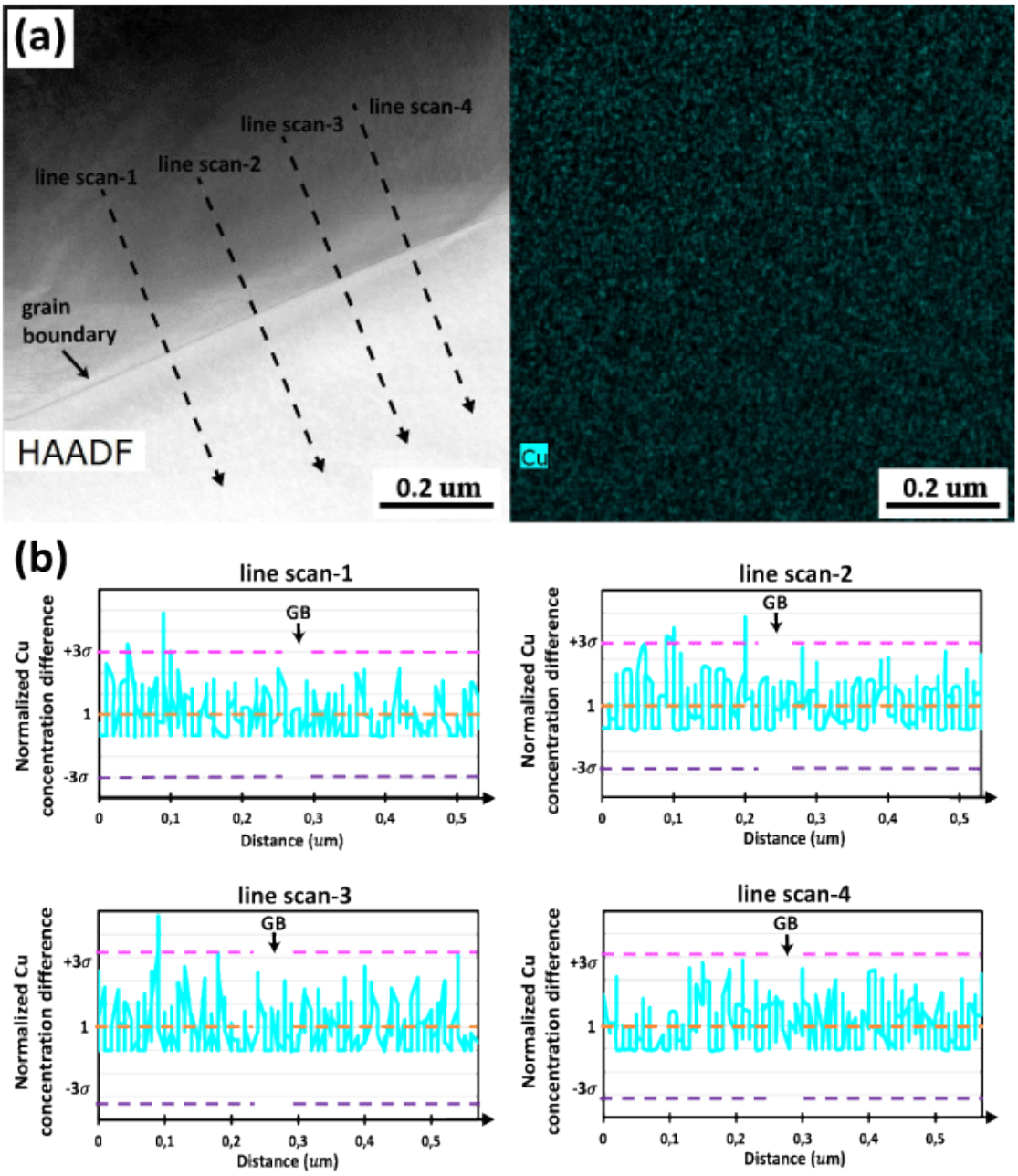

Figure 2.17: (a) The HAADF image of 0.4 at%Cu-doped $BaTiO_3$ and corresponding EDX map illustrating Cu (acceptor) distribution. The focused ion beam milling instrument (MEB-FIB Helios 660, FEI Thermofischer) was applied on annealed sample to prepare the TEM-lamella specimens. The specimens were placed in a low-background double tilt holder and covered by Al clip and Mo nut during EDX-mapping acquisition. The transmission electron microscope (TEM,Titan3 G2 80-300, FEI ThermoFisher) equipped energy-dispersive X-ray spectroscopy (EDX) was used. (b) The normalized line scans along the dotted arrows in the HAADF image enable to detect the Cu concentrations at the grain boundary and inside the grains. Compared to three standard-deviations (3σ) of the mean Cu concentration of inside the grains, no higher concentration of Cu is detected at the grain boundary, demonstrating an homogeneous Cu distribution.

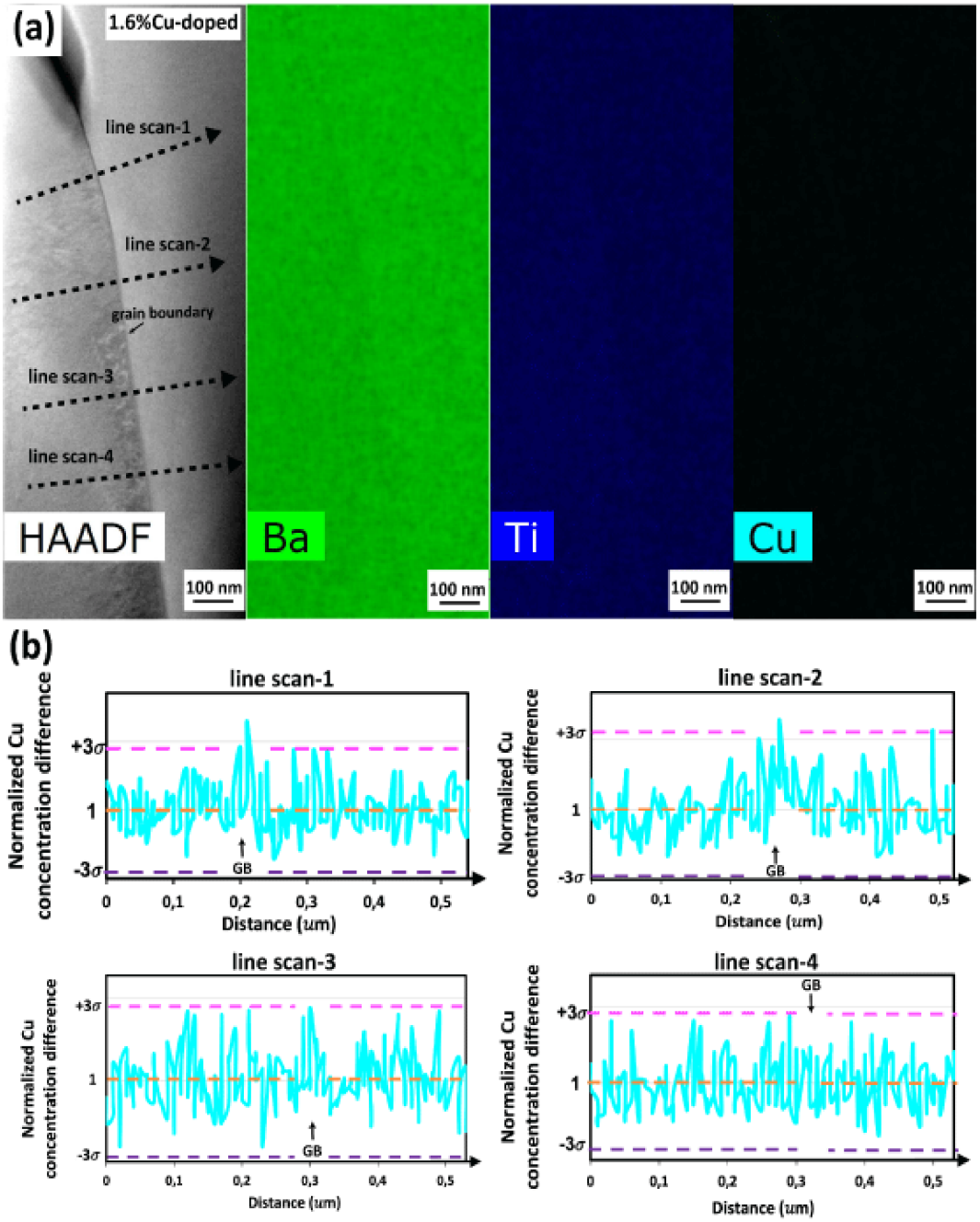

Figure 2.18: (a) The HAADF image of 1.6 at%Cu-doped $BaTiO_3$ and corresponding EDX map illustrating Cu (acceptor) distribution. The focused ion beam milling instrument (MEB-FIB Helios 660, FEI Thermofischer) was applied on annealed sample to prepare the TEM-lamella specimens. The specimens were placed in a low-background double tilt holder and covered by Al clip and Mo nut during EDX-mapping acquisition. The transmission electron microscope (TEM,Titan3 G2 80-300, FEI ThermoFisher) equipped energy-dispersive X-ray spectroscopy (EDX) was used. (b) The normalized line scans along the dotted arrows in the HAADF image enable to detect the Cu concentrations at the grain boundary and inside the grains. Compared to three standard-deviations (3σ) of the mean Cu concentration of inside the grains, higher Cu concentrations at the grain boundary are detected (line scan 1 and 2).

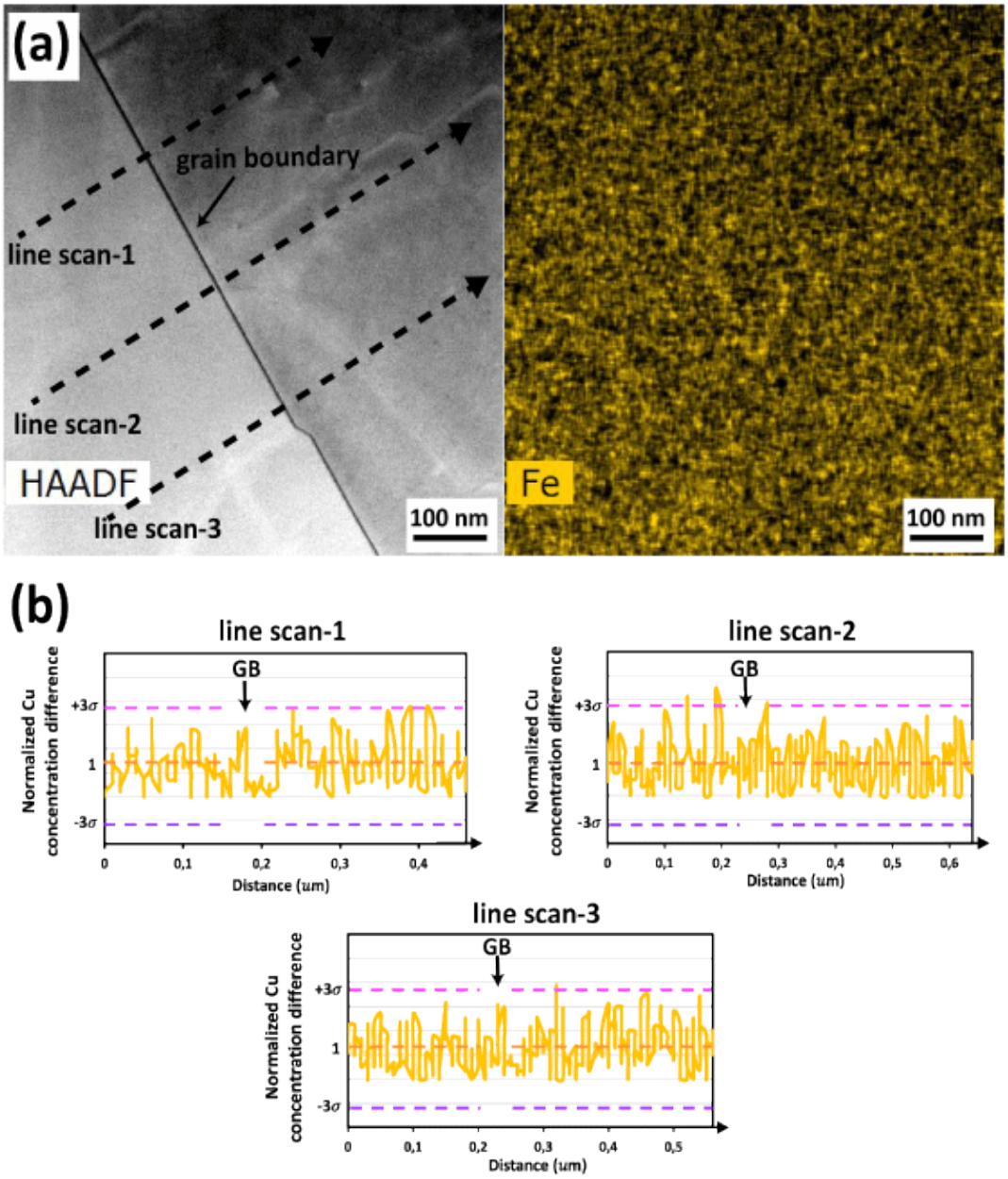

Figure 2.19: (a) The HAADF image of 1.5 at%Fe-doped $BaTiO_3$ and corresponding EDX map illustrating Fe (acceptor) distribution. The focused ion beam milling instrument (MEB-FIB Helios 660, FEI Thermofischer) was applied on annealed sample to prepare the TEM-lamella specimens. The specimens were placed in a low-background double tilt holder and covered by Al clip and Mo nut during EDX-mapping acquisition. The transmission electron microscope (TEM,Titan3 G2 80-300, FEI ThermoFisher) equipped energy-dispersive X-ray spectroscopy (EDX) was used. (b) The normalized line scans along the dotted arrows in the HAADF image enable to detect the Fe concentrations at the grain boundary and inside the grains. Compared to three standard-deviations (3σ) of the mean Fe concentration of inside the grains, no higher concentration of Fe is detected at the grain boundary, demonstrating an homogeneous Fe distribution.

As a conclusion, the EPR spectra prove that the traditional solid-state method succeeds in doping $BaTiO_3$ with Cu or Fe ions as acceptors substituting for Ti ions on the B site of the perovskite

structure. The doped $BaTiO_3$ keeps the good perovskite structure of pure $BaTiO_3$ with a tetragonal phase (*P*4*mm*) at room temperature. No trace of impurity or secondary phase, especially hexagonal phase, is detected on the XRD and Raman patterns. With the increase of acceptor concentration, the dopant-segregation phenomenon is only observed in the 1.6 at%Cu-doped $BaTiO_3$ at the grain boundary.

2.3 Acceptor doping efficiently affects the properties of ferroelectrics

Although the acceptor-doping concentration is small, acceptors can effectively cause the deformation of crystalline lattices and modify internal electric fields in ceramics. As a result, the properties of ferroelectrics, including dielectric permittivity, phase transition, ferroelectric hysteresis loop, and piezoelectric coefficient, are effectively changed.

2.3.1 Changing dielectric permittivity

The domain walls motion is a major contributor to the dielectric properties of ferroelectric. The dielectric response of tetragonal $BaTiO_3$ is significantly improved by enhancing the 180° domain wall mobility without introducing large dielectric losses, which are mostly caused by 90° domain wall motion[31] and electronic conduction[59]. The acceptor doping hinders the movement of the domain walls, generally contributing to the permittivity decrease.[62] For example, with Fe or Mn concentrations increasing to 1 at%, the permittivity of *B*-site-doped $BaTiO_3$ decreases to 1 800 or 1 000, respectively.[101] Ce^{3+}-Gd^{3+} co-doped $BaTiO_3$ (on the *B* site) also exhibits a decreased permittivity as the doping concentration increases.[102] Even though it is not the case for $BaTiO_3$ doped with 0.4 at%Cu, permittivity decreases with Cu concentrations increasing to 1.6 at% (Figure.2.20(a)). The lower permittivity of the pure $BaTiO_3$ sample compared to the 0.4 at%Cu-doped sample is due[103, 104] to the lower grain size of the pure $BaTiO_3$ sample ($<$1µm, measured by SEM) compared to the 0.4 at%Cu-doped sample (tens of µm). The doping-induced decrease of the permittivity is therefore over-compensated in the doped sample by the larger grain size. Moreover, oxygen vacancies induced by acceptor doping contribute to the conductivity, thereby contributing to the increase of the dielectric losses.[105] As shown in Figure.2.20(b), 1.6 at%Cu(acceptor)-doped $BaTiO_3$ shows higher dielectric loss than the undoped sample.

2.3.2 Changing phase transition

Because dopants have an ionic radius that differs from one of the host ions, the oxygen octahedron surrounding a dopant is distorted, and changes in phase transition temperatures are therefore expected. When smaller ions substitute for Ba^{2+} on the *A* site ($r_{Ba^{2+}} = 149$ pm), the surrounding oxygen ions displace towards the dopant, resulting in a more open space enabling the larger displacement of Ti. Such displacement is favored along the $\langle 111 \rangle$ axes rather than along the $\langle 100 \rangle$ axes.[106] As a consequence, the tetragonal phase is destabilized, and T_C decreases. For example, the T_C of Ce-doped $BaTiO_3$ ($r_{Ce^{3+}} = 115$ pm) decreases to 313 K for a Ce concentration of 3 at%.[107] The other phase transition temperatures to the orthorhombic and rhombohedral phases may also be affected. In *A*-site La-doped $BaTiO_3$ ($Ba_{1-x}La_{2x/3}TiO_3$ with $r_{La^{3+}} = 117.2$ pm) T_C decreases while T_{T-O} increases with increasing La concentration until x=0.06, resulting in an overall narrower temperature range for the tetragonal phase.[58]

Similarly, replacing Ti ions ($r_{Ti^{4+}} = 74.5$ pm) on the *B* site by dopants with different radii also distorts oxygen octahedra. Destabilization of the tetragonal phase occurs when larger ions substitute for Ti. These larger ions push the adjacent oxygen anions toward the neighboring octahedra, reducing the space for the displacement of Ti ions along the $\langle 100 \rangle$ axes. Consequently, the cubic-tetragonal transition (at T_C) is shifted to lower temperatures. The tetragonal-orthogonal phase transition (at T_{O-T}) may also be changed.[106] For example, the T_C and T_{O-T} of (1-*x*)$BaTiO_3$–*x*LiF ceramics ($r_{Li^+} = 90$ pm) are decreased to 334 K and increased to 298 K respectively, with increasing

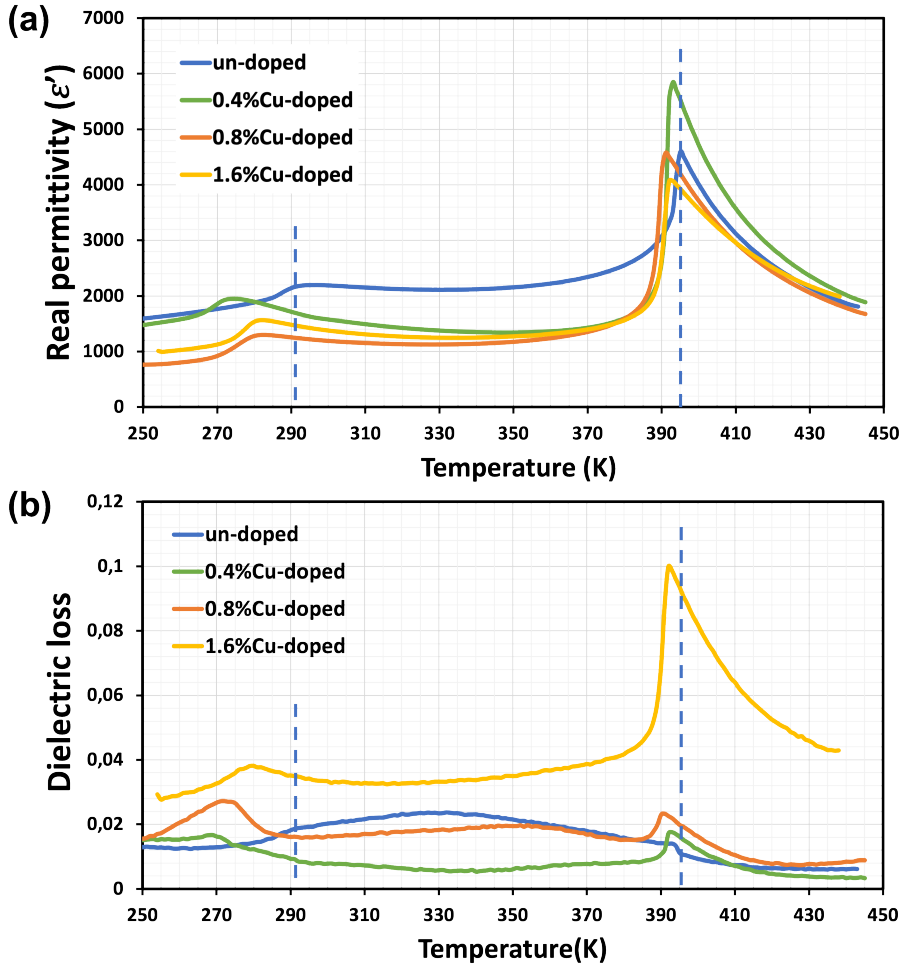

Figure 2.20: Doping effect on the real part of the relative permittivity (a) and dielectric losses (b) of Cu-doped $BaTiO_3$ with different doping concentration (at 10 kHz) as a function of temperature, compared to the un-doped $BaTiO_3$. Samples were measured through heating and cooling at 1 °C min^{-1} in cyrofurnace. The impedance analyzer (Agilent 4294A) was applied with 500 mV of oscillation amplitude from 40 to 1.1 MHz.

x (over the 2-5 at% range).[108] In $BaTi_{1-x}Mn_xO_3$ with 1.3 at% Mn ($r_{Mn^{2+}} = 97(81)$ pm and $r_{Mn^{3+}} = 78.5(72)$ pm for high (low) spin), the Curie temperature decreases to 383 K.[109] In the case of Cu^{2+} ($r_{Cu^{2+}} = 87$ pm) doping on the B site, as shown in Figure.2.20, the decreases of both T_C and T_{O-T} are observed, even though the tetragonlity of Cu-doped $BaTiO_3$ increases with increasing doping concentration (as shown in Figure.2.13).

2.3.3 Changing the hysteresis loop shape

Acceptor doping induces oxygen vacancies in the ferroelectrics, creating internal electric fields.[66, 23, 67] These fields lead to a stronger pinning effect of the domains, resulting in "hard" ferroelectrics accompanied by various hysteresis loops, such as pinched loops and shifted loops.[16, 110, 111] By manipulating the interaction between oxygen vacancies and domain walls, the hysteresis loop of acceptor-doped ferroelectrics changes shapes even with less than 1 at% acceptors, we shall discuss this effect in detail in Chapter 5.

2.3.4 Causing high piezoelectric coefficient

The contributions to the strain-electric field relationship are a very complex problem.[112, 10] Apart from the intrinsic lattice strain, domain-walls movement accounts for as much as 50% of the electromechanical effect on ferroelectric materials.[113, 114] Large nonlinear and recoverable electrostrains are most often experimentally observed due to non-180° domain walls.[2, 10, 115, 116] Thus, the factors affecting the domain-walls motions have a major influence on the electromechanical response of $BaTiO_3$.

The internal electric fields created by acceptor doping can effectively align the domains, promoting domain walls movement during the removal of the external applied electric field. As a consequence, acceptor-doped ferroelectrics have a higher piezoelectric coefficient (d_{33}) than pure $BaTiO_3$ (d_{33} = 190 pm V^{-1})[29, 60] in a specific range of electric fields. As shown in Figure.2.21, the slope of the strain response of 0.4 at%Cu-doped $BaTiO_3$ corresponds to a very large piezoelectric coefficient (d_{33}) of 1561 pm V^{-1} for electric fields from 8 to 6 kV cm^{-1}. Similarly, due to the internal electric field created by acceptor doping, the domain walls mobility of $BaTiO_3$ doped with 0.3 at%Mn[66] is increased, resulting in a d_{33} of 2100 pm V^{-1} for electric fields from 2.5 to 3.5 kV cm^{-1}. Single crystals of 0.02 at%Fe-doped $BaTiO_3$ also present a large strain (7.5×10^{-3}) at low electric field (2 kV cm^{-1}), corresponding to a d_{33} of 3750 pm V^{-1}[47] about 10 times larger than conventional piezoelectric PZT and $Pb(Zn_{1/3},Nb_{2/3})O_3$-8 at%$PbTiO_3$ (PZN-PT) ceramics[117].

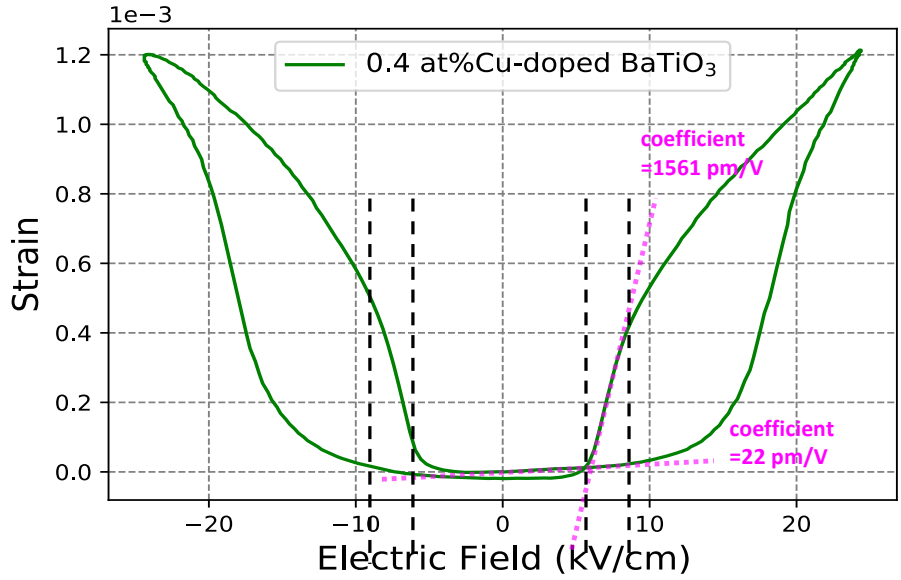

Figure 2.21: The strain vs electric field curve of hardened 0.4 at%Cu-doped $BaTiO_3$ at room temperature. In the lower field range (0 - 6 kV cm^{-1} or -6 - 0 kV cm^{-1}), the strain curve is almost flat with a corresponding piezoelectric coefficient of 22 pm V^{-1}. With decreasing electric field from 8 (-8) to 6 (-6) kV cm^{-1}, strain drastically and linearly decreases with a piezoelectric coefficient of about 1561 pm V^{-1}. The curve was measured by a Piezoelectric Evaluation System (TF analyzer 2000E with FE-mode, AixAcct) without prepolarization and leakage compensation. The sample pasted by silver was immersed in silicon oil during the test to prevent flashover. A sinusoidal electric field with 5 Hz of frequency was applied.

2.4 Summary

Summary 2 Through the easy steps of the traditional solid-state method, the acceptors (Cu and Fe ions) are successfully doped on the *B* site of $BaTiO_3$, which are demonstrated by EPR spectra. Combining with the Rietveld-refined XRD patterns, and Raman spectra, these doped $BaTiO_3$ ceramics keeping the perovskite structure of pure $BaTiO_3$ with a single tetragonal phase ($P4mm$) at room temperature are determined, which indicates that the acceptor doping method has less modification to the structure of based ferroelectrics than solid solution method. At the same time, as the acceptor doping induce internal electric fields restricting the domain-walls movement, they generally contribute to the decrease dielectric permittivity, to distabilize phase transition, to change hysteresis loop shape, and to increase the piezoelectric coefficient, even with less than 1 at% acceptors. Hence, acceptor doping is a promising method for expanding ferroelectrics applications.

3. Forming defect dipoles is inevitable in acceptor-doped $BaTiO_3$

As acceptors successfully substitute Ti ion on the B site of $BaTiO_3$, oxygen vacancies are naturally induced to keep the charge neutrality.[118, 61] These oxygen vacancies cause the deformation of crystalline lattices[2], and create internal electric fields in ceramics, which hinder domain walls movements.[4, 119] Opposite to donor doping that softens ferroelectrics due to the increased mobility of domain walls[51, 53], acceptor doping impedes domains-walls movement, leading to "hard" ferroelectrics.[4, 101] The hardened ferroelectrics are also called aged, which is classically characterized by pinched[4] or shifted hysteresis loops[120, 121]. Two models are put forward to explain the hardening mechanism: the surface effect and the volume effect. Studies of these two models are abundant, from experimental methods to theoretical calculations[4, 120, 23, 122]. However, the respective magnitude of these two effects are difficult to estimate, and the questions about the hardening mechanism remain numerous. In this chapter, the volume effect is demonstrated to be achieved through be the principal hardening mechanism of polycrystalline acceptor-doped $BaTiO_3$ ceramics. This is achieved through the local resistance mapping measurement. Combining the volume effect as the hardening mechanism with the symmetry-conforming principle of point defects, the interaction between oxygen vacancies and ferroelectric domains is clearly revealed in this chapter.

3.1 Two models to explain the hardening phenomenon of acceptor-doped ferroelectrics

3.1.1 Surface effect model

The surface effect model was firstly reported by Okazaki *et al.* in 1962.[23] This model postulates that the oxygen vacancies are preferentially presented at domain walls nodes or grain boundaries to compensate for the spontaneous polarization discontinuities (P_s)[123, 124], as shown in Figure.3.1. The accumulation of oxygen vacancies leads to internal electric fields, against the applied field during polarization-reversal processes. When the external applied field is removed, this internal field restores the original direction of polarization in the domains.[23]

The surface effect pinning domain walls is frequently used to explain hardening behaviors of multi-phase materials because of second phases leading to surface charges at the grain boundaries, such as Al-doped $Pb(Ti,Zr)O_3$[23, 125] and $BaTiO_3-CaTiO_3$ pseudo-binary system[122]. However, it is merely mentioned and barely analyzed in single-phase ferroelectrics. Extrapolated from the

surface effect, the accumulations of oxygen vacancies at grain boundaries imprint directions of the polarization on the individual grains. The grain-size dependency of the hardening behavior is therefore anticipated. Moreover, the individual domain walls inside the grains remain mobile. The high hysteresis losses of ferroelectric ceramics due to domain wall oscillations is also anticipated. However, these phenomena have not been reported to the beset of our knowledge.

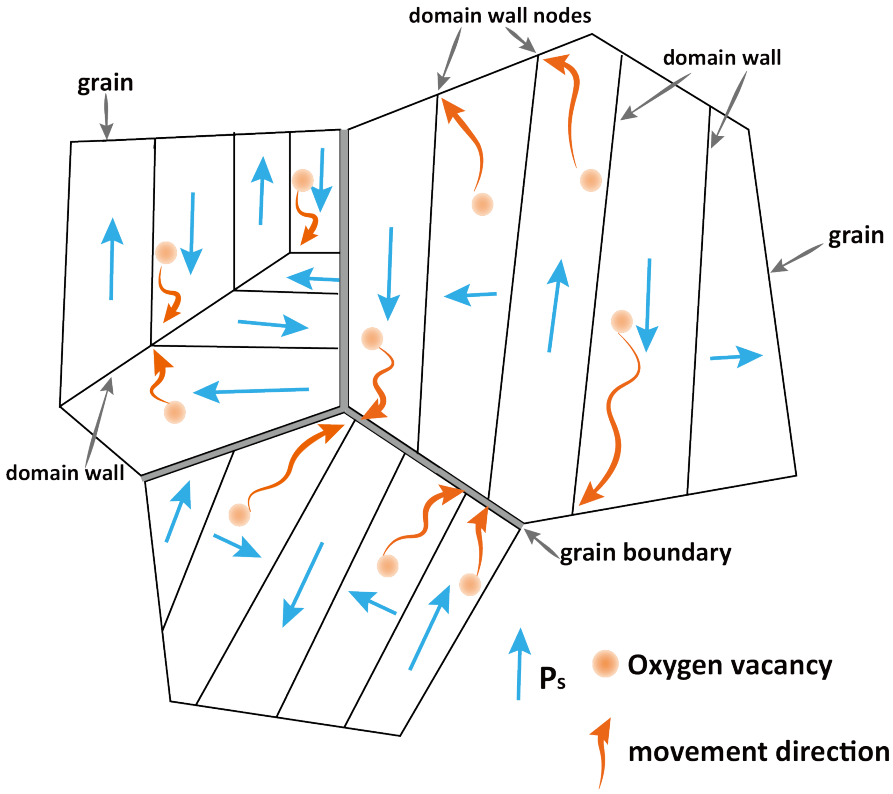

Figure 3.1: Schematic illustrating the surface effect model for the hardening mechanism. P_s is the spontaneous polarization of domains, and the orange arrows point out the diffusion directions of oxygen vacancies. The accumulation of oxygen vacancies at grain boundaries or domain walls nodes acts as internal electric fields to stabilize directions of the polarization on the individual grains.

3.1.2 Volume effect model

Within the framework of the volume effect model[23], oxygen vacancies occupy the nearest neighbor positions to dopants inside the grains to create the defect dipoles (M-$V_O^{\bullet\bullet}$-Ti), circled by dotted line in Figure.3.2. These defect dipoles act as internal bias fields to stabilize the orientation of the nearby domains.[63, 121] According to the symmetry-conforming principle of point defects, the symmetry of defect dipoles conform to the nearby domains at thermodynamic equilibrium.[68, 69] The domains therefore can be switched back to their orientations by the restoring force provided by defect dipoles upon removal of the external fields. By using DFT calculations with large-scale molecular dynamics to simulate orientation and concentration of defect dipoles in $BaTiO_3$, the hardening behaviors, including pinched hysteresis loop and horizontally shifted hysteresis loop, were obtained.[120] The volume effect was also experimental verified through using a single-domain (domain wall free) Mn-doped $BaTiO_3$ single crystal,[66]. The limitation of the volume effect is that its contribution to the hardening mechanism of the polycrystalline ferroelectrics have not been demonstrated.

Hence, motivated to reveal the hardening mechanism of acceptor-doped ferroelectrics poly-crystalline ceramics, we chose local resistance measurements to identify the distribution of oxygen

vacancies in Cu-doped $BaTiO_3$. According to the oxygen vacancies distribution, the hardening mechanism in acceptor-doped $BaTiO_3$ ceramics is consequently identified and the interactions between oxygen vacancies and domains are understood.

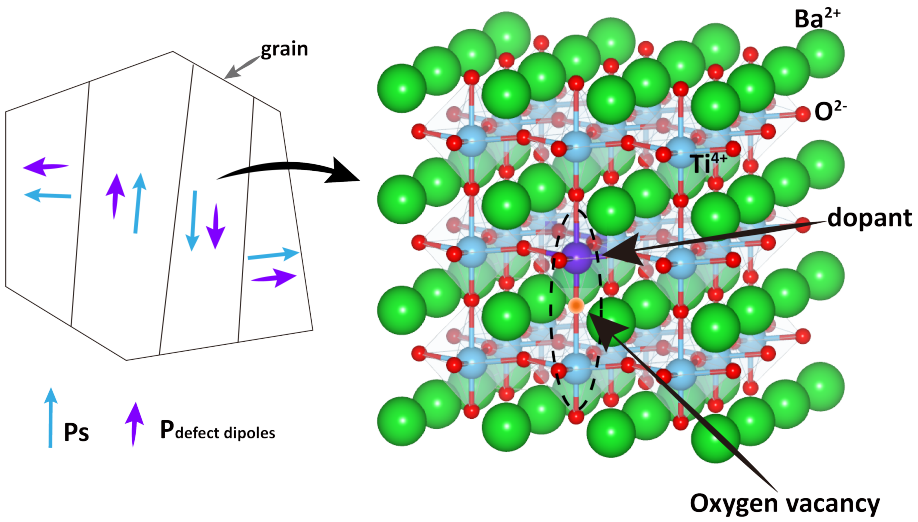

Figure 3.2: Schematic illustrating the volume effect model. Defect dipoles (circled by dotted line) are formed between oxygen vacancies and dopants in grain bulks which give rise to local internal electric fields to pin the surrounding domains. According to the symmetry-conforming principle description, the polarization of defect dipoles follow the polarization of the surrounding domains at thermodynamic equilibrium.

3.2 Proving the volume-effect model by using local resistance measurement

3.2.1 Mobile oxygen vacancies contribute to conductivity

Oxygen vacancies ($V_O^{\bullet\bullet}$) as point defect are ubiquitous in ferroelectric ceramics. Arising from the evaporation of oxygen during sintering or annealing processes[126, 119], oxygen vacancies are created in oxygen-deficient materials, such as in $BaTiO_{3-\delta}$[126] and $SrTiO_{3-\delta}$[127], following $O_0 \longrightarrow \frac{1}{2}O_2(g) + V_O^{\bullet\bullet} + 2\,e^-$.[128] In acceptor-doped ferroelectrics, the oxygen vacancies are induced into materials in order to maintain the charge neutrality.[118, 61], such as $3\,Ti_{Ti}^{\times} \longrightarrow 2\,Ti^{3+} + Ni_{Ti}'' + 2\,V_O^{\bullet\bullet}$ in $BaTi_{1-x}Ni_xO_3$,[129] and $Ba_{Ba}^{\times} \longrightarrow Li_{Ba}' + \frac{1}{2}\,V_O^{\bullet\bullet}$ in $Ba_{1-x}Li_{2x}TiO_3$[130]. In addition, oxygen vacancies can be generated by the partial Schottky reaction, following $Ba_xTi_yO_{x+2y} \longrightarrow xBa_{Ba}^{\times} + yTi_{Ti}^{\times} + (x+2\,y)O_O^{\times} + yV_{Ba}'' + xV_{Ti}'''' + (2\,x+y)V_O^{\bullet\bullet}$.[131, 132, 133]

The created oxygen vacancies not only modify the internal bias field in crystalline lattices[2], but also act as charge carriers to contribute to the conductivity of ferroelectrics.[126] For example, the oxygen-deficient $BaTiO_{3-\delta}$ exhibits an insulator to n-type conductor phase transition with increasing oxygen vacancies concentration up to 25 at%.[126, 134, 119] The generation of oxygen vacancies leads to the dielectric relaxation behavior in $(Pb_{1-x}Ba_x)(Zr_{0.95}Ti_{0.05})O_3$[135] and $KNbO_3$[119] ceramics. As concentration of oxygen vacancies increases from 0 at% to 10 at%, the resistivity of 0.5 at%Mg-doped $BaTiO_3$ ceramics decreases from 3×10^{14} Ω·cm to 1×10^{12} Ω·cm.[136]

Lee, S *et al.*[131, 137] systematically compared the conductivities of nonstoichiometric $BaTiO_3$ ceramics (undoped, A-site Ca-doped, and B-site Ca-doped $BaTiO_{3-\delta}$) through high-temperature equilibrium conductivity measurement (HiTEC). Because of a larger oxygen vacancy concentration, B-site Ca-doped $BaTiO_3$ ($Ba_{0.993}Ti_{0.987}Ca_{0.02}O_{2.987}$) shows a much higher ionic conductivity (σ_{ion} = 2.91 × 10^{-3} $(\Omega\cdot cm)^{-1}$) than undoped $BaTiO_3$ ($BaTi_{0.998}O_{2.996}$ σ_{ion} = 0.273 × 10^{-3} $(\Omega\cdot cm)^{-1}$)

and A-site Ca-doped $BaTiO_3$ ($Ba_{0.987}Ca_{0.02}Ti_{0.993}O_{2.993}$ $\sigma_{ion} = 2.06 \times 10^{-3}\,(\Omega{\cdot}cm)^{-1}$).

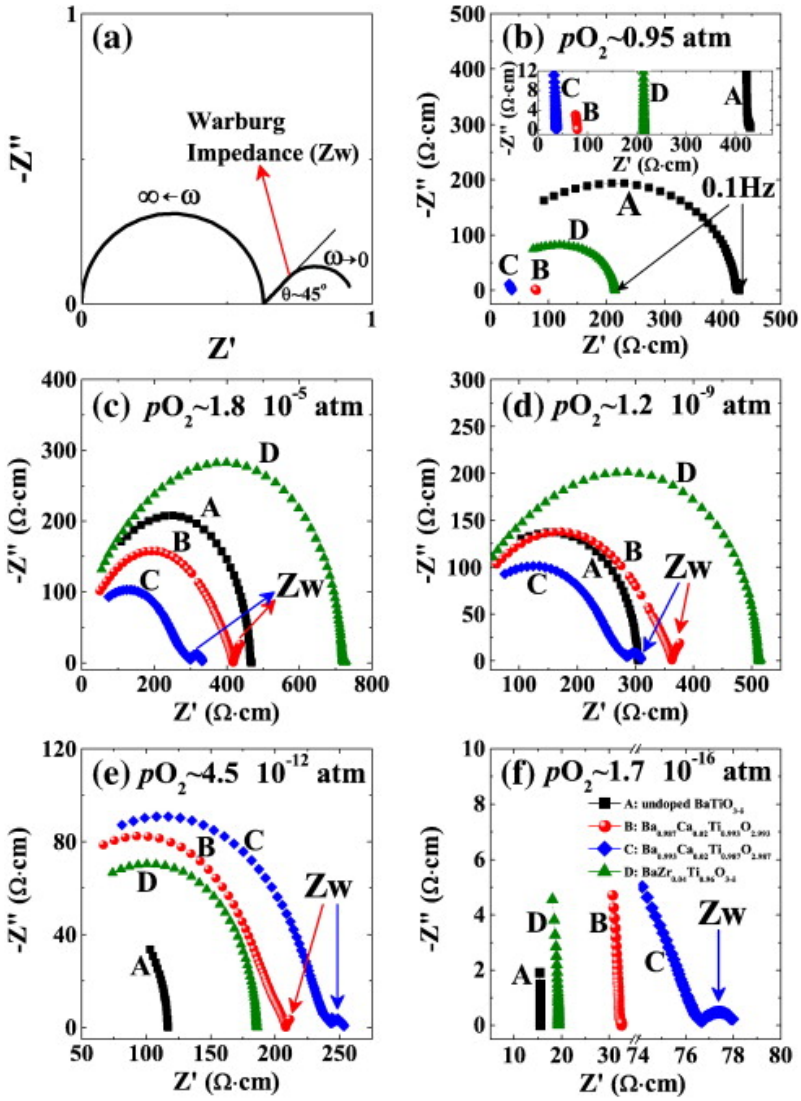

Figure 3.3: (a) Warburg impedance (Zw) and (b)-(f) Nyquist impedance plots of undoped (sample A), A-site Ca-doped (sample B), B-site Ca-doped (sample C), and B-site Zr-doped (sample D) $BaTiO_{3-\delta}$ at 950 °C over the frequency range of 1 MHz – 100 MHz with With decreasing oxygen partial pressure (ρO_2) (After Lee, S *et al.* 2013.)

Beside the DC equilibrium conductivity measurement, the contribution of oxygen vacancies to conductivity of ferroelectrics can be demonstrated by the AC impedance measurement through the Warburg impedance (Zw).[138] Because of the limited ionic diffusion, ionic conduction gives rise to a Warburg impedance at low frequencies regime at the high temperature, characterized by an additional semi-circle in impedance spectra, as shown in Figure.3.3(a)[131]. With decreasing oxygen partial pressure (ρO_2) (from (b) to (f)), the oxygen vacancy concentration is increased, resulting in that the Warburg impedance (Zw) is gradually observed clearly from the B-site Ca-doped $BaTiO_3$ samples (samples C).

These results are both obtained at high temperatures. With decreasing temperature to room temperature, the mobility of oxygen vacancies is decreased[139, 140, 118] and the conductivity of ceramics becomes complex.[141, 142] As a result, the ionic conductivity of oxygen vacancies can not be sufficient to determine the total conductivity. Nevertheless, the conductivity contributions of

oxygen vacancies guided us to use local resistance mapping measurement to investigate hardening mechanism of acceptor-doped ferroelectrics. Our hypothesis is that as the two hardening models (volume effect and surface effect) would cause different resistance distribution maps due to the different positions for accumulation of oxygen vacancies. The hardening mechanism of acceptor-doped ferroelectrics therefore could be identified according to the resistance maps.

3.2.2 Locating oxygen vacancies of acceptor-doped $BaTiO_3$ through local resistance mapping

The surface effect and volume models describe different trapping positions for oxygen vacancies in acceptor-doped ferroelectrics. The oxygen vacancies are trapped by the grain boundaries within the surface effect model or by the acceptors inside the grains according to the volume effects. Therefore the different resistance maps would be anticipated when materials are hardened (aged) by one of two effects. Imagining that sample is hardened by surface effect, in which the oxygen vacancies are most presented at grain boundaries. The resistance of grain boundary (R_{GB}) is expected to be lower than the resistance of interior of the grain (R_G). Otherwise inside of the grain is expected to have a lower resistance because of the accumulation of oxygen vacancies in the bulk of the grains according to the volume effect.

This assumption is based on the ideal regime in which oxygen vacancies induced by aliovalent doping are the only charge carriers. The contributions to ceramic conduction are complex in real samples. The sole measurement of the resistance in the interior of the grains and at the grain boundaries is not sufficient to identify the model that plays in the acceptor-doped ferroelectric. Thereby, we use an additional external electric field to disorder oxygen vacancies, which causes the “hard” sample to be relaxed (unaged or de-aged). Then local resistance maps of these relaxed (unaged or de-aged) samples are measured. Through comparing the variation of grain boundary resistance (ΔR_{GB}) and grain bulk resistance (ΔR_G), the hardening mechanism of acceptor-doped ferroelectrics in real regime is strongly identified. During the relaxation process of hardened samples, the oxygen vacancies trapped by dopants or grain boundaries are released, which contribute to the increase of the resistance of grain bulk or grain boundary depending on the model. If the sample was previously hardened by surface effect, the relaxed sample is supposed to present larger resistance variation of the grain boundaries than of the grain bulk. On the contrary, the grain bulk will show higher resistance variation than grain boundaries when volume-effect-hardened sample is relaxed. The hypothesis is summarized in the Table.3.1).

	surface effect	volume effect
Hardened state	$R_{GB} < R_G$	$R_{GB} > R_G$
Relaxed state	$\Delta R_{GB} > \Delta R_G$	$\Delta R_{GB} < \Delta R_G$

Table 3.1: The hypotheses for the resistances of the interior of the grain and grain boundary in different sample states according to the two different hardening models.

Technique 3.1 — Resiscope measurement (carried out by Dr. Pascal Chrétien, Laboratoire GeePs, CentraleSupélec). For several years, an original technique derived from atomic force microscopy called "Resiscope"[143, 144, 145, 146] has been developed at GeePs laboratory to perform local electrical investigations on the surface of materials. The general principle of this technique is described schematically in Figure.3.4. The left half of the figure corresponds to the commercial AFM (Nanoscope 5 (Bruker)), the right half corresponds to the specific "Resiscope" extension for electrical measurements. Both the tip and the cantilever are conductive. A bias voltage (about 1 V) is applied to the sample (green). The resulting current

is fed into an amplification/conversion device which gives an instantaneous value of the local tip/sample resistance. The sample is scanned line by line with the XY displacement of the piezoelectric tube while the force applied by the probe on the surface is kept constant by the Z translation of the sample. With this configuration, it is possible to simultaneously construct a map of the topography and electrical characteristics of the sample surface. The local resistance range that can be explored with the last generation of "Resiscope" used here is very wide: $10^4\,\Omega$ to $10^{14}\,\Omega$.

In this PhD work, we work in contact mode, the probe is a commercial N-doped silicon covered with P-doped diamond, the force applied is around 100 nN to 500ṅN, and all measurements are performed at room temperature atmosphere.

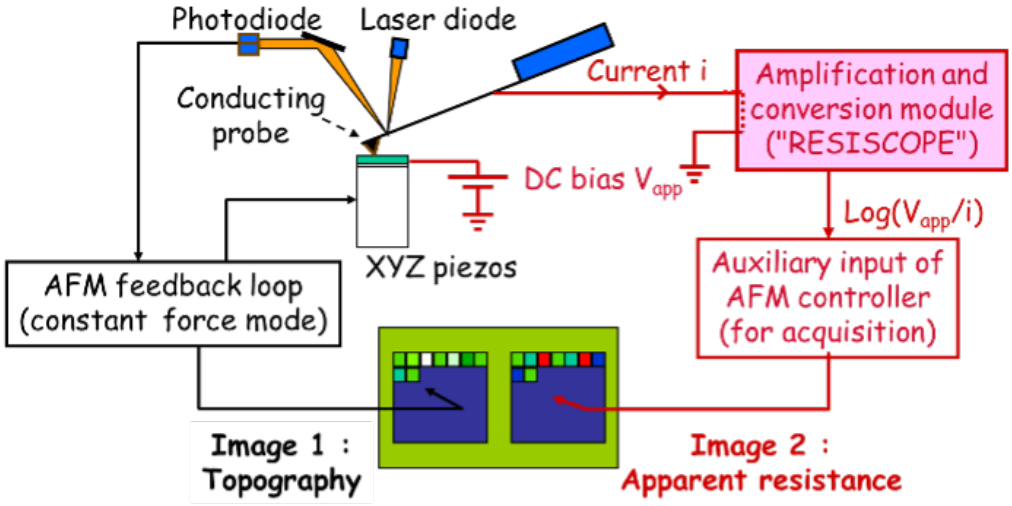

Figure 3.4: Principle diagram of "Resiscope" extension[143] coupled to a commercial AFM allowing simultaneous mappings of topography (left) and local electrical properties (Right) of a sample surface. (carried out by Dr. Pascal Chrétien, Laboratoire GeePs, CentraleSupélec)

The local resistance mapping measurement results are shown in Figure.3.5. The pinched hysteresis loop in Figure.3.5 (a) denotes the hardened state of 0.4 at%Cu-doped $BaTiO_3$. After treated by fatigue treatment (20 kV cm^{-1}, 10 Hz of oscillating electric field for 10^5 cycles), the hardened sample was relaxed and showed open hysteresis loop (Figure.3.5 (d)). The local resistance maps corresponding to two state are shown in Figure.3.5 (b) and (e), respectively. It can be observed that the lower-resistance boundaries separate three grains which have higher resistance values. The resistance in the interior of grains is homogeneous. Independent on sample sates, the resistance of grain boundaries (R_{GB}) is lower than the resistance of interior of the grain (R_G). Through using the software Gwyddion, 15 line scans across the boundaries were analyzed to obtain the precise resistance comparison between boundaries and inside the grain. The two line scans of each state are shown in Figure.3.5 (c) and (f). In hardened state, the resistance values at boundaries (R_{GB}) are $0.275\times10^{13}\,\Omega$ in line scan 1 and $0.347\times10^{13}\,\Omega$ in line scan 2, which are obvisouly lower than three standard deviations (3σ) of the average resistance inside the grains (average $R_G = 1.299\times10^{13}\,\Omega$ in line scan 1 and $1.400\times10^{13}\,\Omega$ in line scan 2). These results are consistent with the hypothesis of surface effect for ideal regime ($R_{GB} < R_G$).

However, in real samples, oxygen vacancies are not only induced by the aliovalent doping. The additional oxygen vacancies do not have dopants to associate with and tend to accumulate at the grain boundaries. As a consequence, from the sole measurement of the resistance in the interior of the grains and at the grain boundaries, it is not possible to conclude which model is the

most appropriate. This is why we compared the resistance variations when the effect of doping disappears. The variations of resistance when the sample undergoes a change from hardened state to relaxed state (*i.e.* when the effect of the doping disappears) are measured by using the software Gwyddion, as shown in Figure.3.6. The average resistance values of inside the grains in the hardened state and relaxed state were analyzed from the largest possible area of each grain. The average resistance values of the boundary were calculated from the 15 line scans across the boundaries.

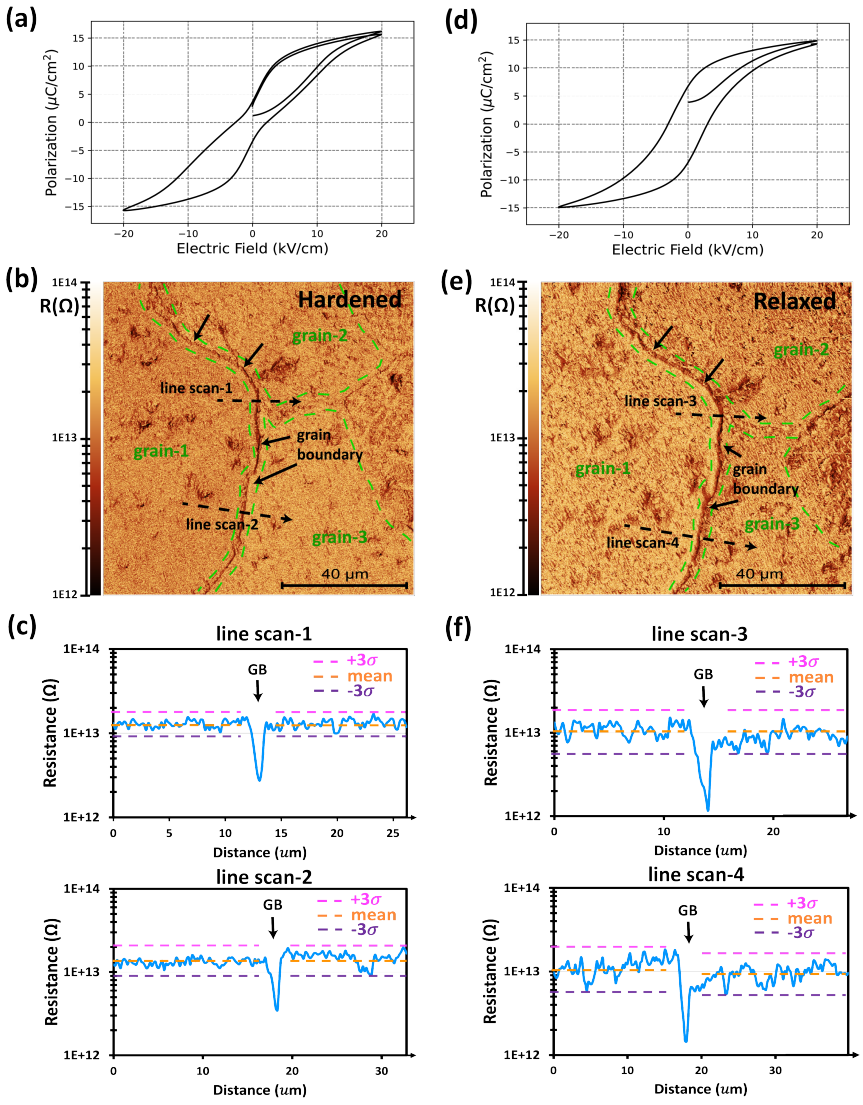

Figure 3.5: The hysteresis loops and corresponding local resistance maps of 0.4 at%Cu-doped $BaTiO_3$ in the hardened (aged) (a and b) and relaxed (unaged or de-aged) (d and e) states at room temperature. The hardened sample was relaxed by fatigue treatment (20 kV cm^{-1}, 10 Hz of rectangular oscillating electric field for 10^5 cycles. The hysteresis loops were measured by a Piezoelectric Evaluation System (TF analyzer 2000E with FE-mode, AixAcct) without prepolarization and leakage compensation. A one-and-half-cycle sinusoidal electric field with 5 Hz of frequency was applied. The resistance maps are measured by Resiscope at room temperature in air. (c) and (f) The line scans are extracted from local resistance maps in order to obtain precise resistance comparisons between grain boundaries and grain bulks. The software Gwyddion was used to carry out line scans and measure resistance values.

In relaxed state, the grain boundaries (R_{GB}) of 0.4 at%Cu-doped $BaTiO_3$ have lower resistance than inside the grains, which can be observed from local resistance map (Figure.3.5 (e)) and line scans (Figure.3.5 (f)). As shown in Figure.3.6, the resistances of grain boundary and interior of the grains both decrease when hardened 0.4 at%Cu-doped $BaTiO_3$ becomes relaxed. The resistance of three grains reduced 0.230×10^{13} Ω (ΔR_{G1}), 0.538×10^{13} Ω (ΔR_{G2}), 0.643×10^{13} Ω (ΔR_{G3}), repectively. Compared with the reduction of boundary resistance ($\Delta R_{GB} = 0.215\times10^{13}$ Ω), reductions of grain resistance are obviously larger. This results conforms with hypothesis of volume effect ($\Delta R_{GB} < \Delta R_G$). Comparing the variations of resistance is more reliable to reflect the real condition in the 0.4 at%Cu-doped $BaTiO_3$. Hence, we conclude that polycrystalline 0.4 at%Cu-doped $BaTiO_3$ ceramics are mainly hardened by volume effect not the surface effect.

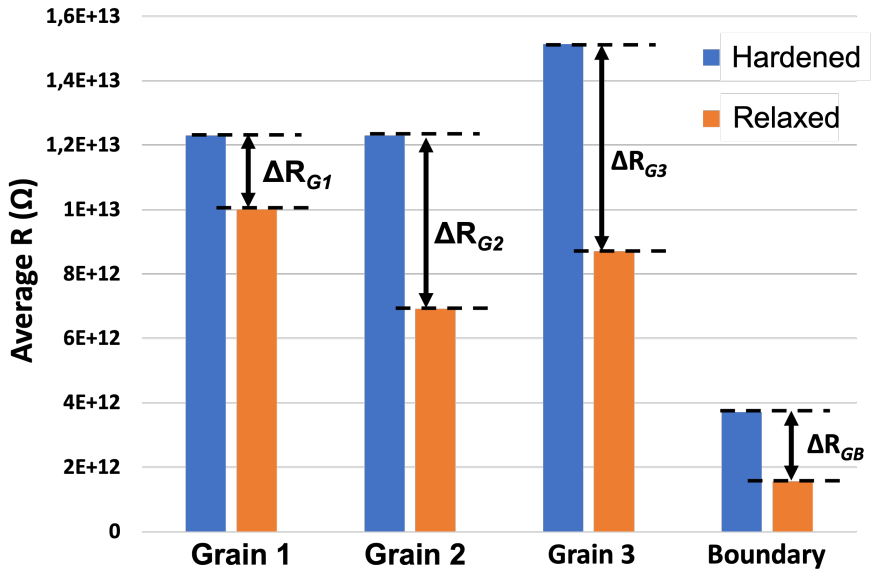

Figure 3.6: Comparison of the variation of grain boundary resistance (ΔR_{GB}) and grain bulk resistance (ΔR_G) when 0.4 at%Cu-doped $BaTiO_3$ undergoes a change from hardened state to relaxed state. By using the software Gwyddion, the average resistance values of inside the grains in the hardened state and relaxed state were analyzed from the largest possible area of each grain in Figure.3.5. The average resistance values of the boundary were calculated from 15 line scans across the boundaries. The three grains each exhibit a reduced resistance of 0.230×10^{13} Ω (ΔR_{G1}), 0.538×10^{13} Ω (ΔR_{G2}), and 0.643×10^{13} Ω (ΔR_{G3}). The reduction of boundary resistance (ΔR_{GB}) is 0.215×10^{13} Ω. The lower reduction of resistance at the boundary than inside the grains ($\Delta R_{GB} < \Delta R_G$) demonstrates that the hardening mechanism in 0.4 at%Cu-doped $BaTiO_3$ is the volume effect

3.3 Oxygen vacancies movement decides defect dipoles

By using local resistance mapping measurement (Resiscope) to compare the reduction of grain boundary resistance (ΔR_{GB}) with the reduction of inside the grain bulk resistance (ΔR_G) when the sample goes from a hardened state to a relaxed state, the volume effect is determined to be the principal hardening mechanism in acceptor-doped $BaTiO_3$ ceramics. The ferroelectric domain walls movements are restricted by the defect dipole (M-$V_O^{\bullet\bullet}$-Ti)[66, 23, 67] that is created between oxygen vacancies and acceptors, as shown in Figure.3.2. Combined with the symmetry-conforming principle of point defect, the defect dipoles-domains interaction can be microscopically understood. This interaction will better guide us to engineer the properties of acceptor-doped ferroelectrics.

3.3.1 Reorientation of defect dipoles as oxygen vacancies hopping

When the oxygen vacancy occupies one of the octahedral positions (position 1 to 6 in Figure.3.7) next to acceptor (Cu) in the perovskite structure $BaTiO_3$, the defect dipoles (M-$V_O^{\bullet\bullet}$-Ti), here M is Cu) are created. These defect dipoles act as the local internal bias field to restricting the surrounding domains rotation. Activated by the external high electric fields or thermal activation, the oxygen vacancies shall be able to undergo the long-range migration between different crystal unit cells[139, 147] or short-range hopping hopping between various sites of the oxygen octahedra.[140, 148] Through the movement of oxygen vacancies, the defect dipole achieves reorientation, vanishing, or appearing.[70, 61] As shown in Figure.3.7, when an oxygen vacancy (represented by orange ball) hops from position 6 to position 5, the defect dipole achieved a 90° rotation. The defect dipole is flipped over after oxygen vacancy finishes a position 6 → position 1 → position 3 hopping. The oxygen vacancy moves away from the dopant (represented by violet ball) and goes into the surrounding octahedra, resulting in the defect dipole vanishing. As oxygen vacancy is re-trapped by an acceptor, a new defect dipole is born.

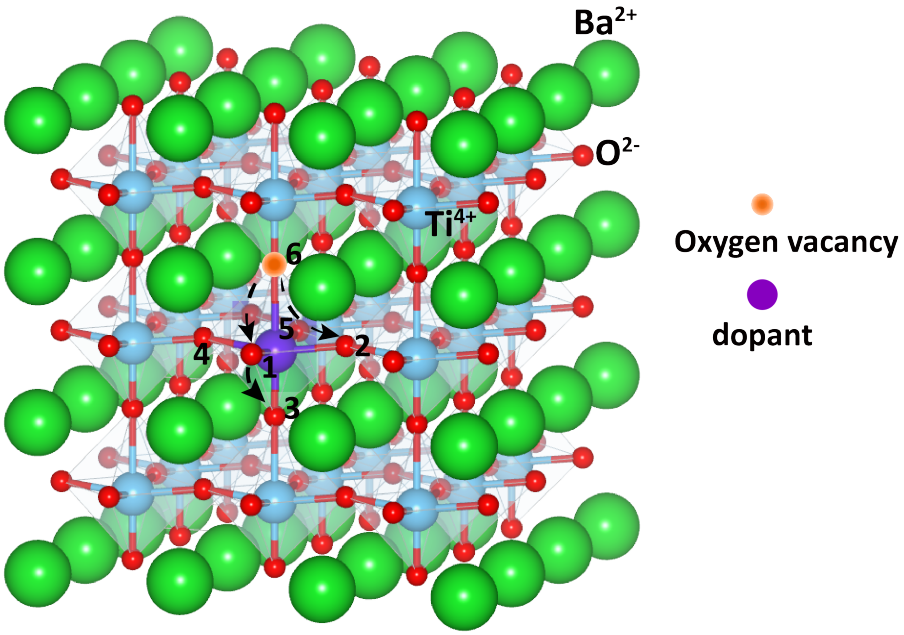

Figure 3.7: Schematic illustrating reorientations of defect dipoles. When an oxygen vacancy occupies one of the octahedral positions (position 1 to 6) next to the dopant, a defect dipole (M-$V_O^{\bullet\bullet}$−Ti) is formed. As oxygen vacancy hops between various sites of the oxygen octahedra, the reorientation of defect dipoles happens.

3.3.2 Symmetry-conforming principle of point defect

According to the symmetry-conforming principle of point defects[68], oxygen vacancies are aligned by the surrounding crystal symmetry. As a result, the defect dipoles have the same orientation as surrounding ferroelectric domains (composed of intrinsic ferroelectric dipoles) at thermodynamic equilibrium[68, 69], as an insert for state 1 in Figure.3.8). After sintering and cooling to room temperature, the randomly orientated ferroelectric domains accompanied by same orientated defect dipoles induce the initial state of the 0.4 at%Cu-doped $BaTiO_3$ ceramics as a zero net polarization. Upon increasing the external electric field, the orientation of the defect dipoles is not modified by the application of the electric field (from state 1 to state 2 and from state 1 to state 5)[17, 18] as it would necessitate the diffusion of the oxygen vacancies from one site to another.[149]. Upon removing the external field, the internal bias field from these defect dipoles

are a restoring force that accelerates the domains back-switching to their original state (state 1) in which the ceramics have a zero net polarization.[10, 8] Hence, hardened (aged) acceptor-doped ferroelectrics present a pinched hysteresis loops.

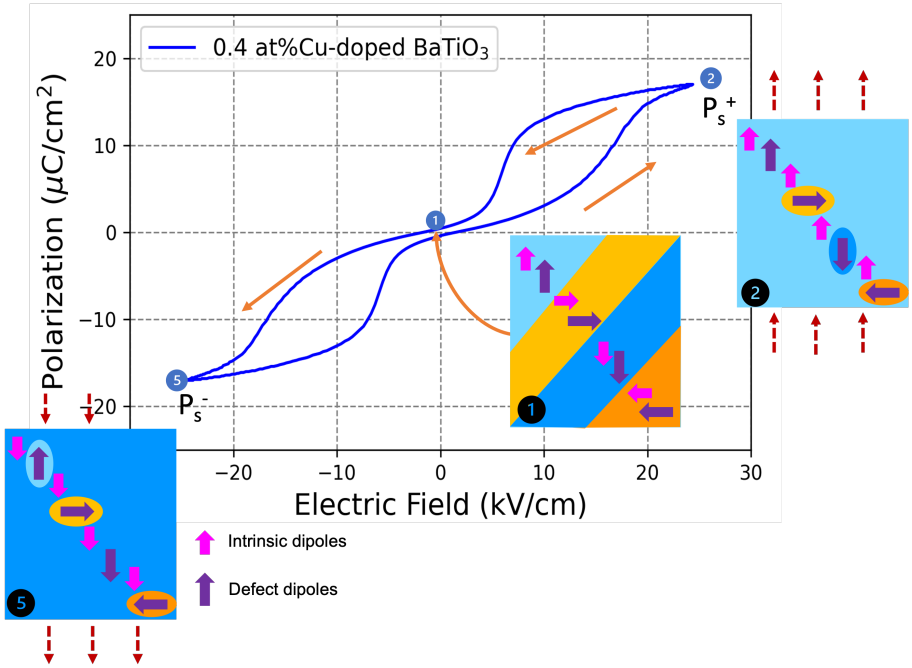

Figure 3.8: Hysteresis loop pinching process for 0.4 at%Cu-doped $BaTiO_3$ at room temperature. The positive electric field gradually aligns the intrinsic dipoles and moves the domain walls except around the defect dipoles, as shown from state 1 to state 2. When the external field is removed, the defect dipoles produce a restoring force that switches intrinsic dipoles back to their initially random orientations, results in a near-zero net polarisation. The same behavior happens under the negative electric field (between state 1 and state 5). The loop was measured by the Piezoelectric Evaluation System (TF analyzer 2000E with FE-mode, AixAcct) without prepolarization and leakage compensation. The sample pasted by silver was immersed in silicon oil during the test to prevent flashover. A sinusoidal electric field with 5 Hz of frequency was applied.

3.4 Summary

Summary 3 Oxygen vacancies modify the internal electric field, playing a crucial role to harden acceptor-doped ferroelectrics. According to the differnet trapping positions for the oxygen vancancies, the hardening mechanism is generally explained either by the volume effect or by the surface effect. As the mobile oxygen vacancies contribute to the conductivity of ferroelectric electroceramics[150, 127], we carried out local resistance mapping measurement (Resiscope) to identify the hardening mechanism in polycrystalline acceptor-doped ferroelectrics. When a hardened sample becomes relaxed (unaged or de-aged), the higher reductions of interior of the grains resistance (ΔR_G) than the reduction of grain boundary resistance (ΔR_{GB}) are observed, which demonstrates that the volume effect is the principal hardening mechanism in polycrystalline acceptor-doped ferroelectrics. Combining volume effect and the symmetry-conforming principle of point defects, the interaction between oxygen vacancies and ferroelectric domains is clearly understood. As a result, the hysteresis loop pinching process is displayed: the oxygen vacancies preferentially move to positions that are nearest neighbor to dopants, forming defect dipoles which adopt the same orientation as domains surrounding them at

thermodynamic equilibrium. These defect dipoles provide internal electric fields not only impeding surrounding domains rotations upon increasing external electric field but also quickly switching back surrounding domains to initial orientation upon removal of the external field, causing the pinching of hysteresis loop that is the hallmark of aged ferroelectrics.

4. Achieving manipulation of hysteresis loops through the control of defect dipoles

In this chapter, we shall display the control over hysteresis loops of Cu-doped $BaTiO_3$ grained by the manipulation of the orientation of the defect dipoles, including deaging, reaging, and shifting. Achieving these processes are based on the defect dipoles that are formed between oxygen vacancies and dopants. As described by symmetry-conforming principle and volume effect, ferroelectric domains align defect dipoles, then, the defect dipoles fix the orientation of domains. Inspired by this mechanism, we used fatigue treatment, quenching treatment, and field-cooling treatment to control the orientation of the defect dipoles. As a result, manipulations of hysteresis loop were achieved.

4.1 Making defect dipoles temporarily disappear causes the de-aging of the hysteresis loop

Defect dipoles provide a restoring force that pinches the hysteresis loop. This defines the "aged state". The reverse process, de-aging, corresponds to the opening of a pinched hysteresis loop. This can be obtained when defect dipoles disappear. This transformation from pinched to open loop (de-aging) is also referred to as from "clamped" to "free"[151] or "unclamped"[152]. As oxygen vacancies are far away from dopants, the defect dipoles temporarily disappear[153, 154, 148] and domains are therefore released, resulting in the de-aging process. In this section, we come up with two methods to separate oxygen oxygen vacancies from dopants, de-ageing a pinched sample (*i.e.* to open pinched loops): quenching and fatigue treatments.

4.1.1 'Freezing' oxygen vacancies prevents formation of defect dipoles

De-aging process of 0.4 at%Cu-doped $BaTiO_3$ ceramic caused by quenching treatment is shown in Figure.4.1(a). Quenching treatment consists in heating the sample in its paraelectric phase (over the Curie temperature), where intrinsic dipoles do not exist and oxygen vacancies are disordered (*i.e.* are not necessarily nearest-neighbors to dopants) before quickly cooling the sample to room temperature. After quenching, defect dipoles are not immediately created as the oxygen vacancies need time to diffuse to positions nearest-neighbor to dopants. The movement of ferroelectric domains is therefore not restricted by the defect dipoles and an open and symmetric hysteresis loop is measured akin to the one of un-doped $BaTiO_3$. A zero net initial polarization of hysteresis loop in Figure.4.1(a) proves the random orientation of the quenched ferroelectric

domains.

The result of this quenching procedure depends on the thermal conductivity of the cooling environment. For example partially pinched loops are observed in $Pb(Zr_{0.58}Ti_{0.42})O_3$ cooled in air whereas totally open loops are observed when cooled in water.[4]

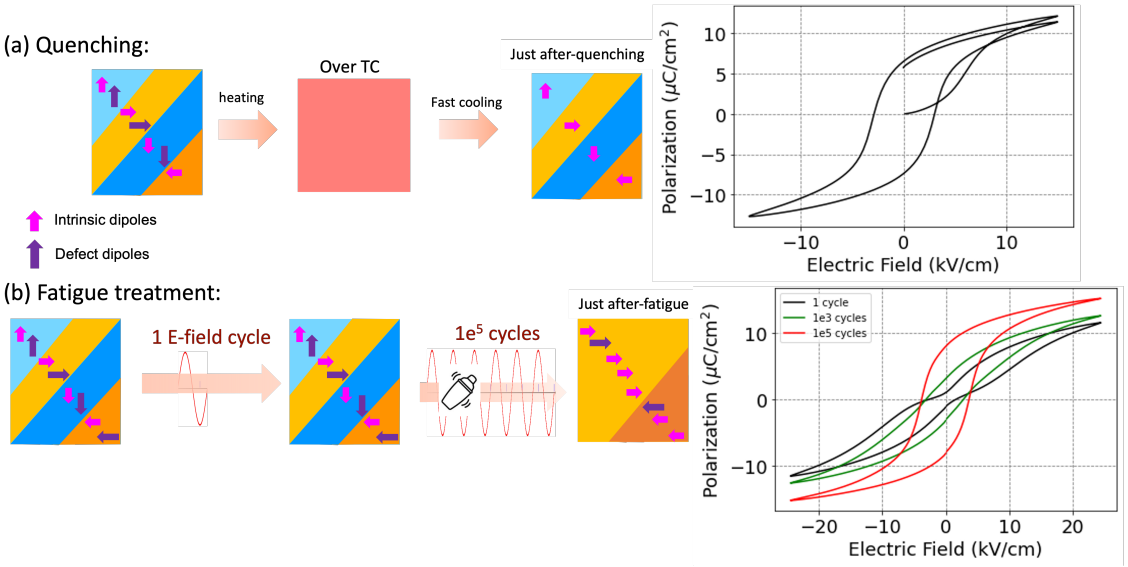

Figure 4.1: De-aging processes of a 0.4 at%Cu-doped $BaTiO_3$ ceramic: (a) Only intrinsic dipoles exist after quenching and the hysteresis loop is therefore open, starting from a "virgin" state with zero net polarisation. The loop of quenched sample was measured without prepolarization and leakage compensation. A one-and-half-cycle sinusoidal electric field with 5 Hz of frequency was applied. This enables to observe the initial polarization and remanent polarization of quenched sample. (b) Fatigue treatment (20 kV cm^{-1}, 10 Hz of rectangular oscillating electric field for 10^5 cycles) randomizes the dipoles in the direction of external fields and defect dipoles are almost eliminated due to disordered oxygen vacancies; the pinched hysteresis loop (black curve) gradually opens (green curve) before reaching a stable open shape after 10^5 cycles (red curve).

Strategy 4.1 — Quenching treatment. As shown in Figure.4.2, the quenching treatment is a progression, beginning with the heating of the sample and then rapidly cooling it in water, oil or air. Quenching generally prevents low-temperature processes by reducing the window of time during which these processes are both thermodynamically favorable and kinetically accessible.[155] In this work, the samples were heated for 10 minutes above T_C (i.e. to 150 °C) and then dropped into water for cooling. The fast cooling freezes the movement of oxygen vacancies, preventing the formation of defect dipoles as a result.

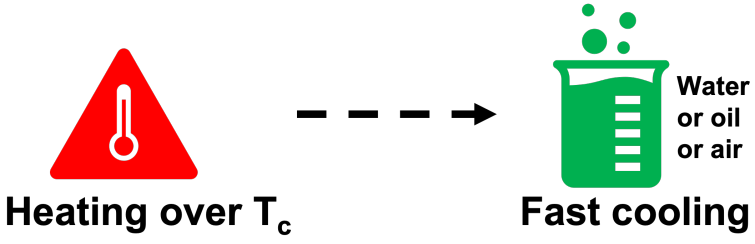

Figure 4.2: Schematic of quenching treatment. It consists in a heating of the sample followed by a fast cooling steps.

4.1.2 Disordering oxygen vacancies breaks defect dipoles

Strategy 4.2 — Fatigue treatment. Fatigue treatment consists in applying a rectangular electric excitation signal to the ceramic thousands times, as shown in Figure 4.3. This treatment allows to investigate the influence of the amplitude and the frequency of the excitation signal as well as of an offset voltage or the number of polarization reversal. Here, doped $BaTiO_3$ ceramics were oscillated 10^5 cycles under 24.4 kV cm^{-1} (frequency was kept at 10 Hz) at room temperature by using the Piezoelectric Evaluation System (TF analyzer2000E with FE-mode, Germany). The hysteresis loops were measured in between the fatigue cycles.

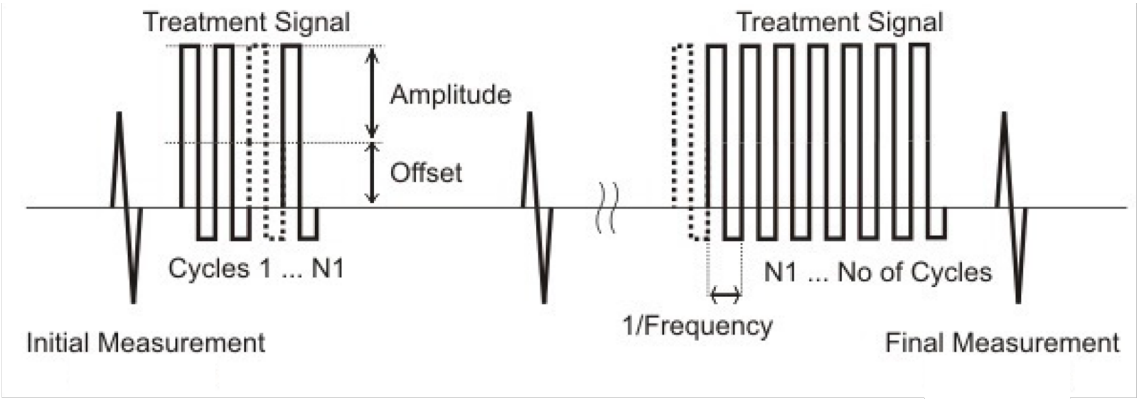

Figure 4.3: Schematic of fatigue treatment (TF analyzer 2000E with FE-mode, AixAcct). The rectangular excitation signal can be applied on the sample thousands of times. Between the fatigue cycles, the hysteresis-loop measurements are executed.

Besides quenching treatment, another procedure to open a pinched loop is the fatigue treatment where an oscillating electric field is applied numerous times on the sample, as shown in Figure.4.1(b). With the increase of the fatigue-cycling number, oxygen vacancies are gradually disordered, breaking defect dipoles. As a result, the pinched hysteresis loop (black curve) of 0.4 at%Cu-doped $BaTiO_3$ is gradually opened accompanied by symmetrical increase of the remanent polarization, saturation polarization, and coercive field from the first cycle to the 10^5-th cycle. A sharp open hysteresis loop (red curve) is finally presented. The fatigue characteristics including loop opening speed and sample fatigue endurance depend on the nature of the ferroelectric material itself, the type of dopants and their concentration, the temperature, and the field profile, among other parameters.[156, 157, 158, 159, 160]

The induced open hysteresis loop (akin to classical ferroelectrics) is nevertheless only metastable and will lead, at thermodynamic equilibrium, to a pinched loop or asymmetric loop. This stems from the orientation of the intrinsic ferroelectric domains prior to the onset of defect dipoles (when oxygen vacancies reach a dopant): the random orientation of the quenched domains will induce a random orientation of the defect dipoles which creates a restoring force pinching the hysteresis loops. The domains aligned by the last application of the electric field of fatigue treatment will align defect dipoles, which results in the shifted hysteresis loop.

4.2 Randomizing the orientation of defect dipoles causes hysteresis loop re-aging

Re-pinching an opened hysteresis loop is called re-aging. It can be achieved once the defect dipoles with randomized orientation are formed. Keeping the sample above T_C disorders the oxygen vacancies and then slowly cooling the sample in the furnace under zero field gives enough time for oxygen vacancies diffusion, the defect dipoles adopting a random orientation are created.

Consequently, the sample exhibits re-pinched hysteresis loop, as shown blue curve in Figure.4.4. Keeping quenched sample for two weeks also enables disordered oxygen vacancies to have enough time to reach positions that are nearest neighbor to dopants, forming randomly orientated defect dipoles. As shown in Figure.4.4, the open hysteresis loop (black dotted curve) of the quenched sample is pinched (violet curve). Re-pinching process is achieved thanks to the random orientation of intrinsic dipoles (in the "virgin" state) resulting in a zero net polarization in ceramics.[47] The random orientation of the ferroelectric domains combined with the eventual presence of defect dipoles give rise to the restoring force that induces the pinching.

The re-aging process not only involves the nucleation and growth of domains,[111] but is also driven by the reorientation of defect dipoles. Hence, the ability to re-age doped ferroelectrics depends on the type of dopants, their concentration, and thermal activation.[161, 162]

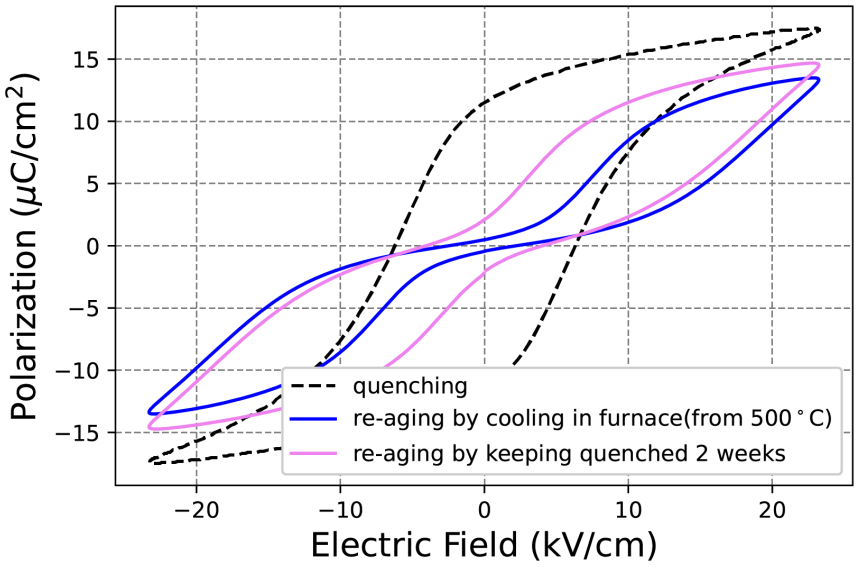

Figure 4.4: Re-pinched hysteresis loops of quenched 0.4 at%Cu-doped $BaTiO_3$. The open loop ("quenching", dotted black curve) is measured immediately after quenching the sample from above T_C and results from the disordering of the oxygen vacancies. Keeping this quenched sample for two weeks at room temperature, the disordered oxygen vacancies diffuse to positions nearest-neighbor to dopants, which forms defect dipoles and pinches the hysteresis loop (violet curve). Cooling the sample from 500°C (over T_C) in air also gives enough time for the diffusion of oxygen vacancies and the formation of defect dipoles, pinching the hysteresis loop (blue curve) as a consequence. All hysteresis loops were measured by the Piezoelectric Evaluation System (TF analyzer 2000E with FE-mode, AixAcct) without prepolarization and leakage compensation. The sample pasted by silver was immersed in silicon oil during the test to prevent flashover. A sinusoidal electric field with 5 Hz of frequency was applied.

4.3 Aligning defect dipoles causes asymmetric hysteresis loop

4.3.1 Horizontally shifting hysteresis loop

According to the symmetry-conforming principle of point defect, once equilibrium is reached, the defect dipoles are orientated along the spontaneous polarization of their corresponding domain. By the using field cooling treatment, domains are firstly orientated preferentially along the applied bias electric field and then defect dipoles are induced similarly preferential orientation, which is illustrated by the schematic in the Figure.4.5. These defect dipoles act as an effective internal bias field.[23, 47] and a larger opposite external field is therefore needed to switch the polarisation. This increases the corresponding coercive field ($\|E_c^-\| > E_c^+$) and causes the asymmetric hysteresis loop,

as if shifting the whole hysteresis loop horizontally when measured with an alternating external field applied along the polar axis[4, 47], as shown in Figure.4.5(a). The non-zero initial polarisation almost equal to the remanent polarisation evidences the effect of field cooling.

As the defect dipoles eventually point along the direction of the electric field (E_{pol}) was applied during field-cooling treatment, they can provide a perpendicular restoring force when the sample is measured perpendicular to the poling direction (E-field $\perp$ E_{pol}). Consequently, a slightly pinched hysteresis loop is obtained, as shown in Figure.4.5(b). The almost zero initial polarisation is because few intrinsic dipoles point along this perpendicular direction. And for those who do, they have a random orientation in that plane, the average polarization is therefore almost zero. Compared with the hysteresis loop that is measured along the poling direction (E-field // E_{pol}), this pinched hysteresis loop displays a reduced saturation polarisation. This is because the majority of defect dipoles still point along the poling direction and therefore hinder the rotation of their surrounding (intrinsic) domains to follow the electric field perpendicular to the poling direction.

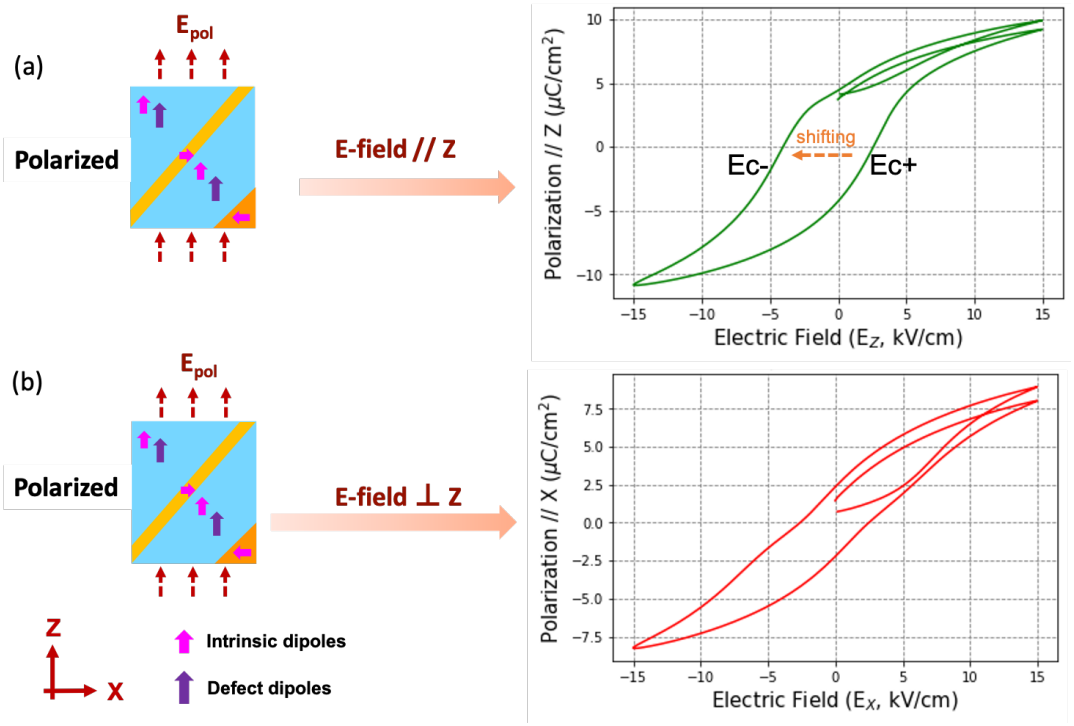

Figure 4.5: Hysteresis loops of field-cooled (15 kV cm^{-1}) 0.4 at%Cu-doped $BaTiO_3$ measured under a one-and-half-cycle sinusoidal electric field with 5 Hz of frequency (a) along the direction of the poling field (E_{pol}) and (b) along an orthogonal direction. The prepolarization and leakage compensation were not applied. Preferentially-oriented defect dipoles (a) shift the hysteresis loop along the poling field axis and (b) cause a slight pinching of the hysteresis loop measured with a measuring field along an direction orthogonal to the poling direction.

The higher bias field applied during field cooling, the larger proportion of aligned defect dipoles. As a consequence, the corresponding hysteresis loop can be shifted further. Figure.4.6(a) shows the shifted hysteresis loops with different E_c asymmetry that are induced by increasing bias fields, the positive value of coercive field (E_c^+) is even almost equal to 0 kV cm^{-1} when the applied bias field reach to 23.2 kV cm^{-1}. It should be note that Figure.4.6(a) does not correspond to a cumulative effect. Indeed, between every field-cooling treatment the samples were quenched to room temperature in water from the high-temperature paraelectric phase (150 °C for 10 minutes). The hysteresis loops measured just after quenching are represented by the dotted line in Figure.4.6(a) and superpose onto each other. The corresponding hysteresis loops indicate that the heating of

the sample above T_C randomizes the oxygen vacancies positions. When the sample is quenched to room temperature, the oxygen vacancies are not given the time to diffuse to a position nearest neighbor to the dopants and form defect dipoles before measurements are carried out.

Shifting the hysteresis loops decreases significantly the opposite remanent polarisation (P_r^-) without changing much the remanent polarisation along the direction of the bias field used to polarise the sample (P_r^+), as shown in Figure.4.6. This increases the recoverable energy storage (W_{reco}) for unipolar measurements in the direction opposite to the field used in field cooling, as illustrated in Figure.4.6(b). Compared to the unpolarized state, the relative increase in energy storage density reaches more than 50% (Figure.4.6(b)).

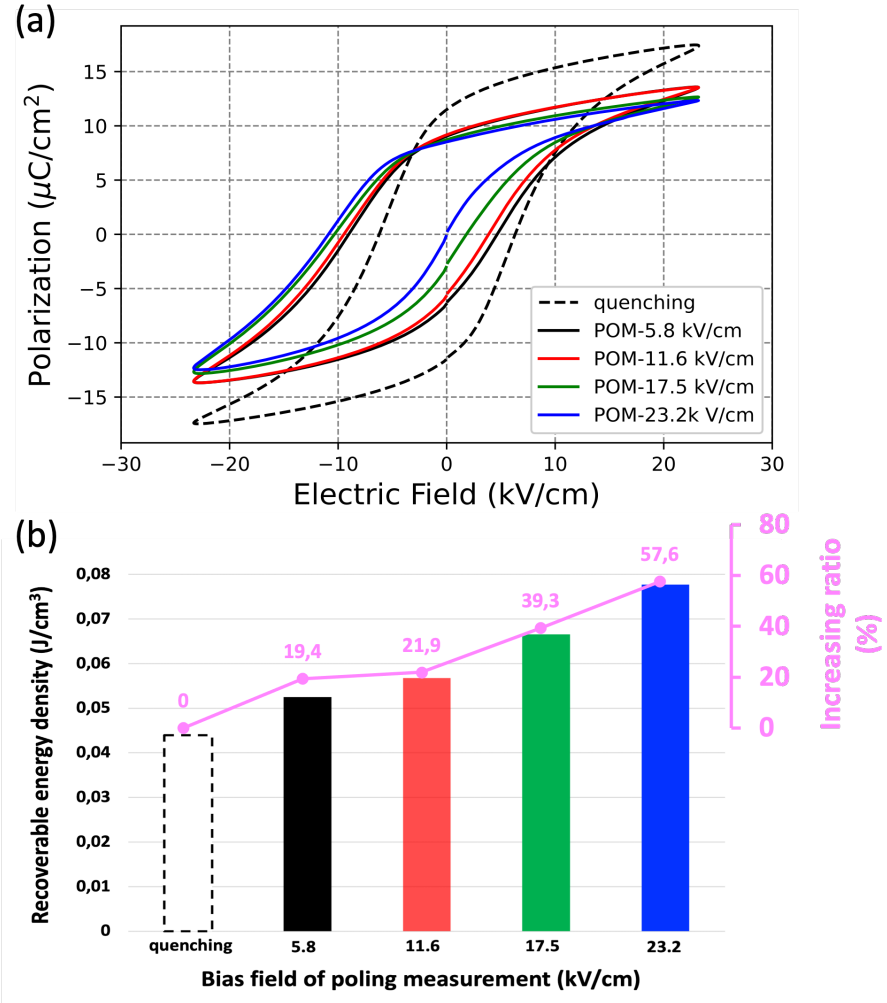

Figure 4.6: (a) Shifted hysteresis loops of 0.4 at% Cu-doped $BaTiO_3$ along the field axis caused by field-cooling treatment with different bias voltage (solid lines), compared to the hysteresis loop measured on the same sample, measured immediately after quenching (dotted black line). Between every field-cooling treatment, the sample is "reset" by quenching it from the paraelectric phase under zero field (heated for 10 minutes to 150 °C and then dropped into water for cooling). All hysteresis loops were measured by applying a 5 Hz of sinusoidal electric field without leakage compensation at room temperature. (b) The recoverable energy storage density of each loop was calculated by integrating the area between the loop and negative polarization axis and their respective increasing ratios compared to the non-shifted loop of the quenching state.

Strategy 4.3 — Field cooling. As shown in Figure.4.7, field cooling treatment consists in both a thermal and a field activation in order to effectively align the defect dipoles with ferroelectric domains (intrinsic dipoles). The treatments were carried out by using the Piezoelectric Evaluation System (TF analyzer2000E with FE-mode, Germany). The samples are first heated over T_C (to 150 °C) without electric field, where $BaTiO_3$ is the paraelectric phase and no ferroelectric domain exists.[47] Then, the samples are slowly cooled in the air to room temperature under a constant electric field, resulting in a preferential orientation of the domains *i.e.* polarising the sample. At thermodynamic equilibrium, the defect dipoles align with the domains and thereby acquire a preferential orientation according to the symmetry-conforming principle of point defect. This preferential orientation is along the direction of the applied poling field.

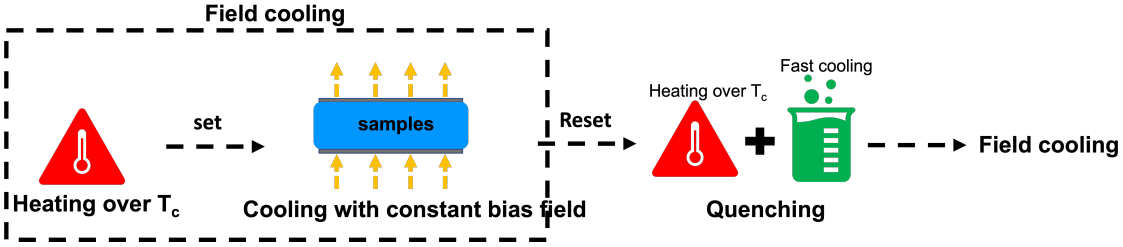

Figure 4.7: Schematic illustrates the field cooling treatment. The ceramcis are heated over T_C without electric field and then cooled to room temperature under a constant bias electric field. Through quenching treatment, the ceramics are reset and field-cooling effect are eliminated, which allows to investigate the influence of the amplitude of the bias field and the cooling speed.

4.3.2 Finally becoming a humming-bird-like hysteresis loop

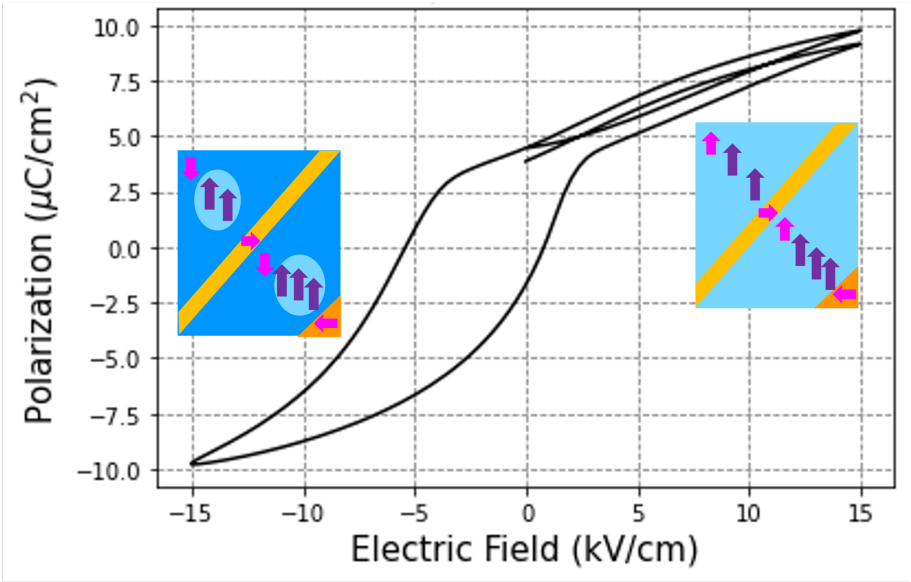

Figure 4.8: Humming-bird-like hysteresis loop for 0.4 at%Cu-doped $BaTiO_3$ caused by the preferential orientation of defect dipoles. Before measurement, the sample was treated by field cooling and then left for two weeks. Hysteresis loop was measured at room temperature under a one-and-half-cycle sinusoidal electric field with 5 Hz of frequency along the direction of the poling field. Under positive electric field (majority orientation of defect dipoles), domains rotation is easy (small E_c) with low hysteresis loss. Under reverse electric field, domain reversal is sluggish with larger hysteresis losses and higher coercive field.

The shifted hysteresis loop can naturally turn into the an hummingbird-like shape after several days, as shown in Figure.4.8. Such loop is characterised by a strong asymmetry with the "beak" indicating the majority orientation of the defect dipoles. The very strong restoring force from aligned defect dipoles (reaching an equilibrium configuration) ease domains rotation under positive electric field (i.e. along defect dipoles majority orientation), which results in a small value of the coercive field and reduced hysteresis losses. Under reverse electric field, domain reversal is sluggish with larger hysteresis losses and requires a higher coercive field value.

4.4 Summary

Summary 4 Based on the defect dipoles configuration process and the interaction between defect dipoles and ferroelectric domains, several strategies including thermal and field excitation are designed to achieve the manipulations of hysteresis loop of doped $BaTiO_3$. The de-aging process corresponding to opening a pinched hysteresis loop is obtained by inducing a temporary absence of defect dipoles. This can be achieved immediately after having quenched the sample from its paraelectric phase to room temperature or through fatigue measurements. In both cases, the oxygen vacancies are disordered away from the dopants and therefore do not create defect dipoles. The deaged states are nevertheless only metastable and will lead, at thermodynamic equilibrium, to a pinched loop once the oxygen vacancies have had the time to reach positions nearest-neighbor to dopants and form defect dipoles with randomized orientation. The driving force is the symmetry-conforming principle. When defect dipoles are induced a preferential orientation through field cooling treatment, shifted hysteresis loops along the field axis are created. Such effect is exacerbated as more and more defect dipoles align and a hummingbird-like hysteresis is eventually generated, with the "beak" along the direction of the majority defect dipoles. These manipulations of hysteresis loop shape and position enable to enhance ferroelectrics use for the various applications.

5. Lifetime of defect dipoles

Manipulations of ferroelectric hysteresis loops, including re-aging, shifting, and bird-like shaping, is attributed to defect dipoles.[51, 47, 163, 118] As oxygen vacancies reach positions nearest neighbor to dopants, defect dipoles are created. Oxygen vacancies hopping between various positions of the oxygen octahedra cause the re-orientation of defect dipoles. The defect dipoles disappear as oxygen vacancies leave the immediate vicinity of the dopants, leading to the deaged (unaged) state of acceptor-doped ferroelectrics. Deaged ferroelectrics display large remanent polarisation (P_r), which is undesired. As shown in Figure.5.1, deaged 0.4 at%Cu-doped $BaTiO_3$ caused by quenching treatment presents a large hysteresis loop with larger hysteresis loss and higher remanent polarization than pure $BaTiO_3$. As a result, a lower recoverable energy storage density of 0.4 at%Cu-doped $BaTiO_3$ (0.053 J cm^{-3}) than that of pure $BaTiO_3$ (0.073 J cm^{-3}) is clearly observed. In addition, deaged acceptor-doped $BaTiO_3$ and acceptor-doped PZT exhibit lower piezoelectric coefficients than their undoped counterparts.[29, 60, 30] Hence, the lifetime of defect dipoles has to be considered for engineering properties of acceptor-doped ferroelectrics. Here, the experiments backed up by DFT calculations were performed to investigate the preferential orientation and mobility of oxygen vacancies, enabling to compare the lifetime of defect dipoles in different acceptor-doped $BaTiO_3$.

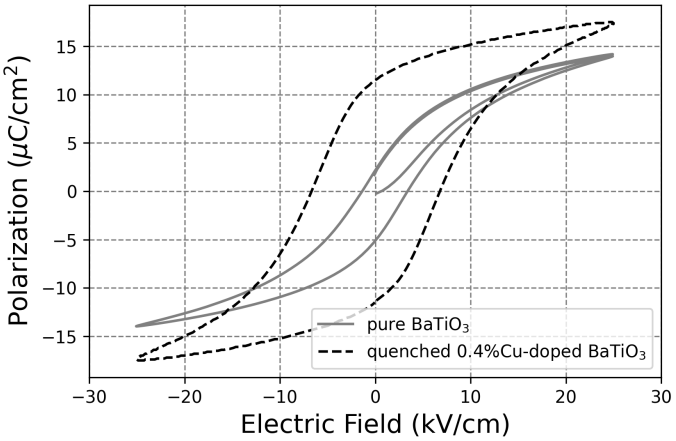

Figure 5.1: Due to the absence of defect dipoles, deaged 0.4 at%Cu-doped $BaTiO_3$ caused by quenching treatment shows larger hysteresis loss and higher remanent polarization than pure $BaTiO_3$. In addition, the recoverable energy storage density of quenched 0.4 at%Cu-doped $BaTiO_3$ (0.053 J cm^{-3}) is lower than that of pure $BaTiO_3$ (0.073 J cm^{-3}). All hysteresis loops were measured by applying a 5 Hz of sinusoidal electric field without leakage compensation at room temperature.

5.1 Defect dipoles preferentially orientate towards spontaneous polarization

As the association of oxygen vacancies and dopants creates defect dipoles, their lifetime are decided by the mobility of oxygen vacancies. The oxygen vacancies hopping between various positions next to the dopants directly results in defect dipoles appearing, vanishing, or rotating. By using DFT calculations[164, 165, 166, 167], the energy barriers that oxygen vacancies have to overcome to jump between various sites of the oxygen octahedra in acceptor(Cu, Fe)-doped $BaTiO_3$ and undoped $BaTiO_3$ at 0 K are obtained. As $BaTiO_3$ is in a rhombohedral phase at 0 K, symmetry-equivalent oxygens in octahedra are separated into two groups: $O_1O_2O_3$ in the triangle along spontaneous polarization (along $[11\bar{1}]$) and $O_4O_5O_6$ opposite the spontaneous polarization (see the insert of Figure.5.2(a)). When oxygen vacancies hop within a triangle, defect dipoles are rotated, but continue to point along or opposite to the spontaneous polarization. As oxygen vacancies diffuse between triangles along or opposite spontaneous polarization, defect dipoles are flipped. According to hopping paths of the oxygen vacancies, the energy barriers are classified into three types: $E_{//P_s}$, the energy barriers between non-symmetry-equivalent positions along the spontaneous polarization, such as $O_5 \rightarrow O_2$; E_{rotate}, the energy barriers between symmetry-equivalent positions, such as $O_1 \rightarrow O_2$ and $O_5 \rightarrow O_4$; and $E_{//\overline{P_s}}$, the energy barriers between non-symmetry-equivalent positions against the spontaneous polarization, such as $O_2 \rightarrow O_5$. Figure.5.2 (a) shows the energy barriers in Fe-doped $BaTiO_3$. One can observe that $E_{//P_s}$ (O_5O_2) = 1 eV, E_{rotate} (O_1O_2) = 1.05 eV, E_{rotate} (O_5O_4) = 1.1 eV, and $E_{//\overline{P_s}}$ (O_2O_5) = 1.2 eV. The same energy barriers ranking is also observed on Cu and Fe-doped $BaTiO_3$ (Figure.5.2 (b)). The lowest energy barrier of oxygen vacancies movement from $O_5 \rightarrow O_2$ therefore induce the preferential orientation of defect dipoles along the spontaneous polarization of $[11\bar{1}]$. This result is consistent with the symmetry-conforming principle of point defects.[61]

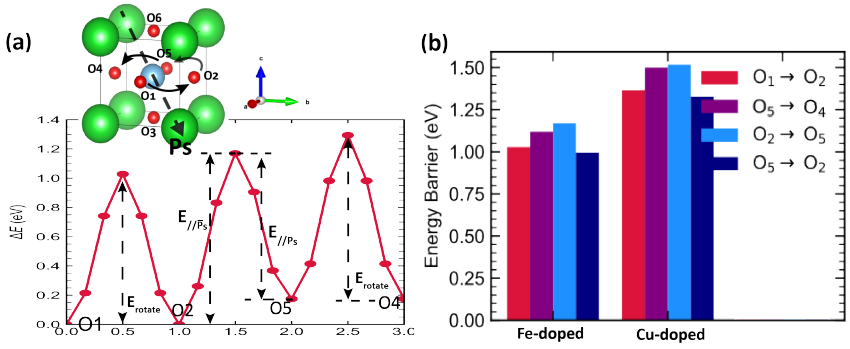

Figure 5.2: (a) Energy barrier for the diffusions of oxygen vacancies between various sites of octahedra in rhombohedral oxygen-deficiency Fe-doped $BaTiO_3$. Because $BaTiO_3$ is rhombohedral at 0 K, there are two triangles of non-equivalent oxygens $O_1O_2O_3$ along spontaneous polarization $[11\bar{1}]$ and $O_4O_5O_6$ opposite the spontaneous polarization (see insert). When oxygen vacancies diffuse between non-symmetry-equivalent positions along the spontaneous polarization, $E_{//P_s}$ (O_5O_2) = 1 eV. Between symmetry-equivalent positions, E_{rotate} (O_1O_2) = 1.05 eV, E_{rotate} (O_5O_4) = 1.1 eV. Between non-symmetry-equivalent positions against the spontaneous polarization, $E_{//\overline{P_s}}$ (O_2O_5) = 1.2 eV. The lowest energy barrier of oxygen vacancies movement is from $O_5 \rightarrow O_2$ therefore induce the preferential orientation of defect dipoles, which is the spontaneous polarization (along $[11\bar{1}]$). This conclusion is exactly consistent with the description of symmetry-conforming principle of point defect.[68, 69] (b) Comparison of the energy barriers in different doped $BaTiO_3$. Lower energy barriers in Fe-doped $BaTiO_3$ than in Cu-doped $BaTiO_3$ are observed regardless of the diffusing direction of the oxygen vacancies, indicating mobile defect dipoles in Fe-doped $BaTiO_3$

Apart from being decided by oxygen vacancies movement, defect dipoles are also dependent on the dopants, as shown in Figure.5.2 (b). Compared with Cu-doped $BaTiO_3$, Fe-doped $BaTiO_3$ has lower energy barriers regardless of the diffusing direction of the oxygen vacancies. This comparison indicates the higher mobility of oxygen vacancies in Fe-doped $BaTiO_3$ than in Cu-doped counterparts. The more mobile oxygen vacancies ease the rotation and the quick vanishing of defect dipoles, reflecting the shorter lifetime of defect dipoles.

According to the transition state theory (Equation.(5.1))[168, 169], energy barriers are related to the hopping probability rate of oxygen vacancies. With increasing temperature to the room temperature even over T_C, the ν_0 value, diffusion coefficient of defect, and the activation energy are changed. In addition, the symmetry of $BaTiO_3$ changes.[170, 171, 172] Therefore, so far, the DFT calculation results are only illustrative[173, 174] and the further exact calculations carried out on tetragonal $BaTiO_3$ at room temperature are needed to obtain the lifetime of defect dipoles in real samples. To investigate the mobility of oxygen vacancies in real acceptor-doped $BaTiO_3$ ceramics, we proposed two experiments: field cooling and fatigue measurement. These experiments both prove the DFT calculations.

$$\nu_{AB} = \nu_0 e^{-\frac{\Delta E}{k_b T}} \tag{5.1}$$

where ΔE is the energy barrier, ν_{AB} is the hopping probability rate of oxygen vacancies to go from site A to site B, and ν_0 is the an attempt frequency to determine, which is general fixed to 10^{+13} Hz.

Technique 5.1 — Density functional theory (DFT) calculations (carried out by Dr. Charles Paillard, Laboratoire SPMS, CentraleSupélec). The objective was to the obtain energy barriers heights between the octahedra sites in oxygen-deficient $BaTiO_3$ and acceptor (Cu,

Fe)-doped $BaTiO_3$. DFT calculations were performed on 3 × 3 × 3 supercells (135 atoms). The projector augmented wave (PAW) method with the Perdew-Burke- Ernzerhof functional was modified for solids (PBEsol). A 1 × 1 × 1 Monkhorst-Pack k-point mesh and a plane wave cut-off of 550 eV were employed. The energy barriers were estimated using the Climbing Image NEB method as implemented in the VTST tod suite for VASP (Henkelman group at UT Austin). 5 images were used to estimate the transition state energy barriers.

5.2 Fe-doped $BaTiO_3$ has more mobile defect dipoles compared to Cu-doped $BaTiO_3$

Inspired by the DFT calculations, we performed two experiments to investigate the mobility of oxygen vacancies, comparing the lifetime of defect dipoles in $BaTiO_3$ doped with different acceptors. During the field cooling treatment, defect dipoles re-orientate as oxygen vacancies adopt the same orientation as their surrounding polarized domains, which shifts the hysteresis loop with asymmetric coercive fields. The mobility of oxygen vacancies can be evaluated by observing the shift of the coercive fields as a function of the applied cooling fields. In fatigue treatment, defect dipoles disappear as oxygen vacancies disorder, which gradually opens the pinched hysteresis loop as more and more defect dipoles disappear accompanied by an increase of the remanent polarization (P_r^+). The evolution of remanent polarization therefore can be used to assessing the mobility of oxygen vacancies. The short lifetime of defect dipoles is reflected by the high mobility of oxygen vacancies.

5.2.1 Defect dipoles are more easily aligned in Fe-doped $BaTiO_3$ than in Cu-doped $BaTiO_3$

The DFT calculations show that oxygen vacancies diffusion spontaneously follows the spontaneous polarization of ferroelectrics. Thus we carried out the field cooling treatment to induce a spontaneous polarization in acceptor-doped $BaTiO_3$. As a consequence, this induced state align the oxygen vacancies and the defect dipoles reorientate along the same direction, which leads to the shifted hysteresis loops. The higher the mobility of the oxygen vacancies, the more defect dipoles are reorientated, which results in a larger shift of the hysteresis loops.

The shifted hysteresis loops of 0.4 at%Cu-doped $BaTiO_3$ and 0.5 at%Fe-doped $BaTiO_3$ caused by different applied electric field in field-cooling treatment are shown in Figure.5.3(a). Between every field-cooling treatment, the samples were reset by quenching. Higher bias electric (from 2.5 to 35 $kV\,cm^{-1}$) applied in the field-cooling treatment align more defect dipoles, resulting in a further shift of the hysteresis loop towards the negative electric field values and increase E_c asymmetry. The shifting of hysteresis loops by the increase of the applied bias field and the corresponding decreasing of the positive coercive field (E_c^+) are observed on the 0.4 at%Cu-doped $BaTiO_3$. If oxygen vacancies in 0.5 at%Fe-doped $BaTiO_3$ are more mobile, more shifted hysteresis loops with larger reduction of positive coercive field are expected. However, the hysteresis loops of field-cooled 0.5 at%Fe-doped $BaTiO_3$ are almost identical when applied bias field is above 5 $kV\,cm^{-1}$. This phenomenon indicates that almost all defect dipoles in 0.5 at%Fe-doped $BaTiO_3$ finish alignment, and the shifting of the hysteresis loop reaches saturation. The 0.4 at%Cu-doped $BaTiO_3$ still has defect dipoles that need to be aligned, which leads to the hysteresis loop continuous shift. The humming-bird shapes of hysteresis loops of 0.5 at%Fe-doped $BaTiO_3$ when the applied bias field is above 5 $kV\,cm^{-1}$ also implies the saturation of saturation of defect dipoles.[175]

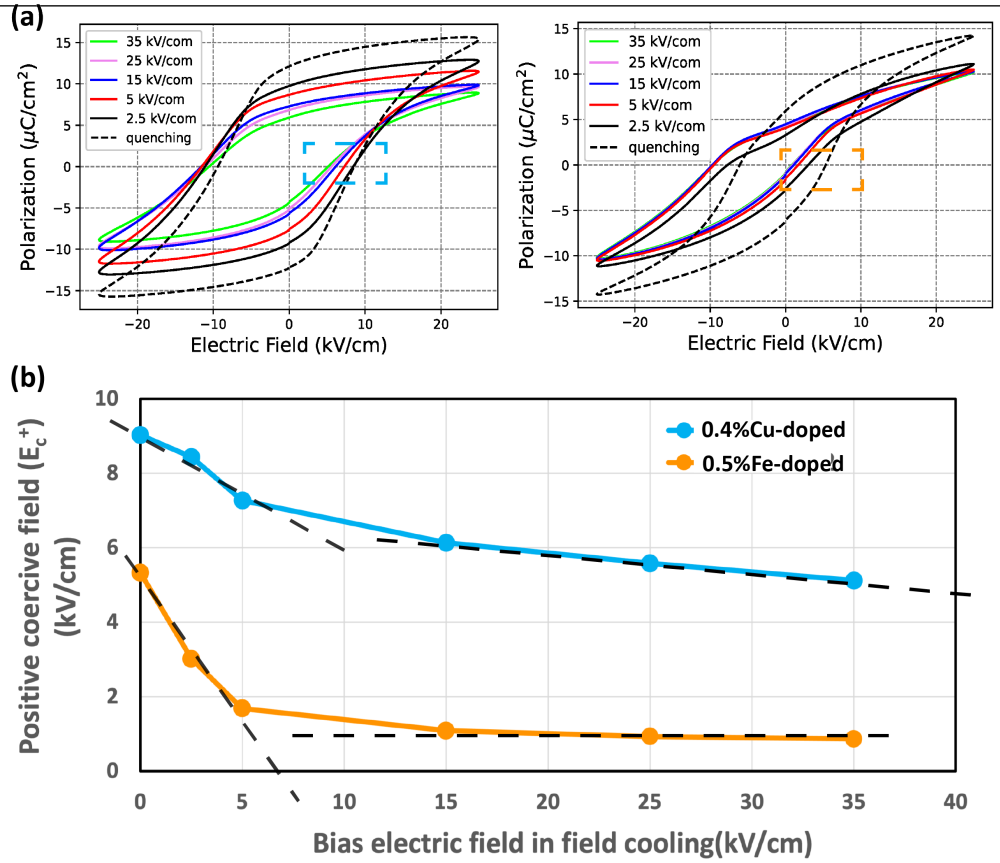

Figure 5.3: (a) Shifted hysteresis loops for various bias electric field amplitudes (from 2.5 to 35 kV cm^{-1}) used during field cooling treatment for 0.4 at%Cu-doped $BaTiO_3$ (left) and 0.5 at%Fe-doped $BaTiO_3$ (right). Between every field-cooling treatment, the samples were reset by quenching. The hysteresis loops of the quenched sample are superposed (dotted black line in panel (a)) to present the non-shifted state. The hysteresis loops were measured by using Piezoelectric Evaluation System (TF analyzer 2000E with FE-mode, AixAcct) without prepolarization and leakage compensation. Each measurement perform a positive pulse and a negative pulse to generate a closed hysteresis loop. (b) The positive coercive field (E_c^+) of doped $BaTiO_3$ as a function of applied bias electric field to more clearly show hysteresis loops shift caused by field cooling treatment. The E_c^+ values of quenched hysteresis loops correspond to a 0 kV cm^{-1} applied bias electric field. The broken black lines show the trend of decreasing positive coercive field as applied bias electric field is increased. The positive coercive field of 0.4 at%Cu-doped $BaTiO_3$ continuously decreases when the applied bias electric field is up to 35 kV cm^{-1}. The positive coercive field of the 0.5 at%Fe-doped $BaTiO_3$ drastically decreases at first and then remains almost constant as the applied bias electric field is over 15 kV cm^{-1}. This almost constant positive coercive field indicates the saturation of defect dipoles alignment in Fe-doped $BaTiO_3$.

The saturations of defect dipoles alignment in acceptor-doped $BaTiO_3$ are further investigated by the positive coercive field value (E_c^+) as a function of the applied bias electric field, as shown in Figure.5.3(b). The E_c^+ values of 0.4 at%Cu-doped $BaTiO_3$ continuously decrease when the applied bias electric field is up to 35 kV cm^{-1}. For the 0.5 at%Fe-doped $BaTiO_3$, the E_c^+ value drastically decreases at first until 5 kV cm^{-1} and then remains almost constant as the applied bias electric field is over 15 kV cm^{-1}. This faster reduction and easier stabilization of the coercive field illustrates the saturation of defect dipoles alignment in Fe-doped $BaTiO_3$. This saturation of the defect dipoles alignment in Fe-doped $BaTiO_3$ by a lower electric field in field-cooling treatment demonstrates

the higher mobility of oxygen vacancies in 0.5 at%Fe-doped $BaTiO_3$ than in 0.4 at%Cu-doped $BaTiO_3$.[175, 176, 177, 159]

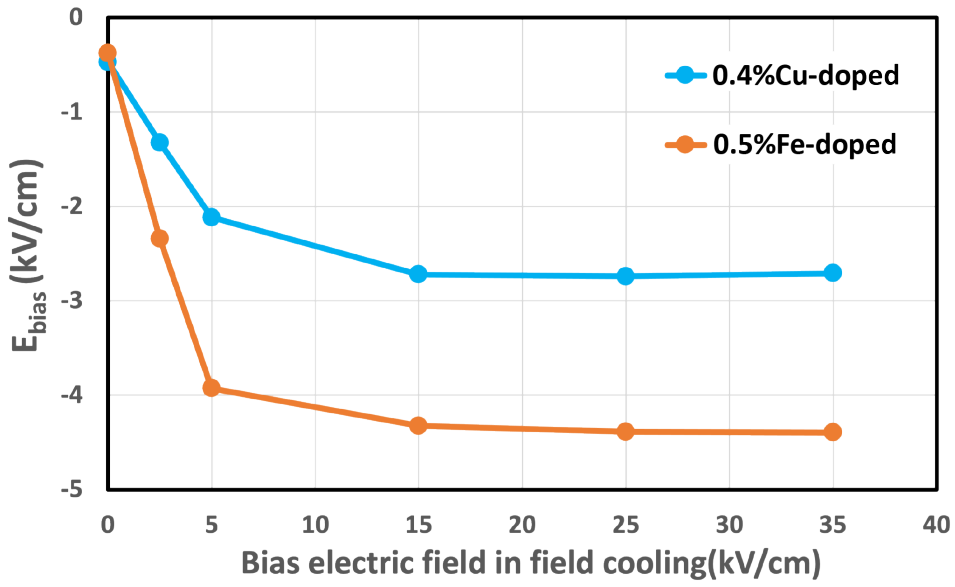

Figure 5.4: The evolution of bias coercive field (E_{bias}) as a function of applied bias electric fields in field cooling treatments. Between every field-cooling treatment, the samples were reset by quenching. The E_{bias} values of quenched hysteresis loops correspond to a 0 kV cm^{-1} applied bias electric field. The faster and larger reduction of E_{bias} of 0.5 at%Fe-doped $BaTiO_3$ indicates the higher mobility oxygen vacancies.

In addition, the shift of the hysteresis loop can be evaluated through the bias coercive fields (E_{bias}) which are calculated through Equation.(5.2). As shown in Figure.5.4, the E_{bias} values drastically decreases until 15 kV cm^{-1} is applied in field cooling. Compared with 0.4 at%Cu-doped $BaTiO_3$, the 0.5 at%Fe-doped $BaTiO_3$ present faster and larger reduction of E_{bias}, confirming the less stability of oxygen vacancies in 0.5 at%Fe-doped $BaTiO_3$. These field cooling results are consistent with expectation from the DFT calculations.

$$E_{bias} = (E_c^+ + E_c^-)/2 \tag{5.2}$$

where bias coercive field (E_{bias}) indicates the shifting degree of hysteresis loop along the electric field axis caused by the field cooling treatment.

5.2.2 Defect dipoles disappear more easily in Fe-doped $BaTiO_3$ than in Cu-doped $BaTiO_3$

Another insight gained from DFT calculations is that oxygen vacancies can move against the spontaneous polarization when they obtain enough energy. We have therefore carried out the fatigue treatment to induce energies, making the random hopping of oxygen vacancies between various sites of the oxygen octahedra in acceptor-doped $BaTiO_3$. With increasing fatigue cycles, more and more oxygen vacancies are activated. These disordered oxygen vacancies lead to the temporary disappearance of defect dipoles. Consequently, pinched hysteresis loops of acceptor-doped $BaTiO_3$ are gradually opened. This defines the de-aging process. Through comparison of the opening speed of pinched hysteresis loops, the mobility of oxygen vacancies in different acceptor-doped $BaTiO_3$ can be assessed.

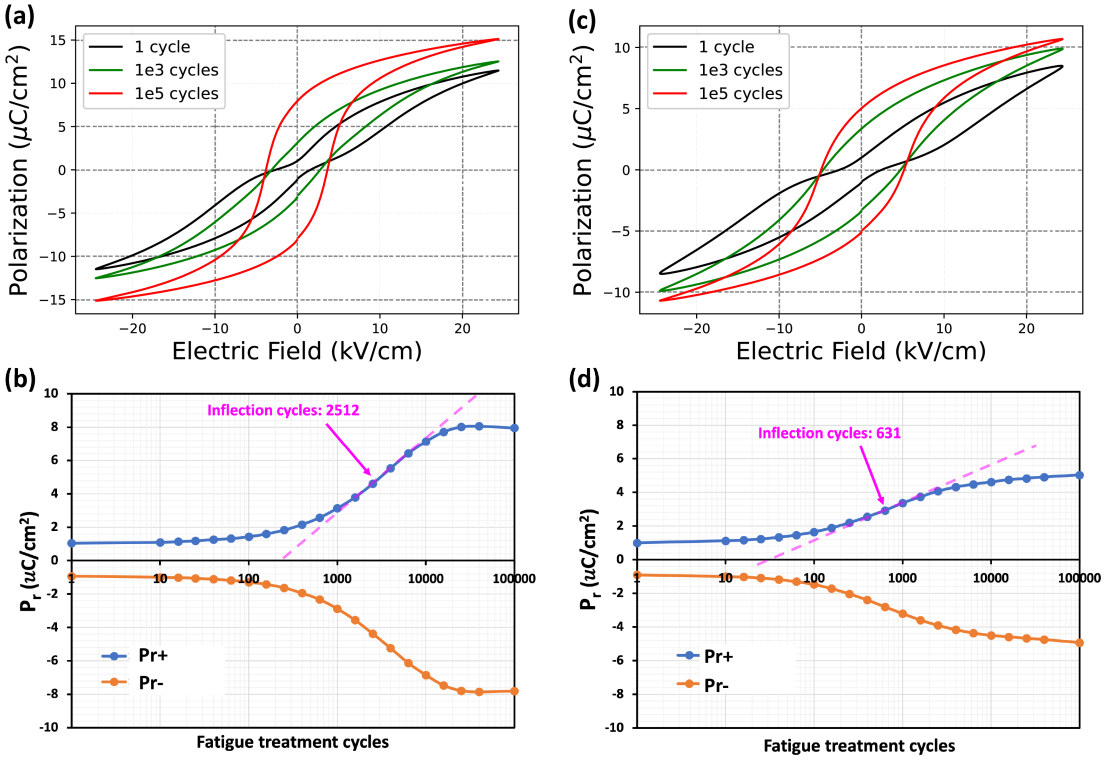

Figure 5.5: Comparing the mobility of oxygen vacancies in 0.4 at%Cu-doped $BaTiO_3$ (a and b) and 0.5 at%Fe-doped $BaTiO_3$ (c and d) by using fatigue treatment. The hysteresis loops were measured by using Piezoelectric Evaluation System (TF analyzer 2000E with FE-mode, AixAcct) without prepolarization and leakage compensation. Each measurement perform a positive pulse and a negative pulse to generate a closed hysteresis loop. As oxygen vacancies gradually disordering by increased fatigue cycles, defect dipoles gradually disappear, which results in the de-aging process: both pinched hysteresis loops of Cu-doped and Fe-doped $BaTiO_3$ both are gradually open (a and c). (b) and (d) respectively show the evolution of remanent polarization (P_r) of Cu-doped $BaTiO_3$ and Fe-doped $BaTiO_3$ in fatigue treatment. The approximate inflection points in the evolution of P_r^+ are the signal that the majority of the defect dipoles have disappeared.

The hysteresis loops of de-aged 0.4 at%Cu-doped $BaTiO_3$ and 0.5 at%Fe-doped $BaTiO_3$ caused by fatigue treatment are shown in Figure.5.5 (a) and (c) respectively. Both pinched hysteresis loops are gradually open accompanied by a symmetrical increase of remanent polarization (*i.e.* P_r^+ increases and P_r^- decreases) as the fatigue cycles increases. Because of defect dipoles disappearance, hysteresis loops of doped $BaTiO_3$ show open shape, and P_r is stable after 10^5 cycles. The Figure.5.5 (b) and (d) shows the evolution of P_r with increasing fatigue cycles numbers. In order to quantitatively describe the opening speed of pinched hysteresis loops, we propose two criteria. One is the inflection points in the evolution of P_r^+. The inflection points corresponding 2512 cycles of Cu-doped $BaTiO_3$ and 631 cycles of Fe-doped $BaTiO_3$ act as the signal that the majority of the defect dipoles have disappeared. Compared with 0.4 at%Cu-doped $BaTiO_3$, 0.5 at%Fe-doped $BaTiO_3$ shows an inflection point at a lower cycles, which denotes that quick vanishing of defect dipoles.

$$\eta = (P_{r-ncycle} - P_{r-1cycle})/P_{r-highest} \tag{5.3}$$

where η is the normalized P_r increase. Because of remanent polarization symmetry, only positive

remanent polarization ((P_r^+) values are used to calculate normalized P_r increase. $P_{r-ncycle}$ is the value of the remanent polarization after cycle n, P_{r-1st} is the value of remanent polarization of the first electric field cycle, and $P_{r-highest}$ is the highest value of remanent polarization at 10^5 cycles when the hysteresis loop is open.

Another possible criterion to evaluate the opening speed of pinched hysteresis loops is the normalized P_r increase, which is calculated through Equation.(5.3). The normalized P_r increase (η) as a function of fatigue treatment cycles are shown in Figure.5.6. The insert shows that the onset of normalized P_r increase of 0.5 at%Fe-doped $BaTiO_3$ occurs for a lower fatigue cycles numbers than that of 0.4 at%Cu-doped $BaTiO_3$. (insert of Figure.5.6), which indicates that defect dipoles in 0.5 at%Fe-doped $BaTiO_3$ first started disappearing. The high mobility of oxygen vacancies in 0.5 at%Fe-doped $BaTiO_3$ is therefore concluded. Moreover, it is observed that 0.5 at%Fe-doped $BaTiO_3$ displays the higher normalized P_r increase than 0.4 at%Cu-doped $BaTiO_3$ before 10000 cycles. This comparison demonstrates the fast opening speed of the pinched hysteresis loops of the 0.5 at%Fe-doped $BaTiO_3$. Hence, higher mobility of defect dipoles in Fe-doped $BaTiO_3$ than in Cu-doped $BaTiO_3$ is concluded by using fatigue treatment. This is also consistent with expectation from DFT calculations.

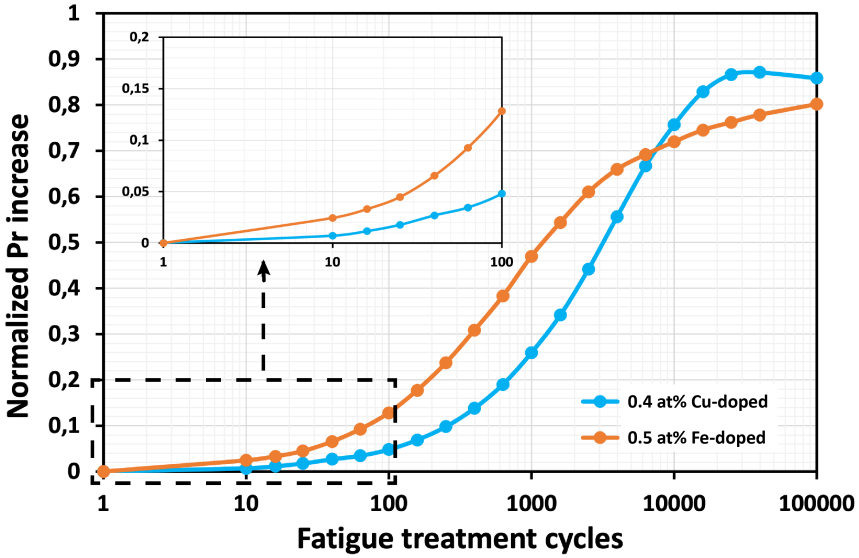

Figure 5.6: Normalized P_r increases (η) as function of fatigue treatment cycles. The insert shows that P_r-increase onset of 0.5 at%Fe-doped $BaTiO_3$ is before 10 cycles, which is lower than 0.4 at%Cu-doped $BaTiO_3$ (around at 40 cycles).

5.3 Summary

Summary 5 The existence of defect dipoles provides the possibility of manipulating ferroelectric hysteresis loop. However, the mobility of oxygen vacancies impacts the stability of defect dipoles. As oxygen vacancies leave positions next to dopants, the defect dipoles disappear, which causes undesired performances of acceptor-doped $BaTiO_3$, including lower energy storage density and low piezoelectric coefficient. By using DFT calculations, the preferential orientation of oxygen vacancies following the direction of spontaneous polarization has been established. This result is consistent with the symmetry-conforming principle of point defect.[68, 69] In addition, the energy barriers of oxygen vacancies diffusion calculated by DFT are lower in Fe-doped $BaTiO_3$ than in Cu-doped $BaTiO_3$, which indicates the higher mobility of oxygen vacancies. As DFT calculations are limited to the rhombohedral $BaTiO_3$ at 0 K, two experi-

ments were carried out to investigate the mobility of oxygen vacancies in tetragonal $BaTiO_3$ at room temperature. The first experiment is the field cooling. It induces a polarization to align oxygen vacancies. Consequently, defect dipoles are reorientated, leading to hysteresis loops shift. Compared with 0.4 at%Cu-doped $BaTiO_3$, 0.5 at%Fe-doped $BaTiO_3$ shows the saturation of the defect dipoles alignment by a lower electric field, which demonstrates higher mobility of oxygen vacancies. Another experiment is the fatigue treatment. Increasing fatigue cycles numbers gradually disorders the oxygen vacancies. The pinched hysteresis loops of acceptor-doped $BaTiO_3$ are therefore opened. The faster opening speed of the pinched hysteresis loop of 0.5 at%Fe-doped $BaTiO_3$ than that of 0.4 at%Cu-doped $BaTiO_3$ confirms the higher mobility of defect dipoles in Fe-doped $BaTiO_3$. The oxygen vacancies with high mobility distabilize defect dipoles, therefore, the shorter lifetime of defect dipole in 0.5 at%Fe-doped $BaTiO_3$ predicted by DFT calculations is concluded.

6. Summary

In summary, by inducing oxygen vacancies to form defect dipoles, the ferroelectric domain rotations are controlled, which enables tuning the properties of lead-free ferroelectric $BaTiO_3$ ceramics.

Acceptor doping is the intentional introduction of dopants with a lower valence than the ion they substitute in the base material. In this work, Cu^{2+} ($r_{Cu^{2+}} = 87$ pm) and Fe^{3+} ($r_{Fe^{3+}} = 78.5$ (69) pm for high (low) spin) are selected as acceptors to substitute for the Ti ions ($r_{Ti^{4+}} = 74.5$ pm) on the B site of the perovskite structure of $BaTiO_3$ through traditional solid-state synthesis method. The Fe and Cu substitutions in $BaTiO_3$ are demonstrated by the EPR spectra. The EPR spectra of Cu-doped $BaTiO_3$ show the presence of tetragonal Cu^{2+} center (CuT center), which consists of the Cu^{2+} localized substitutionally in the B site, and four O^{2-} in the equatorial plane, and the oxygen vacancy on the tetragonal axis (perpendicular to the equatorial plane). The simulated spectra of tetragonal Fe^{3+} centers are obtained from the spectra of Fe-doped $BaTiO_3$. Combined with the SEM images, Rietveld-refined XRD patterns, and Raman spectra, the perovskite structure of doped $BaTiO_3$ ceramics with a single tetragonal phase ($P4mm$) at room temperature are determined. The homogeneous Cu distributions are observed on the EDX maps.

The oxygen vacancies, either trapped by dopants or accumulated at grain boundaries, create an internal electric field, playing a crucial role to harden acceptor-doped ferroelectrics. According to these two trapping positions for the oxygen vancancies, the hardening mechanism is generally explained by the volume effect or the surface effect, respectively. As the mobile oxygen vacancies contribute to the conductivity of ferroelectric ceramic, we measure the local resistance maps of 0.4 at%Cu-coped $BaTiO_3$ at the hardened state and the relaxed state by using Resiscope measurement. The higher reduction of the interior of the grains resistance (ΔR_G) than the reduction of grain boundary resistance (ΔR_{GB}) when a hardened sample becomes relaxed demonstrates that the volume effect is the principal hardening mechanism in polycrystalline acceptor-doped ferroelectrics. The movements of ferroelectric domain walls are restricted by the defect dipoles that are created as oxygen vacancies reach positions nearest-neighbor to dopants. According to the symmetry-conforming principle of point defects, the orientation of defect dipoles follows the orientation of surrounding domains at thermodynamic equilibrium. Therefore, the defect dipoles provide a restoring force to quickly switch back surrounding domains to their initial orientations during the removal of the external field. Now, the interaction between oxygen vacancies and ferroelectric domains are clearly understood.

Inspired by this oxygen vacancies-domains interaction, we design several strategies including thermal and field excitation to control the oxygen vacancies migration, and manipulate the orientation of defect dipoles. Consequently, the domain walls movements are controlled, which makes

the acceptor-doped $BaTiO_3$ present different hysteresis loops. Through quenching and fatigue treatment, the de-aging process corresponding to the opening a pinched hysteresis loop is obtained due to a temporary absence of defect dipoles. The deaged states are nevertheless only metastable and will lead, at thermodynamic equilibrium, to a pinched loop once the oxygen vacancies have had the time to reach positions nearest-neighbor to dopants and form defect dipoles with randomized orientation. The field cooling treatment can induce a preferential orientation of defect dipoles, resulting in a shifted hysteresis loops along the field axis. Such effect is exacerbated as more and more defect dipoles align and a hummingbird-like hysteresis is eventually generated, with the "beak" along the direction of the majority defect dipoles.

The mobility of oxygen vacancies is a crucial factor that must be considered when using oxygen vacancies-domains interaction to tune ferroelectrics. The oxygen vacancies with high mobility can cause unstable defect dipoles, which affect the defect engineering of lead-free ferroelectric ceramics $BaTiO_3$. By using DFT calculations, the lowest energy barrier of oxygen vacancies movement is established, which follows the spontaneous polarization of rhombohedral $BaTiO_3$ ceramics. This result is consistent with the symmetry-conforming principle of point defects. In addition, the lower energy barriers of oxygen vacancies diffusion in Fe-doped $BaTiO_3$ than in Cu-doped $BaTiO_3$ are calculated by DFT, which indicates the higher mobility of oxygen vacancies in Fe-doped $BaTiO_3$. These DFT calculation results are backed up by two experiments. In field cooling measurement, 0.5 at%Fe-doped $BaTiO_3$ shows a saturation of the defect dipoles alignment by a lower electric field than in 0.4 at%Cu-doped $BaTiO_3$, which demonstrates the higher mobility of oxygen vacancies in Fe-doped $BaTiO_3$. During fatigue measurement, the faster opening of pinched hysteresis loop of 0.5 at%Fe-doped $BaTiO_3$ than that of 0.4 at%Cu-doped $BaTiO_3$ confirms the higher mobility of defect dipoles in Fe-doped $BaTiO_3$. Therefore, the stability of defect dipole in acceptor-doped ferroelectrics can be predicted by DFT calculations.

Bibliography

[1] Zechao Li et al. “Enhancing properties of lead-free ferroelectric BaTiO 3 through doping”. In: *Journal of the European Ceramic Society* 42.12 (2022), pages 4693–4701 (cited on pages 7, 9).

[2] Malcolm E Lines and Alastair M Glass. *Principles and applications of ferroelectrics and related materials*. Oxford university press, 2001 (cited on pages 13, 15, 18, 43, 45, 47).

[3] SM Said, MFM Sabri, and F Salleh. “Ferroelectrics and Their Applications”. In: (2017) (cited on page 13).

[4] Dragan Damjanovic. “Hysteresis in piezoelectric and ferroelectric materials”. In: *The science of hysteresis* 3 (2006), pages 337–465 (cited on pages 13, 16, 20, 45, 58, 61).

[5] Irinela Chilibon and José N Marat-Mendes. “Ferroelectric ceramics by sol–gel methods and applications: a review”. In: *Journal of sol-gel science and technology* 64.3 (2012), pages 571–611 (cited on page 13).

[6] JF Scott. “Applications of modern ferroelectrics”. In: *science* 315.5814 (2007), pages 954–959 (cited on page 13).

[7] Letao Yang et al. “Perovskite lead-free dielectrics for energy storage applications”. In: *Progress in Materials Science* 102 (2019), pages 72–108 (cited on pages 13, 16, 18, 28).

[8] Xihong Hao. “A review on the dielectric materials for high energy-storage application”. In: *Journal of Advanced Dielectrics* 3.01 (2013), page 1330001 (cited on pages 13, 16, 17, 54).

[9] Nava Setter and EL Colla. *Ferroelectric ceramics: tutorial reviews, theory, processing, and applications*. Springer, 1993 (cited on page 13).

[10] Dragan Damjanovic. “Ferroelectric, dielectric and piezoelectric properties of ferroelectric thin films and ceramics”. In: *Reports on Progress in Physics* 61.9 (1998), page 1267 (cited on pages 13, 15, 17–19, 43, 54).

[11] Shuangyi Liu et al. “Intrinsic dielectric frequency dependent spectrum of a single domain tetragonal BaTiO3”. In: *Journal of Applied Physics* 112.1 (2012), page 014108 (cited on page 13).

[12] G Arlt. “Twinning in ferroelectric and ferroelastic ceramics: stress relief”. In: *Journal of materials Science* 25.6 (1990), pages 2655–2666 (cited on page 15).

[13] Dennis Meier and Sverre M Selbach. “Ferroelectric domain walls for nanotechnology”. In: *Nature Reviews Materials* (2021), pages 1–17 (cited on pages 15, 18).

[14] YY Guo et al. “Kinetics controlled aging effect of ferroelectricity in Al-doped and Ga-doped BaTiO 3”. In: *Applied Physics Letters* 97.11 (2010), page 112906 (cited on page 16).

[15] Mohamad M Ahmad et al. “Aging-induced dielectric relaxation in barium titanate ceramics”. In: *Applied physics letters* 90.11 (2007), page 112902 (cited on page 16).

[16] Zhiyang Wang et al. “Enhanced Energy-Storage Density by Reversible Domain Switching in Acceptor-Doped Ferroelectrics”. In: *Physical Review Applied* 15.3 (2021), page 034061 (cited on pages 16, 18, 42).

[17] Lixue Zhang et al. “Reorientation of (Mn Ti - VO••)× defect dipoles in acceptor-modified BaTiO 3 single crystals: An electron paramagnetic resonance study”. In: *Applied Physics Letters* 93.20 (2008), page 202901 (cited on pages 16, 20, 53).

[18] Jiandang Liu et al. “Understanding doped perovskite ferroelectrics with defective dipole model”. In: *The Journal of chemical physics* 149.24 (2018), page 244122 (cited on pages 16, 53).

[19] T Schenk et al. “About the deformation of ferroelectric hystereses”. In: *Applied physics reviews* 1.4 (2014), page 041103 (cited on page 16).

[20] Bin Peng et al. “Improvement of the recoverable energy storage density and efficiency by utilizing the linear dielectric response in ferroelectric capacitors”. In: *Applied Physics Letters* 105.5 (2014), page 052904 (cited on page 16).

[21] Mao Ye et al. “Effect of Eu doping on the electrical properties and energy storage performance of PbZrO 3 antiferroelectric thin films”. In: *Journal of the American Ceramic Society* 94.10 (2011), pages 3234–3236 (cited on page 16).

[22] Venkata Sreenivas Puli et al. “Crystal structure, dielectric, ferroelectric and energy storage properties of La-doped BaTiO 3 semiconducting ceramics”. In: *Journal of Advanced Dielectrics* 5.03 (2015), page 1550027 (cited on page 16).

[23] KHHK Carl and KH Hardtl. “Electrical after-effects in Pb (Ti, Zr) O3 ceramics”. In: *Ferroelectrics* 17.1 (1977), pages 473–486 (cited on pages 16, 20, 42, 45, 46, 52, 60).

[24] Robert Alan Huggins. *Energy storage*. Volume 406. Springer, 2010 (cited on page 16).

[25] Gordon R Love. “Energy storage in ceramic dielectrics”. In: *Journal of the American Ceramic Society* 73.2 (1990), pages 323–328 (cited on page 16).

[26] Satyanarayan Patel, Aditya Chauhan, and Rahul Vaish. “Enhancing electrical energy storage density in anti-ferroelectric ceramics using ferroelastic domain switching”. In: *Materials Research Express* 1.4 (2014), page 045502 (cited on page 17).

[27] Juergen Roedel and Jing-Feng Li. “Lead-free piezoceramics: Status and perspectives”. In: *MRS Bulletin* 43.8 (2018), pages 576–580 (cited on page 17).

[28] Vincenzo Buscaglia, Maria Teresa Buscaglia, and Giovanna Canu. “BaTiO3-based ceramics: Fundamentals, properties and applications”. In: (2021) (cited on page 18).

[29] Matias Acosta et al. “BaTiO3-based piezoelectrics: Fundamentals, current status, and perspectives”. In: *Applied Physics Reviews* 4.4 (2017), page 041305 (cited on pages 18, 19, 43, 65).

[30] Thomas R Shrout and Shujun J Zhang. “Lead-free piezoelectric ceramics: Alternatives for PZT?” In: *Journal of Electroceramics* 19.1 (2007), pages 113–126 (cited on pages 18, 65).

[31] QM Zhang et al. “Direct evaluation of domain-wall and intrinsic contributions to the dielectric and piezoelectric response and their temperature dependence on lead zirconate-titanate ceramics”. In: *Journal of Applied Physics* 75.1 (1994), pages 454–459 (cited on pages 18, 41).

[32] Xiaolian Chao et al. “Aging behavior and electrical properties of low-temperature sintered (Ba, Ca)(Ti, Zr) O3-Ba (Cu, W) O3 ceramics and plate loudspeaker”. In: *Sensors and Actuators A: Physical* 237 (2016), pages 9–19 (cited on page 18).

[33] Suhana Mohd Said et al. “Ferroelectrics and their applications”. In: (2022) (cited on page 18).

[34] Shenglan Hao et al. “Optical absorption by design in a ferroelectric: co-doping in BaTiO 3”. In: *Journal of Materials Chemistry C* 10.1 (2022), pages 227–234 (cited on page 18).

[35] Antonio Feteira. “Negative temperature coefficient resistance (NTCR) ceramic thermistors: an industrial perspective”. In: *Journal of the American Ceramic Society* 92.5 (2009), pages 967–983 (cited on page 18).

[36] Burcu Ertuğ. “The Fabrication of Porous Barium Titanate Ceramics via Pore-Forming Agents (PFAs) for Thermistor and Sensor Applications”. In: *Powder Metallurgy* 4.1 (2012), pages 73–98 (cited on page 18).

[37] Clive A Randall et al. “Intrinsic and extrinsic size effects in fine-grained morphotropic-phase-boundary lead zirconate titanate ceramics”. In: *Journal of the American Ceramic Society* 81.3 (1998), pages 677–688 (cited on page 18).

[38] Jürgen Rödel et al. “Perspective on the development of lead-free piezoceramics”. In: *Journal of the American Ceramic Society* 92.6 (2009), pages 1153–1177 (cited on page 18).

[39] Ji Zhang et al. “Bi0. 5Na0. 5TiO3: ZnO lead-free piezoelectric composites with deferred thermal depolarization”. In: *Applied Physics Letters* 106.23 (2015), page 232904 (cited on page 19).

[40] AG Khachaturyan. “Ferroelectric solid solutions with morphotropic boundary: Rotational instability of polarization, metastable coexistence of phases and nanodomain adaptive states”. In: *Philosophical Magazine* 90.1-4 (2010), pages 37–60 (cited on page 19).

[41] Chonghea Li et al. “Formability of abx3 (x= f, cl, br, i) halide perovskites”. In: *Acta Crystallographica Section B: Structural Science* 64.6 (2008), pages 702–707 (cited on page 19).

[42] T Mitsui and William Blackburn Westphal. “Dielectric and X-Ray Studies of Ca x Ba 1- x Ti O 3 and Ca x Sr 1- x Ti O 3”. In: *Physical Review* 124.5 (1961), page 1354 (cited on page 19).

[43] Yonggang Yao et al. “Large piezoelectricity and dielectric permittivity in BaTiO3-xBaSnO3 system: The role of phase coexisting”. In: *EPL (Europhysics Letters)* 98.2 (2012), page 27008 (cited on page 19).

[44] Abdel-Baset MA Ibrahim et al. “Morphotropic phase boundary in ferroelectric materials”. In: *Ferroelectrics-Physical Effects* (2011) (cited on page 19).

[45] Muhtar Ahart et al. “Origin of morphotropic phase boundaries in ferroelectrics”. In: *Nature* 451.7178 (2008), pages 545–548 (cited on page 19).

[46] GA Rossetti Jr et al. “Ferroelectric solid solutions with morphotropic boundaries: Vanishing polarization anisotropy, adaptive, polar glass, and two-phase states”. In: *Journal of Applied Physics* 103.11 (2008), page 114113 (cited on page 19).

[47] Xiaobing Ren. “Large electric-field-induced strain in ferroelectric crystals by point-defect-mediated reversible domain switching”. In: *Nature materials* 3.2 (2004), pages 91–94 (cited on pages 19, 43, 60, 61, 63, 65).

[48] Jonathon N Baker et al. “Mechanisms governing metal vacancy formation in BaTiO3 and SrTiO3”. In: *Journal of Applied Physics* 124.11 (2018), page 114101 (cited on page 19).

[49] Pankaj P Khirade et al. “Multiferroic iron doped BaTiO3 nanoceramics synthesized by sol-gel auto combustion: influence of iron on physical properties”. In: *Ceramics International* 42.10 (2016), pages 12441–12451 (cited on page 19).

[50] Robert D Shannon. “Revised effective ionic radii and systematic studies of interatomic distances in halides and chalcogenides”. In: *Acta crystallographica section A: crystal physics, diffraction, theoretical and general crystallography* 32.5 (1976), pages 751–767 (cited on page 20).

[51] MI Morozov and D Damjanovic. “Charge migration in Pb (Zr, Ti) O 3 ceramics and its relation to ageing, hardening, and softening”. In: *Journal of Applied Physics* 107.3 (2010), page 034106 (cited on pages 19, 45, 65).

[52] Robert Gerson. “Variation in ferroelectric characteristics of lead zirconate titanate ceramics due to minor chemical modifications”. In: *Journal of Applied Physics* 31.1 (1960), pages 188–194 (cited on page 19).

[53] Lucien Eyraud et al. “Interpretation of the softening effect in PZT ceramics near the morphotropic phase boundary”. In: *Ferroelectrics* 330.1 (2006), pages 51–60 (cited on pages 19, 45).

[54] J Daniels et al. “ELECTRICAL CONDUCTIVITY AT HIGH TEMPERATURES OF DONOR-DOPED BARIUM TITANATE CERAMICS. I.” In: (1976) (cited on page 19).

[55] Ting Zheng et al. “Recent development in lead-free perovskite piezoelectric bulk materials”. In: *Progress in materials science* 98 (2018), pages 552–624 (cited on page 19).

[56] Hans Jaffe. “Piezoelectric ceramics”. In: *Journal of the American Ceramic Society* 41.11 (1958), pages 494–498 (cited on page 19).

[57] Jia Liu et al. “Charge effects in donor-doped perovskite ferroelectrics”. In: *Journal of the American Ceramic Society* 103.9 (2020), pages 5392–5399 (cited on page 19).

[58] M Ganguly et al. “Characterization and rietveld refinement of A-site deficient lanthanum doped barium titanate”. In: *Journal of alloys and compounds* 579 (2013), pages 473–484 (cited on pages 19, 41).

[59] Colin L Freeman et al. “Energetics of Donor-Doping, Metal Vacancies, and Oxygen-Loss in A-Site Rare-Earth-Doped BaTiO3”. In: *Advanced Functional Materials* 23.31 (2013), pages 3925–3928 (cited on pages 19, 41).

[60] Chen Ang et al. “Piezoelectric and electrostrictive strain behavior of Ce-doped BaTiO 3 ceramics”. In: *Applied physics letters* 80.18 (2002), pages 3424–3426 (cited on pages 19, 43, 65).

[61] Rüdiger-A Eichel. “Defect structure of oxide ferroelectrics—valence state, site of incorporation, mechanisms of charge compensation and internal bias fields”. In: *Journal of electroceramics* 19.1 (2007), pages 11–23 (cited on pages 20, 35, 45, 47, 53, 66).

[62] Lixue Zhang and Xiaobing Ren. “Aging behavior in single-domain Mn-doped BaTiO 3 crystals: implication for a unified microscopic explanation of ferroelectric aging”. In: *Physical Review B* 73.9 (2006), page 094121 (cited on pages 20, 41).

[63] NV Dang et al. “Structural, optical and magnetic properties of polycrystalline BaTi1-xFexO3 ceramics”. In: *Journal of Applied Physics* 110.4 (2011), page 043914 (cited on pages 20, 29, 46).

[64] Tao Li et al. “The effect of CuO doping on the microstructures and dielectric properties of BaTiO 3 ceramics”. In: *Journal of Materials Science: Materials in Electronics* 22.7 (2011), pages 838–842 (cited on page 20).

[65] DM Smyth. “Barium titanate”. In: *The Defect Chemistry of Metal Oxides* (2000), pages 253–282 (cited on page 20).

[66] LX Zhang and X Ren. “In situ observation of reversible domain switching in aged Mn-doped BaTiO 3 single crystals”. In: *Physical Review B* 71.17 (2005), page 174108 (cited on pages 20, 42, 43, 46, 52).

[67] G Arlt and H Neumann. “Internal bias in ferroelectric ceramics: origin and time dependence”. In: *Ferroelectrics* 87.1 (1988), pages 109–120 (cited on pages 20, 42, 52).

[68] Xiaobing Ren. “Giant electric-field induced strain in ferroelectric crystals by point-defect mediated reversible domain switching”. In: *APS March Meeting Abstracts*. Volume 2004. 2004, W19–005 (cited on pages 20, 46, 53, 67, 72).

[69] Xiaobing Ren and Kazuhiro Otsuka. “Universal symmetry property of point defects in crystals”. In: *Physical review letters* 85.5 (2000), page 1016 (cited on pages 20, 46, 53, 67, 72).

[70] PV Lambeck and GH Jonker. “The nature of domain stabilization in ferroelectric perovskites”. In: *Journal of Physics and Chemistry of Solids* 47.5 (1986), pages 453–461 (cited on pages 20, 53).

[71] Yuri A Genenko et al. “Mechanisms of aging and fatigue in ferroelectrics”. In: *Materials Science and Engineering: B* 192 (2015), pages 52–82 (cited on page 20).

[72] HL Stadler. “Etched hillocks in BaTiO3”. In: *Journal of Applied Physics* 34.3 (1963), pages 570–573 (cited on page 20).

[73] Sergey Ivanov. “Multiferroic complex metal oxides: main features of preparation, structure, and properties”. In: *Science and Technology of Atomic, Molecular, Condensed Matter & Biological Systems*. Volume 2. Elsevier, 2012, pages 163–238 (cited on page 23).

[74] CP Romao et al. “Negative thermal expansion (thermomiotic) materials”. In: (2013) (cited on page 23).

[75] JC Fothergill. “Estimating the cumulative probability of failure data points to be plotted on Weibull and other probability paper”. In: *IEEE transactions on Electrical Insulation* 25.3 (1990), pages 489–492 (cited on page 28).

[76] Qibin Yuan et al. “Relaxor ferroelectric 0.9 BaTiO 3–0.1 Bi (Zn 0.5 Zr 0.5) O 3 ceramic capacitors with high energy density and temperature stable energy storage properties”. In: *Journal of Materials Chemistry C* 5.37 (2017), pages 9552–9558 (cited on page 28).

[77] Bill Bergman. “On the estimation of the Weibull modulus”. In: *Journal of Materials Science Letters* 3.8 (1984), pages 689–692 (cited on pages 28, 29).

[78] IEC TC 112. “BSI Standards Publication Electric strength of insulating materials — Test methods Part 1 : Tests at power frequencies”. In: *Bsi* (2013), page 30 (cited on page 28).

[79] Baibo Liu et al. “Grain size effect and microstructure influence on the energy storage properties of fine-grained BaTiO3-based ceramics”. In: *Journal of the American Ceramic Society* 100.8 (2017), pages 3599–3607 (cited on page 30).

[80] T Tunkasiri and G Rujijanagul. “Dielectric strength of fine grained barium titanate ceramics”. In: *Journal of materials science letters* 15.20 (1996), pages 1767–1769 (cited on page 30).

[81] Hee Young Lee, Kyung Ho Cho, and Hyo-Duk Nam. “Grain size and temperature dependence of electrical breakdown in BaTiO3 ceramic”. In: *Ferroelectrics* 334.1 (2006), pages 165–169 (cited on page 30).

[82] A Young et al. “Effect of liquid-phase sintering on the breakdown strength of barium titanate”. In: *Journal of the American Ceramic Society* 90.5 (2007), pages 1504–1510 (cited on page 30).

[83] FK Lotgering. “Topotactical reactions with ferrimagnetic oxides having hexagonal crystal structures—I”. In: *Journal of Inorganic and Nuclear Chemistry* 9.2 (1959), pages 113–123 (cited on page 29).

[84] Emil Zolotoyabko. “Determination of the degree of preferred orientation within the March–Dollase approach”. In: *Journal of applied Crystallography* 42.3 (2009), pages 513–518 (cited on page 29).

[85] Alan Hewat, WI David, and L van Eijck. “Hugo Rietveld (1932–2016)”. In: *Journal of Applied Crystallography* 49.4 (2016), pages 1394–1395 (cited on page 32).

[86] Hugo M Rietveld. “A profile refinement method for nuclear and magnetic structures”. In: *Journal of applied Crystallography* 2.2 (1969), pages 65–71 (cited on page 32).

[87] IA Lira-Hernández et al. “Comments about Rietveld Analysis and Tolerance Factor: Y Doped BaTiO3”. In: (2016) (cited on page 33).

[88] Brian H Toby. “R factors in Rietveld analysis: How good is good enough?” In: *Powder diffraction* 21.1 (2006), pages 67–70 (cited on page 33).

[89] Nam-Kyeong Kim et al. “Crystallographic Orientation Dependent Ferroelectric Characteristics of (Bi3. 3, La0. 8) Ti3O12 (BLT) Capacitors”. In: *Integrated Ferroelectrics* 70.1 (2005), pages 89–97 (cited on page 34).

[90] J-H Park et al. “Effects of preferred orientation on the piezoelectric properties of Pt/Pb (Zr0. 3Ti0. 7) O3/Pt thin films grown by sol–gel process”. In: *Journal of Materials Science: Materials in Electronics* 20.4 (2009), pages 366–373 (cited on page 34).

[91] Woo Sik Kim, Jun-Kyu Yang, and Hyung-Ho Park. “Influence of preferred orientation of lead zirconate titanate thin film on the ferroelectric properties”. In: *Applied surface science* 169 (2001), pages 549–552 (cited on page 34).

[92] Hans Theo Langhammer et al. “Crystal structure and related properties of copper-doped barium titanate ceramics”. In: *Solid State Sciences* 5.7 (2003), pages 965–971 (cited on page 35).

[93] Fabio La Mattina et al. “Controlled oxygen vacancies and space correlation with Cr 3+ in SrTiO 3”. In: *Physical Review B* 80.7 (2009), page 075122 (cited on pages 35, 36).

[94] Evgeny Blokhin et al. “Theoretical modeling of the complexes of iron impurities and oxygen vacancies in SrTiO3”. In: *Applied Physics Letters* 102.11 (2013), page 112913 (cited on pages 35, 36).

[95] ES Kirkpatrick, KA Müller, and RS Rubins. “Strong Axial Electron Paramagnetic Resonance Spectrum of Fe 3+ in SrTi O 3 Due to Nearest-Neighbor Charge Compensation”. In: *Physical Review* 135.1A (1964), A86 (cited on pages 35, 36).

[96] R Böttcher et al. “3C–6H phase transition in BaTiO3 induced by Fe ions: an electron paramagnetic resonance study”. In: *Journal of Physics: Condensed Matter* 20.50 (2008), page 505209 (cited on page 36).

[97] Da-Yong Lu, Xiu-Yun Sun, and Masayuki Toda. “A novel high-k ‘Y5V’barium titanate ceramics co-doped with lanthanum and cerium”. In: *Journal of Physics and Chemistry of Solids* 68.4 (2007), pages 650–664 (cited on pages 36, 37).

[98] E Siegel and KA Müller. “Local position of Fe 3+ in ferroelectric BaTi O 3”. In: *Physical Review B* 20.9 (1979), page 3587 (cited on page 37).

[99] Hiroshi Kishi et al. “Study of occupational sites and dielectric properties of Ho–Mg and Ho–Mn substituted BaTiO3”. In: *Japanese Journal of Applied Physics* 39.9S (2000), page 5533 (cited on page 37).

[100] Timothy D Dunbar et al. “Electron paramagnetic resonance investigations of lanthanide-doped barium titanate: dopant site occupancy”. In: *The Journal of Physical Chemistry B* 108.3 (2004), pages 908–917 (cited on page 37).

[101] H-J Hagemann. “Loss mechanisms and domain stabilisation in doped BaTiO3”. In: *Journal of Physics C: Solid State Physics* 11.15 (1978), page 3333 (cited on pages 41, 45).

[102] Kang Yan et al. “Ferroelectric aging effects and large recoverable electrostrain in ceria-doped BaTiO3 ceramics”. In: *Journal of the American Ceramic Society* 102.5 (2019), pages 2611–2618 (cited on page 41).

[103] Jan Petzelt. “Dielectric grain-size effect in high-permittivity ceramics”. In: *Ferroelectrics* 400.1 (2010), pages 117–134 (cited on page 41).

[104] Yongqiang Tan et al. “Unfolding grain size effects in barium titanate ferroelectric ceramics”. In: *Scientific reports* 5.1 (2015), pages 1–9 (cited on page 41).

[105] A Salhi et al. “Impedance spectroscopy analysis of Ca doped BaTiO3 ferroelectric ceramic manufactured with a new synthesis technique”. In: *Materials Today: Proceedings* 13 (2019), pages 1248–1258 (cited on page 41).

[106] JN Lin and TB Wu. “Effects of isovalent substitutions on lattice softening and transition character of BaTiO3 solid solutions”. In: *Journal of applied physics* 68.3 (1990), pages 985–993 (cited on page 41).

[107] Sabina Yasmm et al. “Effect of cerium doping on microstructure and dielectric properties of BaTiO3 ceramics”. In: *Journal of Materials Science & Technology* 27.8 (2011), pages 759–763 (cited on page 41).

[108] Wei-Gang Yang et al. “High piezoelectric properties of BaTiO3–xLiF ceramics sintered at low temperatures”. In: *Journal of the European Ceramic Society* 32.4 (2012), pages 899–904 (cited on page 42).

[109] Wei Chen et al. “Effect of the Mn doping concentration on the dielectric and ferroelectric properties of different-routes-fabricated BaTiO3-based ceramics”. In: *Journal of Alloys and Compounds* 670 (2016), pages 48–54 (cited on page 42).

[110] Yingying Zhao et al. “Aging rate of cerium doped Ba (Ti0. 99Mn0. 01) O3”. In: *Ceramics International* 43 (2017), S70–S74 (cited on page 42).

[111] RC Bradt and GS Ansell. “Aging in tetragonal ferroelectric barium titanate”. In: *Journal of the American Ceramic Society* 52.4 (1969), pages 192–198 (cited on pages 42, 60).

[112] Thomas R Shrout and Shujun J Zhang. “Lead-free Piezoelectric Ceramics: Alternatives for PZT?” In: *Progress in Advanced Dielectrics*. World Scientific, 2020, pages 295–327 (cited on page 43).

[113] EI Bondarenko, V Yu Topolov, and AV Turik. “The role of 90 domain wall displacements in forming physical properties of perovskite ferroelectric ceramics”. In: *Ferroelectrics Letters Section* 13.1 (1991), pages 13–19 (cited on page 43).

[114] Dragan Damjanovic and Marlyse Demartin. “Contribution of the irreversible displacement of domain walls to the piezoelectric effect in barium titanate and lead zirconate titanate ceramics”. In: *Journal of Physics: Condensed Matter* 9.23 (1997), page 4943 (cited on page 43).

[115] Fei Li et al. “Electrostrictive effect in ferroelectrics: An alternative approach to improve piezoelectricity”. In: *Applied Physics Reviews* 1.1 (2014), page 011103 (cited on page 43).

[116] Takaaki Tsurumi et al. “90° domain reorientation and electric-field-induced strain of tetragonal lead zirconate titanate ceramics”. In: *Japanese journal of applied physics* 36.9S (1997), page 5970 (cited on page 43).

[117] Seung-Eek Park and Thomas R Shrout. “Ultrahigh strain and piezoelectric behavior in relaxor based ferroelectric single crystals”. In: *Journal of applied physics* 82.4 (1997), pages 1804–1811 (cited on page 43).

[118] CH Park and DJ Chadi. “Microscopic study of oxygen-vacancy defects in ferroelectric perovskites”. In: *Physical Review B* 57.22 (1998), R13961 (cited on pages 45, 47, 48, 65).

[119] Gurvinderjit Singh, VS Tiwari, and PK Gupta. “Role of oxygen vacancies on relaxation and conduction behavior of KNbO 3 ceramic”. In: *Journal of Applied Physics* 107.6 (2010), page 064103 (cited on pages 45, 47).

[120] Shi Liu and RE Cohen. “Multiscale simulations of defect dipole–enhanced electromechanical coupling at dilute defect concentrations”. In: *Applied Physics Letters* 111.8 (2017), page 082903 (cited on pages 45, 46).

[121] Lei Wang et al. “Enhanced strain effect of aged acceptor-doped BaTiO3 ceramics with clamping domain structures”. In: *Applied Physics Letters* 110.10 (2017), page 102904 (cited on pages 45, 46).

[122] Changhao Zhao et al. “Precipitation hardening in ferroelectric ceramics”. In: *Advanced Materials* 33.36 (2021), page 2102421 (cited on page 45).

[123] Masao Takahashi. “Space charge effect in lead zirconate titanate ceramics caused by the addition of impurities”. In: *Japanese Journal of Applied Physics* 9.10 (1970), page 1236 (cited on page 45).

[124] Sadayuki Takahashi. “Internal bias field effects in lead zirconate-titanate ceramics doped with multiple impurities”. In: *Japanese Journal of Applied Physics* 20.1 (1981), page 95 (cited on page 45).

[125] Methee Promsawat et al. “Electrical fatigue behavior of lead zirconate titanate ceramic under elevated temperatures”. In: *Journal of the European Ceramic Society* 37.5 (2017), pages 2047–2055 (cited on page 45).

[126] I-K Jeong et al. “Structural evolution across the insulator-metal transition in oxygen-deficient BaTiO 3- δ studied using neutron total scattering and Rietveld analysis”. In: *Physical Review B* 84.6 (2011), page 064125 (cited on page 47).

[127] JF Schooley, WR Hosler, and Marvin L Cohen. “Superconductivity in Semiconducting SrTi O 3”. In: *Physical Review Letters* 12.17 (1964), page 474 (cited on pages 47, 54).

[128] MK Paria and HS Maiti. “Electrical conduction in barium titanate”. In: *Journal of materials science letters* 3.7 (1984), pages 578–580 (cited on page 47).

[129] Chenjie Fu, Nan Chen, and Guoping Du. “Comparative studies of nickel doping effects at A and B sites of BaTiO3 ceramics on their crystal structures and dielectric and ferroelectric properties”. In: *Ceramics International* 43.17 (2017), pages 15927–15931 (cited on page 47).

[130] C Meric Guvenc and Umut Adem. “Influence of aging on electrocaloric effect in Li+ doped BaTiO3 ceramics”. In: *Journal of Alloys and Compounds* 791 (2019), pages 674–680 (cited on page 47).

[131] Soonil Lee and Clive A Randall. “Determination of electronic and ionic conductivity in mixed ionic conductors: HiTEC and in-situ impedance spectroscopy analysis of isovalent and aliovalent doped BaTiO3”. In: *Solid State Ionics* 249 (2013), pages 86–92 (cited on pages 47, 48).

[132] JMH Seuter. “Defect chemistry and electrical transport properties of barium titanate”. In: *Philips Res. Rep. Suppl.* (1974), pages 1–84 (cited on page 47).

[133] Yoed Tsur and Clive A Randall. “Point defect concentrations in barium titanate revisited”. In: *Journal of the American Ceramic Society* 84.9 (2001), pages 2147–2149 (cited on page 47).

[134] J Hwang et al. “Doping and temperature-dependent optical properties of oxygen-reduced BaTiO 3- δ”. In: *Physical Review B* 82.21 (2010), page 214109 (cited on page 47).

[135] Tian-Fu Zhang et al. “Oxygen-vacancy-related relaxation and conduction behavior in (Pb1-x Ba x)(Zr0. 95Ti0. 05) O3 ceramics”. In: *AIP Advances* 4.10 (2014), page 107141 (cited on page 47).

[136] Seok-Hyun Yoon et al. “Effect of acceptor (Mg) concentration on the electrical resistance at room and high (200° C) temperatures of acceptor (Mg)-doped Ba Ti O 3 ceramics”. In: *Journal of Applied Physics* 102.5 (2007), page 054105 (cited on page 47).

[137] Soonil Lee, William H Woodford, and Clive A Randall. “Crystal and defect chemistry influences on band gap trends in alkaline earth perovskites”. In: *Applied Physics Letters* 92.20 (2008), page 201909 (cited on page 47).

[138] Niall J Donnelly and Clive A Randall. “Pb loss in Pb (Zr, Ti) O3 ceramics observed by in situ ionic conductivity measurements”. In: *Journal of Applied Physics* 109.10 (2011), page 104107 (cited on page 48).

[139] MF Zhang et al. “Characterization of oxygen vacancies and their migration in Ba-doped Pb (Zr 0.52 Ti 0.48) O 3 ferroelectrics”. In: *Journal of Applied Physics* 105.6 (2009), page 061639 (cited on pages 48, 53).

[140] Youn-Kyu Choi et al. “Effect of oxygen vacancy and oxygen vacancy migration on dielectric response of BaTiO3-Based Ceramics”. In: *Japanese Journal of Applied Physics* 50.3R (2011), page 031504 (cited on pages 48, 53).

[141] Piotr Jasinski et al. “Impedance studies of diffusion phenomena and ionic and electronic conductivity of cerium oxide”. In: *Journal of the Electrochemical Society* 152.4 (2005), J27 (cited on page 48).

[142] M Legallais et al. “Fast re-oxidation kinetics and conduction pathway in Spark Plasma Sintered ferroelectric ceramics”. In: *Journal of the European Ceramic Society* 38.2 (2018), pages 543–550 (cited on page 48).

[143] José Alvarez et al. “Electrical characterization of Schottky diodes based on boron doped homoepitaxial diamond films by conducting probe atomic force microscopy”. In: *Superlattices and Microstructures* 40.4-6 (2006), pages 343–349 (cited on pages 49, 50).

[144] Aymeric Vecchiola et al. “Wide range local resistance imaging on fragile materials by conducting probe atomic force microscopy in intermittent contact mode”. In: *Applied Physics Letters* 108.24 (2016), page 243101 (cited on page 49).

[145] Jules Courtin et al. “A low Schottky barrier height and transport mechanism in gold–graphene–silicon (001) heterojunctions”. In: *Nanoscale Advances* 1.9 (2019), pages 3372–3378 (cited on page 49).

[146] Paul Narchi et al. “Cross-sectional investigations on epitaxial silicon solar cells by kelvin and conducting probe atomic force microscopy: effect of illumination”. In: *Nanoscale research letters* 11.1 (2016), pages 1–8 (cited on page 49).

[147] Roger A De Souza. “Limits to the rate of oxygen transport in mixed-conducting oxides”. In: *Journal of Materials Chemistry A* 5.38 (2017), pages 20334–20350 (cited on page 53).

[148] William L Warren et al. “Oxygen vacancy motion in perovskite oxides”. In: *Journal of the American Ceramic Society* 79.2 (1996), pages 536–538 (cited on pages 53, 57).

[149] Yuji Noguchi et al. “Ferroelectrics with a controlled oxygen-vacancy distribution by design”. In: *Scientific reports* 9.1 (2019), pages 1–10 (cited on page 53).

[150] MV Raymond and DM Smyth. “Defects and charge transport in perovskite ferroelectrics”. In: *Journal of Physics and Chemistry of Solids* 57.10 (1996), pages 1507–1511 (cited on page 54).

[151] KnW Plessner. “Ageing of the dielectric properties of barium titanate ceramics”. In: *Proceedings of the Physical Society. Section B* 69.12 (1956), page 1261 (cited on page 57).

[152] AF Devonshire. “Theory of ferroelectrics”. In: *Advances in physics* 3.10 (1954), pages 85–130 (cited on page 57).

[153] WL Warren et al. “Alignment of defect dipoles in polycrystalline ferroelectrics”. In: *Applied physics letters* 67.12 (1995), pages 1689–1691 (cited on page 57).

[154] WL Warren et al. “Defect-dipole alignment and tetragonal strain in ferroelectrics”. In: *Journal of applied physics* 79.12 (1996), pages 9250–9257 (cited on page 57).

[155] D Scott Mackenzie. “History of quenching”. In: *International Heat Treatment and Surface Engineering* 2.2 (2008), pages 68–73 (cited on page 58).

[156] JF Scott and Matthew Dawber. “Oxygen-vacancy ordering as a fatigue mechanism in perovskite ferroelectrics”. In: *Applied Physics Letters* 76.25 (2000), pages 3801–3803 (cited on page 59).

[157] Maxim I Morozov and Dragan Damjanovic. “Hardening-softening transition in Fe-doped Pb (Zr, Ti) O 3 ceramics and evolution of the third harmonic of the polarization response”. In: *Journal of Applied Physics* 104.3 (2008), page 034107 (cited on page 59).

[158] LX Zhang, W Chen, and X Ren. “Large recoverable electrostrain in Mn-doped (Ba, Sr) Ti O 3 ceramics”. In: *Applied Physics Letters* 85.23 (2004), pages 5658–5660 (cited on page 59).

[159] Julia Glaum et al. “Temperature and driving field dependence of fatigue processes in PZT bulk ceramics”. In: *Acta materialia* 59.15 (2011), pages 6083–6092 (cited on pages 59, 70).

[160] Nina Balke et al. “Fatigue of lead zirconate titanate ceramics. I: Unipolar and DC loading”. In: *Journal of the American Ceramic Society* 90.4 (2007), pages 1081–1087 (cited on page 59).

[161] U Robels and G Arlt. “Domain wall clamping in ferroelectrics by orientation of defects”. In: *Journal of Applied Physics* 73.7 (1993), pages 3454–3460 (cited on page 60).

[162] Doru C Lupascu, Yuri A Genenko, and Nina Balke. “Aging in ferroelectrics”. In: *Journal of the American Ceramic Society* 89.1 (2006), pages 224–229 (cited on page 60).

[163] Bin Xu et al. “Pinched hysteresis loop in defect-free ferroelectric materials”. In: *Physical Review B* 94.14 (2016), page 140101 (cited on page 65).

[164] Charles Paillard et al. “Vacancies and holes in bulk and at 180° domain walls in lead titanate”. In: *Journal of Physics: Condensed Matter* 29.48 (2017), page 485707 (cited on page 66).

[165] Anand Chandrasekaran et al. “Defect ordering and defect–domain-wall interactions in PbTiO 3: A first-principles study”. In: *Physical Review B* 88.21 (2013), page 214116 (cited on page 66).

[166] Lixin He and David Vanderbilt. “First-principles study of oxygen-vacancy pinning of domain walls in PbTiO 3”. In: *Physical Review B* 68.13 (2003), page 134103 (cited on page 66).

[167] Shogo Tomoda et al. “Hybrid functional study on the ferroelectricity of domain walls with O-vacancies in PbTiO3”. In: *Mechanical Engineering Journal* 2.3 (2015), pages 15–00037 (cited on page 66).

[168] Henry Eyring. “The activated complex in chemical reactions”. In: *The Journal of Chemical Physics* 3.2 (1935), pages 107–115 (cited on page 67).

[169] Peter Hänggi, Peter Talkner, and Michal Borkovec. “Reaction-rate theory: fifty years after Kramers”. In: *Reviews of modern physics* 62.2 (1990), page 251 (cited on page 67).

[170] Pavel Goudochnikov and Andrew J Bell. “Correlations between transition temperature, tolerance factor and cohesive energy in 2+: 4+ perovskites”. In: *Journal of Physics: Condensed Matter* 19.17 (2007), page 176201 (cited on page 67).

[171] W Münch et al. “The relation between crystal structure and the formation and mobility of protonic charge carriers in perovskite-type oxides: A case study of Y-doped BaCeO3 and SrCeO3”. In: *Phase Transitions* 68.3 (1999), pages 567–586 (cited on page 67).

[172] Truls Norby and Yngve Larring. “Concentration and transport of protons in oxides”. In: *Current Opinion in Solid State and Materials Science* 2.5 (1997), pages 593–599 (cited on page 67).

[173] Julius Koettgen et al. “Ab initio calculation of the attempt frequency of oxygen diffusion in pure and samarium doped ceria”. In: *Physical Chemistry Chemical Physics* 19.15 (2017), pages 9957–9973 (cited on page 67).

[174] Arif Ismail et al. “A DFT+ U study of defect association and oxygen migration in samarium-doped ceria”. In: *Physical Chemistry Chemical Physics* 13.13 (2011), pages 6116–6124 (cited on page 67).

[175] Vladimir Koval, Giuseppe Viola, and Yongqiang Tan. “Biasing effects in ferroic materials”. In: *Ferroelectric Materials–Synthesis and Characterization* (2015) (cited on pages 68, 70).

[176] U Robels, JH Calderwood, and G Arlt. “Shift and deformation of the hysteresis curve of ferroelectrics by defects: An electrostatic model”. In: *Journal of applied physics* 77.8 (1995), pages 4002–4008 (cited on page 70).

[177] Julia Glaum, Torsten Granzow, and Jürgen Rödel. “Evaluation of domain wall motion in bipolar fatigued lead-zirconate-titanate: A study on reversible and irreversible contributions”. In: *Journal of Applied Physics* 107.10 (2010), page 104119 (cited on page 70).

A. Publications

Journal of the European Ceramic Society xxx (xxxx) xxx

Contents lists available at ScienceDirect

Journal of the European Ceramic Society

journal homepage: www.elsevier.com/locate/jeurceramsoc

Review article

Enhancing properties of lead-free ferroelectric $BaTiO_3$ through doping

Zechao Li [a], Jiacheng Yu [a], Shenglan Hao [a], Pierre-Eymeric Janolin [a,*]

[a] Unversité Paris-Saclay, CNRS, CentraleSupélec, laboratoire SPMS, 91190 Gif-sur-Yvette, France

ARTICLE INFO

Keywords:
Ceramics
Ferroelectrics
Microstructure
Properties

ABSTRACT

The substitution on either the *A*- or *B*-site of ferroelectric perovskites by aliovalent elements has a profound influence on their properties. Donor doping "softens" ferroelectrics, whereas acceptor doping "hardens" them. The charge compensation mechanisms are reviewed, as well as the models describing their effects. The focus of this review is doped-$BaTiO_3$, a model lead-free ferroelectric. The effects of aliovalent doping on its dielectric, ferroelectric, and piezoelectric properties are reviewed and illustrated in the case of Cu (acceptor) doping.

1. Introduction

Ferroelectric materials are characterised by a spontaneous polarisation (P_s) that can be switched reversibly between at least two different orientations under the application of an electric field [1–4]. Since the first ferroelectric crystals were produced in 1935 by Bush and Scherrer[1], ferroelectric materials have attracted much attention from a wide community due to their numerous properties including dielectric, piezoelectric, pyroelectric, electrocaloric etc. As a consequence, ferroelectric materials are used not only in the fields of information memory, energy storage, and optical devices but also as resonators, transducers, sensors, actuators, and capacitors [2,5–8]. New ferroelectric materials were gradually discovered and synthesized to satisfy various application needs, such as lead zirconate titanate ($PbZr_{1-x}Ti_xO_3$), lead lanthanum zirconate titanate ($Pb_{1-3y}La_{2y}Zr_{1-x}Ti_xO_3$ or $Pb_{1-y}La_y(Zr_{1-x}Ti_x)_{1-0.25y}O_3$), and barium titanate ($BaTiO_3$).

$BaTiO_3$ is a promising candidate for lead-free perovskite oxide (ABO_3) ferroelectrics. The Ba^{2+} cation occupies the *A* site at the corners of the perovskite unit cell and each *A*-site cation is 12-fold coordinated with the oxygen anions. At the center of the cell (on the *B* site), the Ti^{4+} is surrounded by an oxygen octahedron (6-fold coordination). Doping on either the *A* site [9–11], *B* site [12–14] or both [15,16] to tune $BaTiO_3$ properties has been extensively investigated. Indeed, adding suitable dopants to $BaTiO_3$, even in minute quantity, has a dramatic influence on its electrical properties. For example, M. Acosta *et al.* reviewed the improved piezoelectric properties of doped $BaTiO_3$ [17], and dielectric properties of rare-earth doped $BaTiO_3$ were summarized by F. Ismail *et al.* [18] Recently, S. Hao *et al.* investigated the change in optical absorption of co-doped $BaTiO_3$ ceramics [19].

Here, we shall review the effects of doping on $BaTiO_3$ ceramics in terms of dielectric, ferroelectric, and piezoelectric properties. Moreover, various ferroelectric behaviors of acceptor-doped $BaTiO_3$ will be systematically illustrated with Cu-doped $BaTiO_3$.

First, $BaTiO_3$-based solid solutions should be distinguished from *M*-doped $BaTiO_3$ based on whether the *M*-based compound can adopt the perovskite structure. If $MTiO_3$ (e.g. $SrTiO_3$) or $BaMO_3$ (e.g. $BaZrO_3$) form a stable perovskite then a solid-solution is usually formed. This is generally the case with isovalent substitution on either the *A* or *B* site of the perovskite and can be predicted based on the Goldschmidt tolerance factor and the octahedral factor [20]. On the contrary, if $MTiO_3$ or $BaMO_3$ do not form a stable perovskite phase, then there is a maximum amount of *M* that can be introduced in the perovskite structure of $BaTiO_3$ (usually a few atomic percents). The resulting compounds constitute the *M*-doped $BaTiO_3$ that are the topic of this review.

Substitutional aliovalent (a.k.a heterovalent) doping is the intentional introduction of dopants with a different valence than the ion for which they substitute in the base material. Common dopants for $BaTiO_3$ and their valence are shown by green stars (*A*-site doping) and blue circles (*B*-site doping) in Fig. 1. Aliovalent dopants can be more or less positively charged than the host ion, therefore defining respectively donors or acceptors.

Doping ferroelectrics with donors (e.g. Rare-Earth ions RE^{3+} substituting for Ba^{2+}) "softens" them. The "soft" ferroelectrics are characterized by a higher mobility of their domain walls. This is ascribed to the following two mechanisms: the relieved internal stress caused by Ba or Ti vacancies (V''_{Ba} or V''''_{Ti}) [22–24] and electrons transfer between ionized Ba and Ti vacancies [23,25,26]. The relative importance of each mechanism remains to be determined. In addition, the primary charge

* Corresponding author.
E-mail address: Pierre-Eymeric.Janolin@centralesupelec.fr (P.-E. Janolin).

https://doi.org/10.1016/j.jeurceramsoc.2022.05.023
Received 16 February 2022; Received in revised form 10 May 2022; Accepted 11 May 2022
Available online 16 May 2022

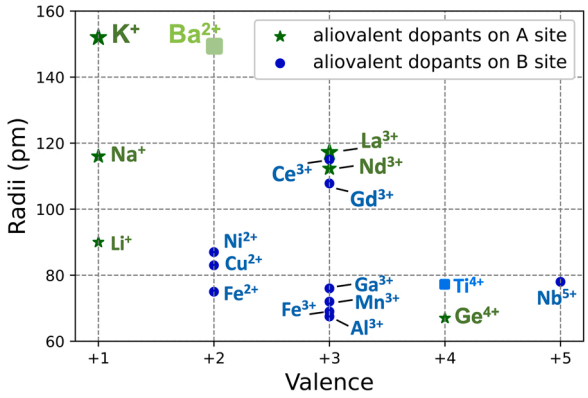

Fig. 1. The radii [21] of common dopants for $BaTiO_3$. The host ions (Ba^{2+} and Ti^{4+}) are presented by square symbols and the aliovalent dopants for *A* site (coordination 12) and *B* site (coordination 6) of $BaTiO_3$ are shown by green stars and blue circles respectively.

compensation mechanism in donor-doped ferroelectrics (Ba vacancies, Ti vacancies, free electrons, changes of valence state of Ti ions.) [9,10,27] remains as well an open question [28].

Oppositely, acceptor doping hinders the movement of the domain walls. Ferroelectrics consequently become "hard" [3]. The two main models put forward to explain this are the volume and surface effects.

The volume effect attributes the stabilization of the domain structure to the oxygen vacancies [29], accompanying acceptor doping through the formation of defect dipoles ($M-$ Vö), as shown by EPR measurements on Mn^{2+} [30]. These dipoles act as an internal bias field that pins the domains and therefore stiffens the walls [14,31,32]. According to the symmetry-conforming principle of point defects, the symmetry of defect dipoles conform to the surrounding crystal symmetry at thermodynamic equilibrium [33,34]. With oxygen vacancies hopping between neighboring positions next to dopants, defect dipoles achieve reorientation [35,36]. The surface effect postulates that the oxygen vacancies move to the domain walls or grain boundaries where they fix the domain walls [31,37,38]. The aging observed in Mn-doped $BaTiO_3$ single-domain crystal [39] (devoid of domain walls) or with controlled domain structures [35] strongly supports the volume effect as the main hardening mechanism in ferroelectrics. To illustrate the volume effect at play and the interactions between the defect dipoles and the spontaneous polarisation of the crystal matrix, Cu was chosen as a dopant for its stable vacancy especially in octahedral symmetry. Substituting for Ti, it is therefore an acceptor and will harden $BaTiO_3$.

2. Changing dielectric properties

2.1. Effect on the permittivity

In ferroelectrics, the domain walls motion is a major contributor to the dielectric properties. The dielectric response is significantly improved by enhancing the 180° domain wall (Fig. 2(a)) mobility in tetragonal $BaTiO_3$ without introducing large dielectric losses, which are mostly caused by 90° domain wall (Fig. 2(b)) motion [40] and electronic conduction [10].

When $BaTiO_3$ is doped with donors, *A*-site vacancies [9,41], *B*-site vacancies [42,43], and/or electrons [43] are induced for charge balancing. This is the case for example when La^{3+} substitutes for Ba^{2+}: $3\,Ba_{Ba}^{\times} \rightarrow V_{Ba}'' + 2\,La_{Ba}^{\cdot}$ in $Ba_{1-3x}La_{2x}TiO_3$, $Ba_{Ba}^{\times} + \frac{1}{4}Ti_{Ti}^{\times} \rightarrow La_{Ba}^{\cdot} + \frac{1}{4}V_{Ti}''''$ in $Ba_{1-y}La_yTi_{1-y/4}O_3$, and $Ba_{Ba}^{\times} \rightarrow La_{Ba}^{\cdot} + e^-$ in $Ba_{1-z}La_zTiO_3$ [9]. Due to the softening mechanism of donor doping, the permittivity increases [3,44,45]. For example, the relative permittivity reaches 11800 for *A*-site Nd^{3+}-doped $BaTiO_3$ [41] and 36000 for *A*-site La^{3+}-Zr^{4+} co-doped $BaTiO_3$ [46] compared with to 4500–10000 in pure $BaTiO_3$ [47,48]. In addition, the induced electrons from donor doping increase the conduction, resulting in an increase of dielectric losses [10,11].

In acceptor-doped $BaTiO_3$, positively charged oxygen vacancies are induced for charge compensation [36,39,49,50], such as $3\,Ti_{Ti}^{x} \rightarrow 2\,Ti^{3+} + Ni_{Ti}'' + 2\,Vö$ in $BaTi_{1-x}Ni_xO_3$ [16], and $Ba_{Ba}^{\times} \rightarrow LiBa' + ½\,Vö$ in $Ba_{1-x}Li_{2x}TiO_3$ [51]. The existence of oxygen vacancies decreases the mobility of domain walls, contributing to the decrease of the permittivity [39]. For example, with Fe or Mn concentrations increasing to 1 at %, the permittivity of *B*-site-doped $BaTiO_3$ decreases to 1800 or 1000, respectively [52]; Ce^{3+}-Gd^{3+} co-doped $BaTiO_3$ (on the *B* site) also exhibits a decreased permittivity as the doping concentration increases [53]. This is also the case for the incorporation (still on the *B*-site) of Zn^{2+} in $BaTiO_3$ that decreases the permittivity value by almost 1000 [54]. Even though it is not the case for $BaTiO_3$ doped with 0.4 at%Cu, permittivity decreases with Cu concentrations increasing to 1.6 at% (Fig. 4(a)). Moreover, oxygen vacancies may also contribute to the conductivity, thereby increasing dielectric losses [55]. For example, the oxygen-deficient $BaTiO_{3-\delta}$ eventually crosses an insulator-metal transition when δ exceeds 0.25, while retaining its ferroelectric character [56]. In our work, 1.6 at%Cu(acceptor)-doped $BaTiO_3$ shows higher

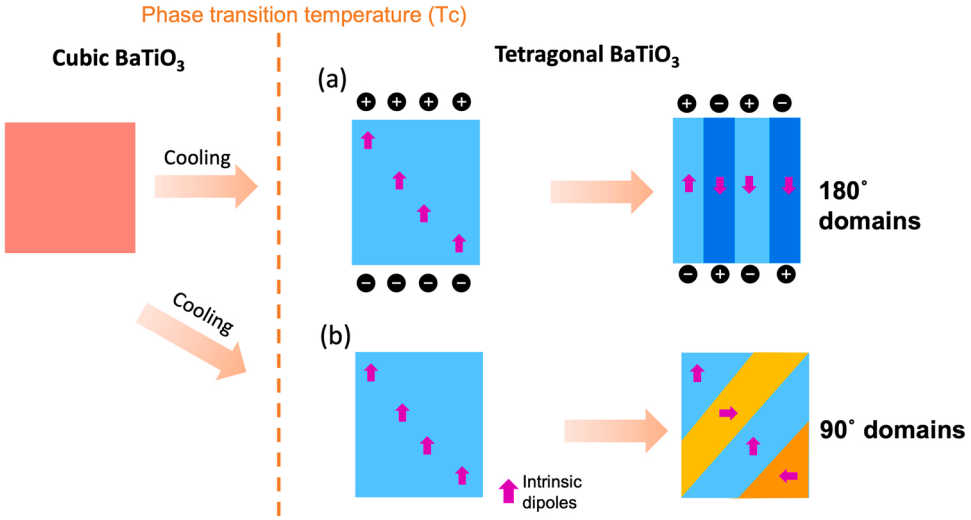

Fig. 2. Schematic of the formation of 180° (a) and 90° (b) domain walls in $BaTiO_3$. Cooling below the phase transition temperature, the spontaneous polarisation of $BaTiO_3$ induces surface charges which cause a depolarizing field. As a result, 180°-domains with opposite polarisation are created in order to minimize the corresponding electrostatic energy; (b) Simultaneously, 90° domains are created to minimize the mechanical stresses caused by the phase transition.

dielectric loss than undoped sample, as shown in Fig. 4(b).

2.2. Shifting phase transitions

In addition to affecting the permittivity of $BaTiO_3$, doping can also change the transition temperatures. At high temperature (above the Curie temperature T_C), $BaTiO_3$ is paraelectric with a centrosymmetric cubic symmetry ($Pm\,\bar{3}\,m$). It undergoes a series of phase transitions to ferroelectric phases: first to a tetragonal ($P4mm$) at T_C= 395 K, then to an orthorhombic (Amm) phase at $T_{T\text{-}O}$= 280 K and finally to a rhombohedral ($R3m$) phase at 185 K[1,3] (see Fig. 3).

The phase transitions of $BaTiO_3$ are mostly displacive and have been interpreted by the displacement of Ti cations relative to O_6 cage. Precisely, the direction of this displacement is determined by the competition between short-range interactions (Pauli repulsion) and long-range interactions (Coulomb attraction, dipole-dipole) [22,57].

Because dopants have an ionic radius that differs from the one of the host ions, the oxygen octahedron surrounding a dopant is distorted and changes in phase transition temperatures are therefore expected. When smaller ions substitute for Ba^{2+} on the A site ($r_{Ba^{2+}}$=149 pm), the surrounding oxygen ions displace towards the dopant, resulting in a more open space enabling the larger displacement of Ti. Such displacement is favored along the ⟨111⟩ axes rather than along the ⟨100⟩ axis [58].

As a consequence the tetragonal phase is destabilized and T_C decreases. For example, the T_C of Ce-doped $BaTiO_3$ ($r_{Ce^{3+}}$=115 pm) decreases to 313 K for a Ce concentration of 3 at% [59]. The other phase transition temperatures may also be affected. In A-site La-doped $BaTiO_3$ ($Ba_{1-x}La_{2x/3}TiO_3$ with $r_{La^{3+}}$ = 117.2 pm) T_C decreases while $T_{T\text{-}O}$ increases with increasing La concentration until x = 0.06, resulting in an overall narrower temperature range for the tetragonal phase [27].

Besides the effects on the A-site, replacing Ti ions ($r_{Ti^{4+}}$=74.5 pm) on the B site by dopants with different radii also distorts oxygen octahedra. A destabilization of the tetragonal phase occurs when larger ions substitute for Ti. These larger ions push the adjacent oxygen anions toward the neighboring octahedra, reducing the space for the displacement of Ti ions along ⟨ 100 ⟩ axis. Consequently, the cubic-tetragonal transition (at T_C) is shifted to lower temperatures. The tetragonal-orthogonal phase transition (at T_{O-T}) may also be changed [58] For example, the T_C and T_{O-T} of (1-x)$BaTiO_3$ − xLiF ceramics (r_{Li^+}=90 pm) are decreased to 334 K and increased to 298 K respectively with increasing x (over the 2–5 at % range).[60].

Adding 1 wt% of Zn ($r_{Zn^{2+}}$=88 pm) lowers the Curie temperature of $BaTiO_3$ by 7 K [54]. In $BaTi_{1-x}Mn_xO_3$ with 1.3 at% Mn ($r_{Mn^{2+}}$ = 97(81) pm and $r_{Mn^{3+}}$ = 78.5(72) pm for high (low) spin), the Curie temperature decreases to 383 K [61]. In the case of Cu^{2+} ($r_{Cu^{2+}}$=87 pm) doping on the B site, as shown in Fig. 4, we observed a decrease of both T_C and $T_{O\text{-}T}$ for doping levels from 0.4 to 1.6 at%. The lower permittivity of the pure $BaTiO_3$ sample compared to the 0.4 at%Cu-doped sample is due [62,63] to the lower grain size of the pure $BaTiO_3$ sample (< 1μm, measured by SEM) compared to the 0.4 at%Cu-doped sample (tens of μm). The doping-induced decrease of the permittivity is therefore over-compensated in the doped sample by the larger grain size.

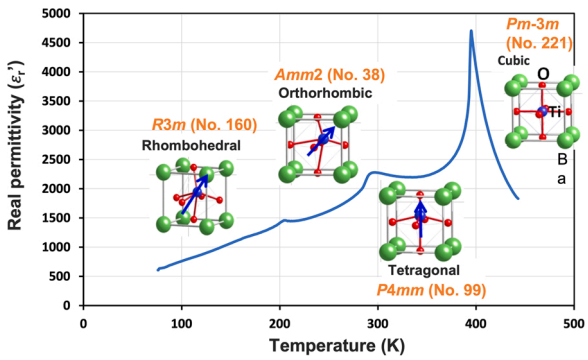

Fig. 3. A real part of the relative permittivity of $BaTiO_3$ as function of temperature. The insets depict the unit cell, its space group and crystalline systems together with a representation of the polarisation direction.

The destabilisation of the tetragonal phase occurs as well when smaller ions substitute on the B-site. Doping with smaller ions such as Al^{3+} ($r_{Al^{3+}}$=67.5 pm) on the B site, the octahedra around the dopant shrink and the movement of Ti ions along the ⟨100⟩ axes is hindered as a consequence. For example, $BaTi_{0.9992}Al_{0.0008}O_3$ has a slightly lower T_C of 390 K and an increased $T_{O\text{-}T}$ of 324 K compared to pure $BaTiO_3$ [64].

In summary, the domain walls movement significantly affect the dielectric properties of $BaTiO_3$ ceramics. Donor doping increases the domain walls mobility and permittivity increases as a consequence. Oppositely, the hardening mechanism of acceptor doping impedes domain rotation, resulting in the decrease of permittivity. In addition, oxygen vacancies induced by acceptor doping and electrons induced by donor doping both contribute to conduction. Dielectric losses increase as a consequence. Due to the different ionic radii between dopants and host ions, distortion of oxygen octahedra in the lattice are induced and displacements of Ti ions along ⟨100⟩ axis are reduced. Consequently, the Curie temperatures of doped-$BaTiO_3$ are shifted to lower temperatures and the tetragonal phase is destabilized.

3. Changing ferroelectric properties

3.1. Softening or hardening ceramics

The hysteresis loop (P-E loop) is the defining characteristic of ferroelectric materials. It presents the polarisation response to an external electric field. Fig. 5 shows the hysteresis loop of pure $BaTiO_3$ ceramics with schematics of the corresponding domains arrangements.

After sintering, $BaTiO_3$ ceramics exhibit a zero net polarisation, due to the random orientation of the ferroelectric domains. Upon increasing external electric field, domains gradually align through domain walls movement. The polarisation gradually increases and then saturates (up to P_s) under high fields. Upon removal of the external field, not all domains switch back to their original orientation, resulting in a remanent polarisation (P_r) in the ceramic. The area decorated by diagonal stripes in Fig. 5 represents the recoverable energy (W_{reco}). It corresponds to the total electric energy brought to the system minus the part used in the polarisation process of the ceramic, represented by the solid blue area inside the hysteresis loop.

Ferroelectrics have higher saturation polarisations and breakdown strengths than other bulk dielectric ceramics [7,65], which are beneficial to the total stored energy (W_{total}, solid blue area in Fig. 5). However, their W_{reco} is lower due to the high value of the remanent polarisation. Doping can be used to decrease the remanent polarisation while keeping a high saturation polarisation, thereby decreasing the hysteresis losses (or increasing W_{reco}) while keeping a high W_{total} [66].

Donor-doping presents the advantages of “soft” materials: higher domain-wall mobility, slimmer hysteresis loops, lower coercive fields, all contributing to the decrease of energy losses and therefore to the increase of W_{reco} [67–69] Through the volume effect, acceptor doping not only “hardens” ferroelectrics with decreased domain-wall mobility but can also result in pinched hysteresis loops. The resulting lower remanent polarisation, higher coercive field, and lower saturation polarisation [70,71] of such double loops compared to the open loop of pure $BaTiO_3$ are illustrated in Fig. 6 for Cu-doped $BaTiO_3$. Significantly, the much smaller remanent polarisation increases W_{reco} despite a small decrease of the saturation polarisation.[66,72] At thermodynamic equilibrium, the defect dipoles created by acceptor doping are aligned with the crystal symmetry (insert for state 1 in Fig. 6), a feature described by the symmetry-conforming principle [33]. The orientation of the defect dipoles is not modified by the application of the electric field[30,45] as it would necessitate the diffusion of the oxygen vacancies from one site to another [12]. The random distribution of defect dipoles

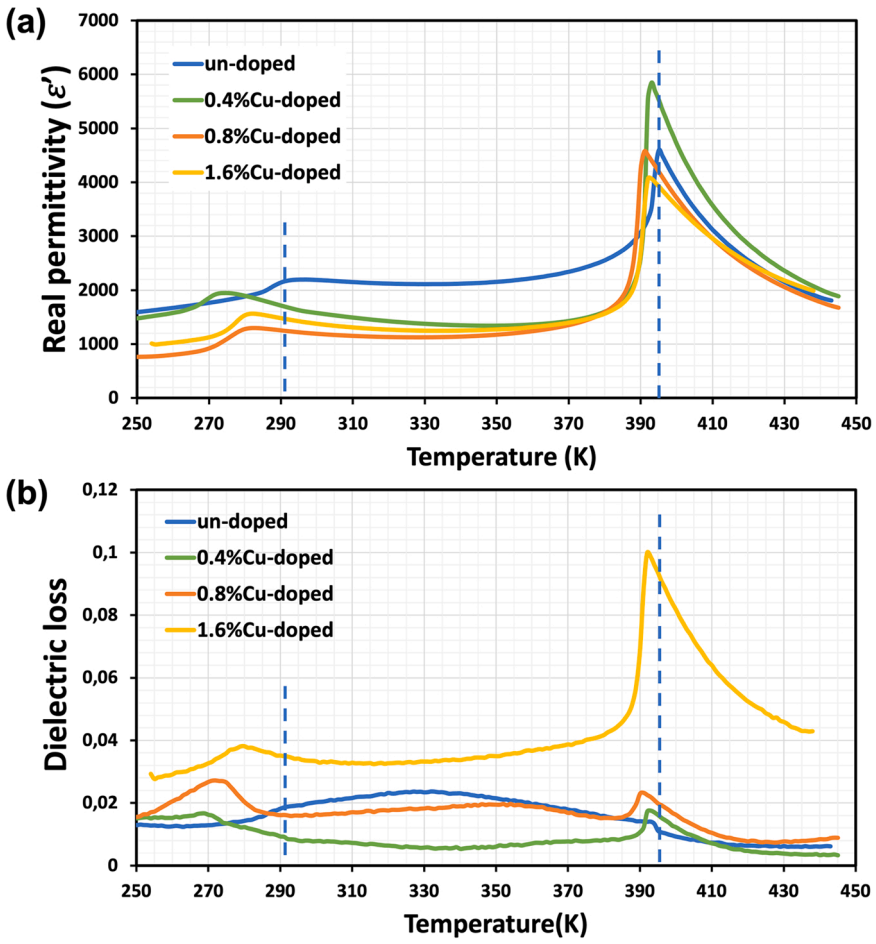

Fig. 4. Doping effect on the real part of the relative permittivity (a) and dielectric losses (b) of Cu-doped $BaTiO_3$ with different doping concentration (at 10 kHz) as function of temperature, compared to the un-doped $BaTiO_3$.

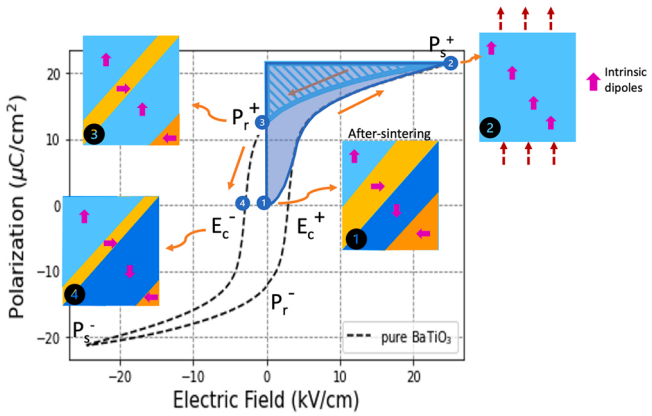

Fig. 5. Hysteresis loop of pure $BaTiO_3$ at room temperature with corresponding dipoles orientation (inserts). The initially randomly-oriented dipoles are gradually aligned by the increasing external electric field. $BaTiO_3$ goes from state 1 ("virgin" state) to state 2 (polarised state). Under removal of the field, dipoles partially switch back (state 3 with remanent polarisation P_r^+). At the coercive field (E_c^-) the orientations of the dipoles cancel each other. The total stored energy (W_{total}) is presented by solid blue area and the diagonal-stripe area corresponds to the recoverable energy (W_{reco}).

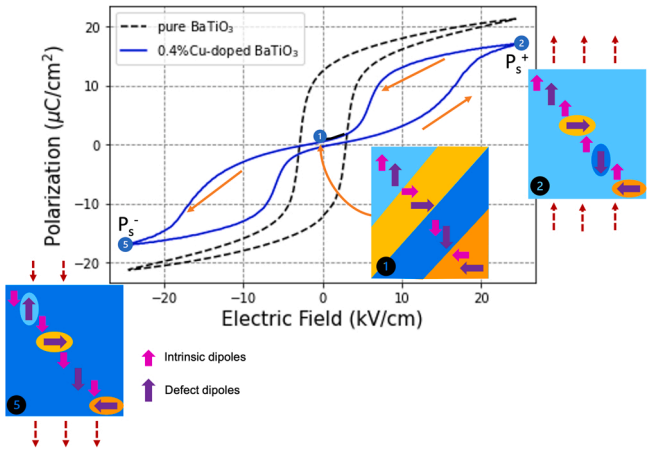

Fig. 6. Hysteresis loop pinching process for 0.4 at%Cu-doped $BaTiO_3$ (solid blue line) compared to the open loop of pure $BaTiO_3$ (dotted black line) at room temperature. The positive electric field gradually aligns the intrinsic dipoles and moves the domain walls except around the defect dipoles, as shown from state 1 to state 2. When the external field is removed, the defect dipoles produce a restoring force that switches intrinsic dipoles back to their initially random orientations and ceramics have a near zero net polarisation. The same behavior happens under the negative electric field (between state 1 and state 5).

produces a restoring force that accelerates the domain back-switching to their original state (state 1) in which the ceramics have a zero net polarisation.[7,22] The resulting pinching of the hysteresis loop enhances W_{reco}.

Hence, both the slimmer hysteresis loops caused by donor doping or the pinched hysteresis loops induced by acceptor doping are promising methods to increase the recoverable stored energy in doped-ferroelectric ceramics [66,72].

3.2. De-aging and re-aging

The hysteresis loop pinching process is also called aging, which is different from degradation. Degradation is an irreversible exhaustion-type process characterised by decreasing spontaneous and saturation polarisations values [73]. On the contrary, ageing is a reversible process [66,74,75].

The reverse process, de-aging, corresponds to the re-opening of a pinched hysteresis loop. A de-aged sample exhibits a classical ferroelectric P-E loop. This transformation from pinched to open loop (de-aging) is also referred to as from "clamped" to "free" [76] or "unclamped" [77]. As oxygen vacancies migrate and disorder, the defect dipoles temporarily disappear [78–80]. Domains are therefore released, resulting in the de-aging process. Two methods can be used to de-age an aged sample (i.e. to open pinched loops): quenching and fatigue treatment.

Quenching consists in heating the sample in its paraelectric phase (over the Curie temperature), where intrinsic dipoles do not exist and oxygen vacancies are disordered (i.e. are not necessarily nearest-neighbors to dopants) before quickly cooling the sample to room temperature. After quenching, defect dipoles are not immediately created as the oxygen vacancies need time to diffuse to positions nearest-neighbor to dopants. The ferroelectric domains are therefore not pinned by the defect dipoles and the hysteresis loop is akin to the one of an un-doped sample. Fig. 7(a) illustrates this for Cu-doped $BaTiO_3$ ceramics quenched in water: the sample initially exhibits a zero polarisation (consistent with a "virgin" state where the intrinsic dipoles are randomly oriented) before an open and symmetric hysteresis loop is measured. The result of this quenching procedure depends however on the thermal conductivity of the cooling environment: for example partially pinched loops were observed in $Pb(Zr_{0.58}Ti_{0.42})O_3$ cooled in air whereas totally open loops were observed when cooled in water [3].

The other procedure to open a pinched loop is the fatigue treatment where an oscillating electric field is applied numerous times on the sample. As a result, oxygen vacancies disorder, causing the defect dipoles to disappear. As shown in Fig. 7(b), the remanent polarisation of 0.4 at%Cu-doped $BaTiO_3$ increases from the first to the 10^3 cycles (from black curve to green curve) and the hysteresis loop is fully open after 10^5 cycles (red curve). The fatigue characteristics depend on the nature of the ferroelectric material itself, the type of dopants and their concentration, the temperature, and the field profile, among other parameters [81–84,85].

If a pinched loop can be opened, the inverse is also possible: it is called re-aging. As shown in Fig. 8 a 0.4 at%Cu-doped $BaTiO_3$ sample

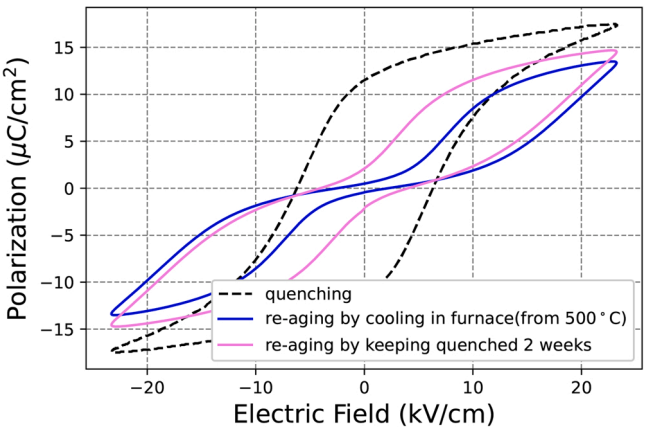

Fig. 8. Re-pinched hysteresis loops of 0.4 at%Cu-doped $BaTiO_3$. The open loop ("quenching", dotted black curve) is measured immediately after quenching the sample from above T_C and results from the disordering of the oxygen vacancies. Keeping this quenched sample for two weeks at room temperature, the disordered oxygen vacancies diffuse to positions nearest-neighbor to dopants, which forms defect dipoles and pinches the hysteresis loop (violet curve). Cooling the sample from 500° C (over T_C) in air also gives enough time for the diffusion of oxygen vacancies and the formation of defect dipoles, pinching the hysteresis loop (blue curve) as a consequence.

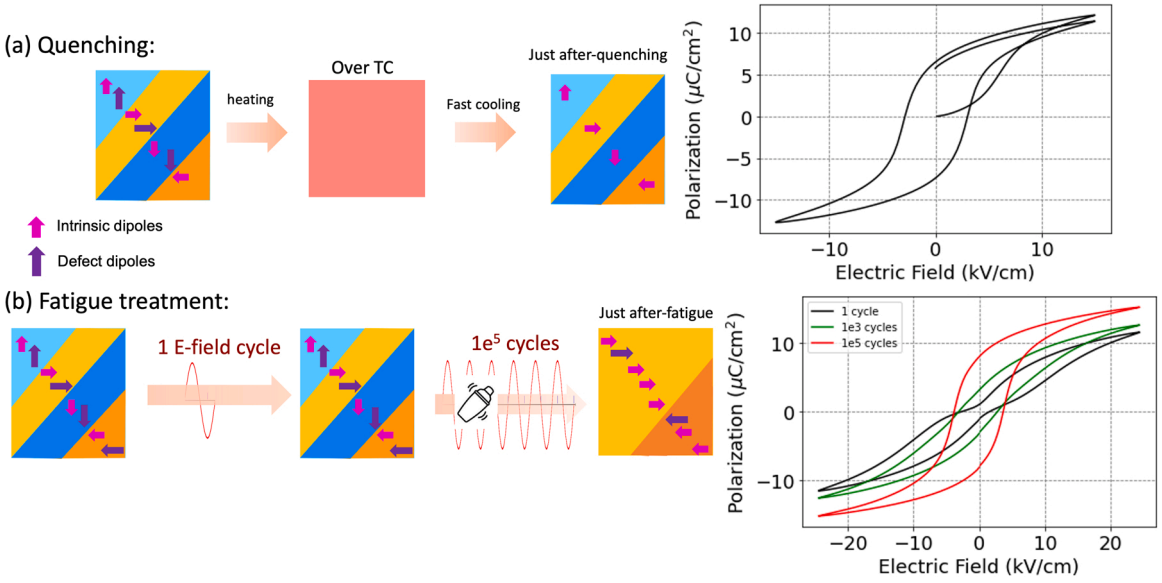

Fig. 7. De-aging processes of a 0.4 at%Cu-doped $BaTiO_3$ ceramic: (a) Only intrinsic dipoles exist after quenching and the hysteresis loop is open, starting from a "virgin" state with zero net polarisation, (b) Fatigue treatment randomizes the dipoles in the direction of external fields and defect dipoles are almost eliminated due to disordered oxygen vacancies; the pinched hysteresis loop (black curve) gradually opens (green curve) before reaching a stable open shape after 10^5 cycles (red curve).

exhibits a pinched hysteresis loop once thermodynamic equilibrium is reached, i.e. when oxygen vacancies have had enough time to reach positions that are nearest neighbor to dopants, forming defect dipoles. The re-aging process not only involves the nucleation and growth of domains [75], but is also driven by the reorientation of defect dipoles. Hence, the ability to re-age doped ferroelectrics depends on the type of dopants, their concentration, and thermal activation [86,87].

3.3. Shifting hysteresis loop

Hysteresis loops of doped ferroelectrics are sometimes shifted along the field axis, as shown in Fig. 9(a) where the negative coercive field is larger than the positive one ($|E_c^-| > E_c^+$). This phenomenon is related to the preferential orientation of the defect dipoles that pin the surrounding intrinsic dipoles alongside them. The preferential orientation of defects dipoles acts as an effective internal bias field [31,88]. As a consequence, a larger opposite external field is needed to switch the polarisation, thereby increasing the corresponding coercive field and shifting the whole hysteresis loop horizontally (Fig. 9(a)) [3,88]. Such a shift can be induced through a field-cooling procedure (polarizing ceramic from high temperature (over T_C) to room temperature) in order to align the intrinsic domains. According to the symmetry-conforming defect principle, once equilibrium is reached, the defect dipoles are aligned as well. This is illustrated by the schematics in Fig. 9.

The effect of field cooling is evidenced by the non-zero initial polarisation, almost equal to the remanent polarisation. As the defect dipoles eventually point along the direction the field was applied during field-cooling, they do not provide a perpendicular restoring force. As a consequence, the polarisation loop measured along that direction is not pinched. However, in the direction perpendicular to the poling field direction (Fig. 9(b)), the initial polarisation is almost zero. This is because few intrinsic dipoles point perpendicularly to the direction of the poling field. And for those who do, they have a random orientation in that plane. What is more, the few defect dipoles present in that plane adopt a random orientation through the symmetry conforming principle, resulting in the slight pinching of the hysteresis loop measured in that plane. A reduced saturation polarisation is also measured as the majority of defect dipoles still point along the poling direction and therefore hinder the rotation of their surrounding (intrinsic) domains to follow the applied field.

Several days after the field-cooling procedure, the shifted hysteresis loop gets further distorted. An hummingbird-like loop eventually appears, as shown in Fig. 10. This is ascribed to the increasing amount of polarised defect dipoles (reaching an equilibrium configuration) leading

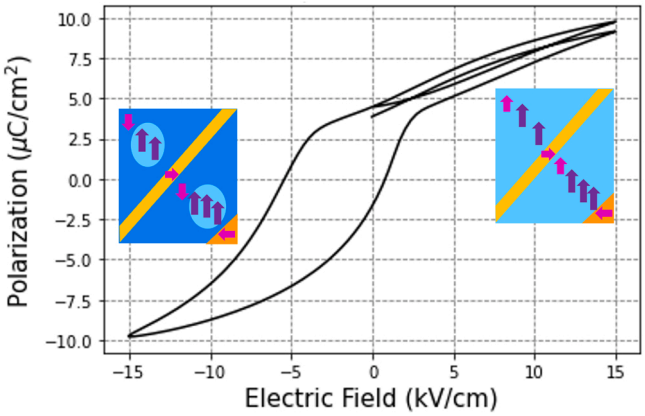

Fig. 10. Humming-bird-like hysteresis loop for 0.4 at%Cu-doped $BaTiO_3$ caused by the preferential orientation of defect dipoles. Under positive electric field (majority orientation of defect dipoles), domains rotation is easy (small E_c) with low hysteresis loss. Under reverse electric field, domain reversal is sluggish with larger hysteresis losses and higher coercive field.

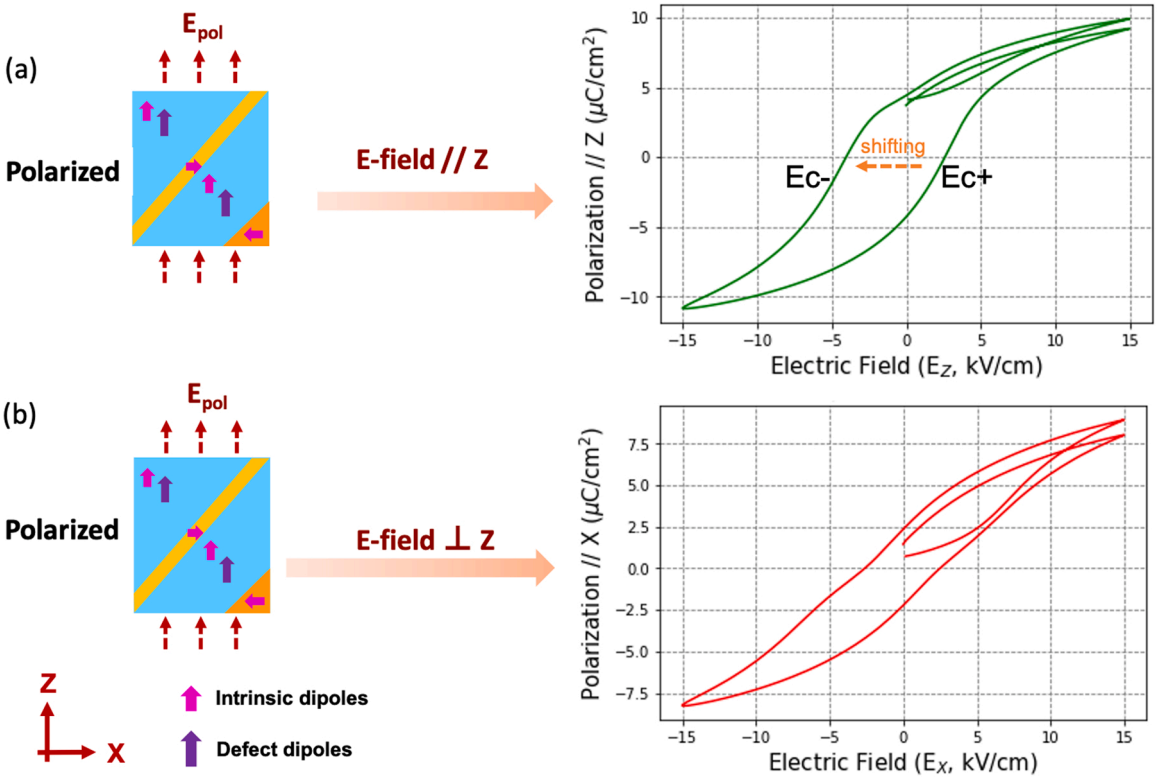

Fig. 9. Hysteresis loops of field-cooled 0.4 at%Cu-doped $BaTiO_3$ measured (a) along the direction of the poling field (E_{pol}) and (b) along an orthogonal direction. Preferentially-oriented defect dipoles (a) shift the hysteresis loop along the poling field axis and (b) cause a slight pinching of the hysteresis loop measured with a measuring field along an orthogonal direction.

to stronger pinning effect of the surrounding domains. Such loop is characterised by an asymmetry with the "beak" indicating the majority orientation of the defect dipoles. Under positive electric field (i.e. along defect dipoles majority orientation) domains rotation is facilitated, resulting in a smaller value of the coercive field and reduced hysteresis losses. Under reverse electric field, domain reversal is sluggish with larger hysteresis losses and requires a higher coercive field value.

In summary, the shape of the hysteresis loop can be manipulated through the control of defect dipoles. A pinched loop is induced when the oxygen vacancies are nearest-neighbors to aliovalent dopants, thereby creating defect dipoles. These defect dipoles provide a restoring force pinching the hysteresis or even inducing a double hysteresis loop akin the ones of antiferroelectrics. The sample nevertheless remains ferroelectric as the low field state is similar to the "virgin state" of undoped samples after synthesis. Such pinched hysteresis is beneficial, e.g. for energy-storage properties.[66,72].

A classical, open, ferroelectric hysteresis loop can nevertheless be induced in such samples by disordering the oxygen vacancies. This can be achieved immediately after having quenched the sample from its paraelectric phase to room temperature or through fatigue measurements. The induced states (akin to classical ferroelectrics) are nevertheless only metastable and will lead, at thermodynamic equilibrium, to a pinched loop once the oxygen vacancies have had the time to reach positions nearest-neighbor to dopants and form defect dipoles.

In addition to a shape change of the hysteresis loops, doping can also shift the hysteresis loops along the field axis. This shift is due to the internal bias field induced by a preferential orientation of the defect dipoles. Such effect is exacerbated when the sample is poled through field cooling, thereby aligning the majority of the intrinsic dipoles. When thermodynamic equilibrium is reached, most defect dipoles align with the polarised ferroelectric domains and a hummingbird-like hysteresis is generated, with the "beak" along the direction of the majority defect dipoles.

4. Changing electromechanical properties

Doping can also influence the piezoelectric properties of $BaTiO_3$. The contributions to strain-electric field relationship are a very complex problem. Apart from the intrinsic lattice strain, domain walls movement account for as much as 50% of the electromechanical effect on ferroelectric materials.[89,90] In addition, large nonlinear and recoverable electrostrains are most often experimentally observed due to the existence of non-180° domain walls [1,22,91,92]. Thus, the factors affecting the domain walls motions have a major influence over the electromechanical response of $BaTiO_3$. These factors include the symmetry of the crystal structure, dopants, defects, local variations in the composition, and external excitations such as temperature and electric field [93,94].

Compared to the pinned domain walls in "hard" ferroelectric, "soft" ferroelectrics have more mobile domain walls that result in higher electric-field-induced strain [23,25,93,95]. As shown in Table 1, the "soft" lead zirconate titanate (PZT-5A, PZT-5 H) ceramics have larger piezoelectric coefficients than the "hard" PZT (unaged) [96]. Unaged "hard" Ce-doped $BaTiO_3$ exhibits a lower piezoelectric coefficient than pure $BaTiO_3$ (d_{33} = 190 pm V^{-1}) [17,28].

As shown before, the defect dipoles in the aged state provide a restoring force that eases the domain rotation back to the zero net polarization (virgin) state, pinching the hysteresis loop. Consequently, the apparent piezoelectric coefficient (d_{33}) is drastically increased [13,17,88]. As shown in Fig. 11, the slope of the strain response of 0.4 at% Cu-doped $BaTiO_3$ corresponds to a very large piezoelectric coefficient (d_{33}) of 1561 pm V^{-1} for electric fields in the range of 5–8 kV cm^{-1}. Similarly, a d_{33} of 2100 pm V^{-1} for electric fields from 2.5 to 3.5 kV cm^{-1} has been reported for aged $BaTiO_3$ doped with 0.3 at%Mn. Single crystals of aged 0.02 at%Fe-doped $BaTiO_3$ also present large strain (7.5×10^{-3}) at low electric field (2 kV cm^{-1}), corresponding to a d_{33} of 3750 pm V^{-1} [88] about 10 times larger than conventional piezoelectric PZT (see Table 1) and $Pb(Zn_{1/3},Nb_{2/3})O_3$–8 % $PbTiO_3$ (PZN-PT) ceramics [97].

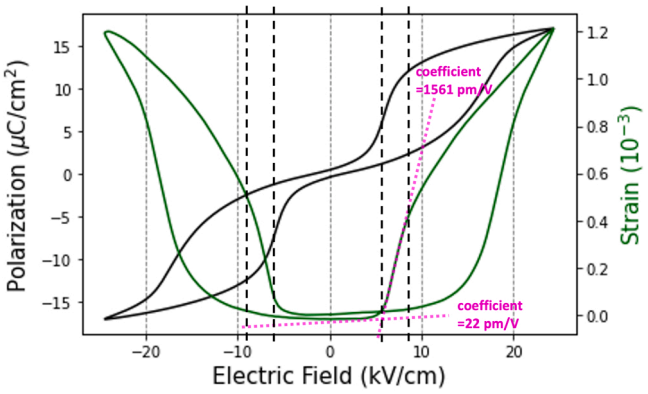

Fig. 11. The polarisation hysteresis loop and strain vs electric field curve of 0.4 at%Cu-doped $BaTiO_3$. In the lower field range (0 - 5 kV cm^{-1} or −5 - 0 kV cm^{-1}), the strain curve is almost flat with a corresponding piezoelectric coefficient of 22 pm V^{-1}. With decreasing electric field from 8(−8) to 5(−5) kV cm^{-1},, strain drastically and linearly decreases with a piezoelectric coefficient of about 1561 pm V^{-1}.

In summary, the enhanced mobility of domain walls enhances the piezoelectric properties of "soft" ferroelectrics compared to their undoped counterparts. In aged hard ferroelectrics the restoring force induced by the defect dipoles accelerates the domain rotation back to their initial orientation. As a result, the piezoelectric coefficients of aged $BaTiO_3$ are significantly increased, reaching values over 1500 pm V^{-1} (this work and Refs. [14,88]). This defect dipoles-domains interaction created by acceptor doping provides a promising method to realize applications based on enhanced electromechanical properties of $BaTiO_3$.

5. Conclusion

Doping provides a promising opportunity to tune the dielectric, ferroelectric, and piezoelectric properties of environmentally-friendly $BaTiO_3$ ceramics.

Because of the different ionic radii between dopants and host ions, the oxygen octahedra of the perovskite structure distort and the displacement of Ti ions along the ⟨100⟩ axis is affected, which results in the destabilization of the tetragonal phase and a decrease of the Curie temperature compared to pure $BaTiO_3$.

Donor doping improves the mobility of domain walls and $BaTiO_3$ is consequently "softened". The "softening" mechanism is ascribed to the reduced internal stress caused by Ba or Ti vacancies and to electron transfer between Ba and Ti vacancies [22–25,26]. Macroscopically, permittivity is increased and slimmer hysteresis loops with lower

Table 1
Comparison of piezoelectric coefficient (d_{33}) values between soft and hard ferroelectrics (PZT: lead zirconate titanate and BT: barium titanate) at room temperature.

Composition	Soft PZT		Hard PZT (unaged)			Hard BT (unaged)	Hard BT (aged)	
	PZT-5A	PZT-5 H	PZT-2	PZT-4	PZT-8	2 at%Ce	0.3 at%Mn	0.02 at%Fe
d_{33} (pm V^{-1})	375	590	152	290	225	116	2100	3750
Reference	[96]	[96]	[93]	[96]	[96]	[28]	[14]	[88]

coercive fields are measured, increasing the energy storage performance. Another advantage of "soft" materials is their higher piezoelectricity compared to un-doped counterparts.

For acceptor-doped $BaTiO_3$, the volume effect (defect-dipoles created by oxygen vacancies nearest-neighbors to dopants) as the primary hardening mechanism decreases mobility of domain walls, which has a contribution to decrease permittivity. According to the symmetry-conforming principle, the defect dipoles formed by oxygen vacancies accompanying acceptor dopants are aligned by crystal symmetry at thermodynamic equilibrium. Hence, aging process results in double hysteresis loops thereby increasing the recoverable energy storage. Through the control of the defect dipoles orientation, the shape of the hysteresis loop can be manipulated including pinching, opening, re-pinching, shifting, even distorting to a hummingbird-like hysteresis loop. Moreover, aged doped-$BaTiO_3$ shows higher piezoelectric coefficients due to the restoring force of the defect dipoles.

Declaration of Competing Interest

The authors declare that they have no known competing financial interests or personal relationships that could have appeared to influence the work reported in this paper.

References

[1] Malcolm E. Lines, Alastair M. Glass, Principles and Applications of Ferroelectrics and Related Materials, Oxford University Press,, 2001.
[2] SM Said, MFM Sabri, F. Salleh, Ferroelectr. their Appl. (2017).
[3] Dragan Damjanovic, Hysteresis in piezoelectric and ferroelectric materials, Sci. Hysteresis 3 (2006) 337–465.
[4] Irinela Chilibon, José N. Marat-Mendes, Ferroelectric ceramics by sol-gel methods and applications: a review, J. Sol. -gel Sci. Technol. 64 (3) (2012) 571–611.
[5] JF Scott, Appl. Mod. Ferroelectr. Sci. 315 (5814) (2007) 954–959.
[6] Letao Yang, Xi Kong, Fei Li, Hua Hao, Zhenxiang Cheng, Hanxing Liu, Jing-Feng Li, Shujun Zhang, Perovskite lead-free dielectrics for energy storage applications, Prog. Mater. Sci. 102 (2019) 72–108.
[7] Xihong Hao, A review on the dielectric materials for high energy-storage application, J. Adv. Dielectr. 3 (01) (2013), 1330001.
[8] Nava Setter, EL Colla, Ferroelectric Ceramics: Tutorial Reviews, Theory, Processing, and Applications, Springer, 1993.
[9] Jia Liu, Laijun Liu, Jiale Zhang, Li Jin, Dawei Wang, Jie Wei, Zuo-Guang Ye, Chun-Lin Jia, Charge effects in donor-doped perovskite ferroelectrics, J. Am. Ceram. Soc. 103 (9) (2020) 5392–5399.
[10] ColinL Freeman, James A. Dawson, Hung-Ru Chen, Liubin Ben, John H. Harding, Finlay D. Morrison, Derek C. Sinclair, Anthony R. West, Energetics of donor-doping, metal vacancies, and oxygen-loss in a-site rare-earth-doped batio3, Adv. Funct. Mater. 23 (31) (2013) 3925–3928.
[11] T. Sareein, P. Baipaywad, W. Chaiammad, A. Ngamjarurojana, S. Ananta, X. Tan, R. Yimnirun, Dielectric aging behavior in a-site hybrid-doped batio3 ceramics, Curr. Appl. Phys. 11 (3) (2011) S90–S94.
[12] Yuji Noguchi, Hiroki Matsuo, Yuuki Kitanaka, Masaru Miyayama, Ferroelectrics with a controlled oxygen-vacancy distribution by design, Sci. Rep. 9 (1) (2019) 1–10.
[13] Wenfeng Liu, Wei Chen, Liu Yang, Lixue Zhang, Yu Wang, Chao Zhou, Shengtao Li, Xiaobing Ren, Ferroelectric aging effect in hybrid-doped ba ti o 3 ceramics and the associated large recoverable electrostrain, Appl. Phys. Lett. 89 (17) (2006), 172908.
[14] LX Zhang, X. Ren, In situ observation of reversible domain switching in aged mn-doped batio 3 single crystals, Phys. Rev. B 71 (17) (2005), 174108.
[15] Da-Yong Lu, Xiu-Yun Sun, Masayuki Toda, A novel high-k -?y5v'barium titanate ceramics co-doped with lanthanum and cerium, J. Phys. Chem. Solids 68 (4) (2007) 650–664.
[16] Chenjie Fu, Nan Chen, Guoping Du, Comparative studies of nickel doping effects at a and b sites of batio3 ceramics on their crystal structures and dielectric and ferroelectric properties, Ceram. Int. 43 (17) (2017) 15927–15931.
[17] Matias Acosta, N. Novak, V. Rojas, S. Patel, R. Vaish, J. Koruza, GA Rossetti Jr., J. Rödel, Batio3-based piezoelectrics: Fundamentals, current status, and perspectives, Appl. Phys. Rev. 4 (4) (2017), 041305.
[18] Fatin Adila Ismail, Rozana Aina Maulat Osman, Mohd Sobri Idris, Review on dielectric properties of rare earth doped barium titanate. AIP Conference Proceedings, volume 1756, AIP Publishing LLC,, 2016.
[19] Shenglan Hao, Minghai Yao, GaëlleVitali Derrien, Pascale Gemeiner, Mojca Otoničar, Pascal Ruello, Houssny Bouyanfif, Pierre-Eymeric Janolin, Brahim Dkhil, Charles Paillard, Optical absorption by design in a ferroelectric: co-doping in batio3, J. Mater. Chem. C. (2021).
[20] Chonghea Li, Xionggang Lu, Weizhong Ding, Liming Feng, Yonghui Gao, Ziming Guo, Formability of abx3 (x= f, cl, br, i) halide perovskites, Acta Crystallogr. Sect. B: Struct. Sci. 64 (6) (2008) 702–707.
[21] Robert D. Shannon, Revised effective ionic radii and systematic studies of interatomic distances in halides and chalcogenides, Acta Crystallogr. Sect. Acrystal Phys., Diffr., Theor. Gen. Crystallogr. 32 (5) (1976) 751–767.
[22] Dragan Damjanovic, Ferroelectric, dielectric and piezoelectric properties of ferroelectric thin films and ceramics, Rep. Prog. Phys. 61 (9) (1998) 1267.
[23] MI Morozov, D. Damjanovic, Charge migration in pb (zr, ti) o 3 ceramics and its relation to ageing, hardening, and softening, J. Appl. Phys. 107 (3) (2010), 034106.
[24] Robert Gerson, Variation in ferroelectric characteristics of lead zirconate titanate ceramics due to minor chemical modifications, J. Appl. Phys. 31 (1) (1960) 188–194.
[25] Lucien Eyraud, Benoit Guiffard, Laurent Lebrun, Daniel Guyomar, Interpretation of the softening effect in pzt ceramics near the morphotropic phase boundary, Ferroelectrics 330 (1) (2006) 51–60.
[26] J. Daniels, et al., Electr. Conduct. High. Temp. donor-doped barium Titan. Ceram. i (1976).
[27] M. Ganguly, SK Rout, TP Sinha, SK Sharma, HY Park, CW Ahn, IW Kim, Characterization and rietveld refinement of a-site deficient lanthanum doped barium titanate, J. Alloy. Compd. 579 (2013) 473–484.
[28] Chen Ang, Zhi Yu, Zhi Jing, Ruyan Guo, AS Bhalla, LE Cross, Piezoelectric and electrostrictive strain behavior of ce-doped batio 3 ceramics, Appl. Phys. Lett. 80 (18) (2002) 3424–3426.
[29] DM Smyth, Barium titanate, Defect Chem. Met. Oxides (2000) 253–282.
[30] Lixue Zhang, Emre Erdem, Xiaobing Ren, Rüdiger-A. Eichel, Reorientation of (mn ti - vö) × defect dipoles in acceptor-modified batio 3 single crystals: An electron paramagnetic resonance study, Appl. Phys. Lett. 93 (20) (2008), 202901.
[31] KHHK Carl, KH Hardtl, Electrical after-effects in pb (ti, zr) o3 ceramics, Ferroelectrics 17 (1) (1977) 473–486.
[32] G. Arlt, H. Neumann, Internal bias in ferroelectric ceramics: origin and time dependence, Ferroelectrics 87 (1) (1988) 109–120.
[33] Xiaobing Ren, Giant electric-field induced strain in ferroelectric crystals by point-defect mediated reversible domain switching, APS March Meet. Abstr. 2004 (2004) pages W19-005.
[34] Xiaobing Ren, Kazuhiro Otsuka, Universal symmetry property of point defects in crystals, Phys. Rev. Lett. 85 (5) (2000) 1016.
[35] PV Lambeck, GH Jonker, The nature of domain stabilization in ferroelectric perovskites, J. Phys. Chem. Solids 47 (5) (1986) 453–461.
[36] Rüdiger-A. Eichel, Defect structure of oxide ferroelectrics-?valence state, site of incorporation, mechanisms of charge compensation and internal bias fields, J. Electroceram. 19 (1) (2007) 11–23.
[37] Yuri A. Genenko, Julia Glaum, Michael J. Hoffmann, Karsten Albe, Mechanisms of aging and fatigue in ferroelectrics, Mater. Sci. Eng.: B 192 (2015) 52–82.
[38] HL Stadler, Etched hillocks in batio3, J. Appl. Phys. 34 (3) (1963) 570–573.
[39] Lixue Zhang, Xiaobing Ren, Aging behavior in single-domain mn-doped batio 3 crystals: implication for a unified microscopic explanation of ferroelectric aging, Phys. Rev. B 73 (9) (2006), 094121.
[40] QM Zhang, Haimin Wang, N. Kim, LE Cross, Direct evaluation of domain-wall and intrinsic contributions to the dielectric and piezoelectric response and their temperature dependence on lead zirconate-titanate ceramics, J. Appl. Phys. 75 (1) (1994) 454–459.
[41] Zhonghua Yao, Hanxing Liu, Yan Liu, Zhaohui Wu, Zongyang Shen, Yang Liu, Minghe Cao, Structure and dielectric behavior of nd-doped batio3 perovskites, Mater. Chem. Phys. 109 (2–3) (2008) 475–481.
[42] Janusz Nowotny, Mieczyslaw Rekas, Defect structure, electrical properties and transport in barium titanate. vii. chemical diffusion in nb-doped batio3, Ceram. Int. 20 (4) (1994) 265–275.
[43] Helen M. Chan, MARTIN R HARMER, and DONALD ML SMYTH. Compensating defects in highly donor-doped batio3, J. Am. Ceram. Soc. 69 (6) (1986) 507–510.
[44] Qiaomei Sun, Qilin Gu, Kongjun Zhu, Rongying Jin, Jinsong Liu, Jing Wang, Jinhao Qiu, Crystalline structure, defect chemistry and room temperature colossal permittivity of nd-doped barium titanate, Sci. Rep. 7 (2017) 42274.
[45] Jiandang Liu, L. Jin, Z. Jiang, Laijun Liu, L. Himanen, J. Wei, Nan Zhang, Dawei Wang, C.-L. Jia, Understanding doped perovskite ferroelectrics with defective dipole model, J. Chem. Phys. 149 (24) (2018), 244122.
[46] Anthony R. West, Timothy B. Adams, Finlay D. Morrison, Derek C. Sinclair, Novel high capacitance materials:-batio3: La and cacu3ti4o12, J. Eur. Ceram. Soc. 24 (6) (2004) 1439–1448.
[47] Vincenzo Buscaglia, Maria Teresa Buscaglia, Giovanna Canu, Batio3-Based Ceram.: Fundam., Prop. Appl. (2020).
[48] Jung-Kun Lee, Kug-Sun Hong, Jin-Wook Jang, Roles of ba/ti ratios in the dielectric properties of batio3 ceramics, J. Am. Ceram. Soc. 84 (9) (2001) 2001–2006.
[49] NV Dang, TD Thanh, LV Hong, VD Lam, The-Long Phan, Structural, optical and magnetic properties of polycrystalline bati1- xfexo3 ceramics, J. Appl. Phys. 110 (4) (2011), 043914.
[50] Tao Li, Kun Yang, Renzhong Xue, Yuncai Xue, Zhenping Chen, The effect of cuo doping on the microstructures and dielectric properties of batio 3 ceramics, J. Mater. Sci.: Mater. Electron. 22 (7) (2011) 838–842.
[51] C.Meric Guvenc, Umut Adem, Influence of aging on electrocaloric effect in li. doped batio3 ceramics, J. Alloy. Compd. 791 (2019) 674–680.
[52] H.-J. Hagemann, Loss mechanisms and domain stabilisation in doped batio3, J. Phys. C: Solid State Phys. 11 (15) (1978) 3333.
[53] Kang Yan, Fangfang Wang, Dawei Wu, Xiaobing Ren, Kongjun Zhu, Ferroelectric aging effects and large recoverable electrostrain in ceria-doped batio3 ceramics, J. Am. Ceram. Soc. 102 (5) (2019) 2611–2618.
[54] AC Caballero, JF Fernandez, C. Moure, P. Duran, Zno-doped batio3: microstructure and electrical properties, J. Eur. Ceram. Soc. 17 (4) (1997) 513–523.

[55] A. Salhi, S. Sayouri, A. Alimoussa, L. Kadira, Impedance spectroscopy analysis of ca doped batio3 ferroelectric ceramic manufactured with a new synthesis technique, Mater. Today.: Proc. 13 (2019) 1248–1258.
[56] I.-K. Jeong, Seunghun Lee, Se-Young Jeong, CJ Won, N. Hur, A. Llobet, Structural evolution across the insulator-metal transition in oxygen-deficient batio 3- δ studied using neutron total scattering and rietveld analysis, Phys. Rev. B 84 (6) (2011), 064125.
[57] Shuangyi Liu, Limin Huang, Jackie Li, Stephen O'Brien, Intrinsic dielectric frequency dependent spectrum of a single domain tetragonal batio3, J. Appl. Phys. 112 (1) (2012), 014108.
[58] JN Lin, TB Wu, Effects of isovalent substitutions on lattice softening and transition character of batio3 solid solutions, J. Appl. Phys. 68 (3) (1990) 985–993.
[59] Sabina Yasmm, Shamima Choudhury, MA Hakim, AH Bhuiyan, MJ Rahman, Effect of cerium doping on microstructure and dielectric properties of batio3 ceramics, J. Mater. Sci. Technol. 27 (8) (2011) 759–763.
[60] Wei-Gang Yang, Bo-Ping Zhang, Nan Ma, Lei Zhao, High piezoelectric properties of batio3-xlif ceramics sintered at low temperatures, J. Eur. Ceram. Soc. 32 (4) (2012) 899–904.
[61] Wei Chen, Xia Zhao, Jingen Sun, Lixue Zhang, Lisheng Zhong, Effect of the mn doping concentration on the dielectric and ferroelectric properties of different-routes-fabricated batio3-based ceramics, J. Alloy. Compd. 670 (2016) 48–54.
[62] Jan Petzelt, Dielectric grain-size effect in high-permittivity ceramics, Ferroelectrics 400 (1) (2010) 117–134.
[63] Y. Tan, J. Zhang, Y. Wu, C. Wang, V. Koval, B. Shi, H. Ye, R. McKinnon, G. Viola, H. Yan, Sci. Rep. 5 (2015) 9953.
[64] K. Vani, Viswanathan Kumar, Evolution of dielectric and ferroelectric relaxor states in al3.-doped batio3, AIP Adv. 5 (2) (2015), 027135.
[65] Mahesh Peddigari, Haribabu Palneedi, Geon-Tae Hwang, Jungho Ryu, Linear and nonlinear dielectric ceramics for high-power energy storage capacitor applications, J. Korean Ceram. Soc. 56 (1) (2019) 1–23.
[66] Zhiyang Wang, Deqing Xue, Yumei Zhou, Nan Wang, Xiangdong Ding, Jun Sun, Turab Lookman, Dezhen Xue, Enhanced energy-storage density by reversible domain switching in acceptor-doped ferroelectrics, Phys. Rev. Appl. 15 (3) (2021), 034061.
[67] Bin Peng, Zhenkun Xie, Zhenxing Yue, Longtu Li, Improvement of the recoverable energy storage density and efficiency by utilizing the linear dielectric response in ferroelectric capacitors, Appl. Phys. Lett. 105 (5) (2014), 052904.
[68] Mao Ye, Qiu Sun, Xiangqun Chen, Zhaohua Jiang, Fuping Wang, Effect of eu doping on the electrical properties and energy storage performance of pbzro 3 antiferroelectric thin films, J. Am. Ceram. Soc. 94 (10) (2011) 3234–3236.
[69] Venkata Sreenivas Puli, Patrick Li, Shiva Adireddy, Douglas B. Chrisey, Crystal structure, dielectric, ferroelectric and energy storage properties of la-doped batio 3 semiconducting ceramics, J. Adv. Dielectr. 5 (03) (2015), 1550027.
[70] YY Guo, MH Qin, T. Wei, KF Wang, J.-M. Liu, Kinetics controlled aging effect of ferroelectricity in al-doped and ga-doped batio 3, Appl. Phys. Lett. 97 (11) (2010), 112906.
[71] Mohamad M. Ahmad, Koji Yamada, Paul Meuffels, Rainer Waser, Aging-induced dielectric relaxation in barium titanate ceramics, Appl. Phys. Lett. 90 (11) (2007), 112902.
[72] Zechao LI, Shenglan HAO, Eva HERIPRE, and Pierre-Eymeric JANOLIN. Improvement of energy storage of ferroelectric by defect dipoles configuration. unpublished, 2021.
[73] Methee Promsawat, Marco Deluca, Sirirat Kampoosiri, Boonruang Marungsri, Soodkhet Pojprapai, Electrical fatigue behavior of lead zirconate titanate ceramic under elevated temperatures, J. Eur. Ceram. Soc. 37 (5) (2017) 2047–2055.
[74] Yingying Zhao, Jiping Wang, Lixue Zhang, Chenchen Wang, Shujuan Liu, Aging rate of cerium doped ba (ti0. 99mn0. 01) o3, Ceram. Int. 43 (2017) S70–S74.
[75] RC Bradt, GS Ansell, Aging in tetragonal ferroelectric barium titanate, J. Am. Ceram. Soc. 52 (4) (1969) 192–198.
[76] KnW Plessner, Ageing of the dielectric properties of barium titanate ceramics, Proc. Phys. Soc. Sect. B 69 (12) (1956) 1261.
[77] AF Devonshire, Theory of ferroelectrics, Adv. Phys. 3 (10) (1954) 85–130.
[78] WL Warren, D. Dimos, GE Pike, K. Vanheusden, R. Ramesh, Alignment of defect dipoles in polycrystalline ferroelectrics, Appl. Phys. Lett. 67 (12) (1995) 1689–1691.
[79] WL Warren, GE Pike, K. Vanheusden, D. Dimos, BA Tuttle, J. Robertson, Defect-dipole alignment and tetragonal strain in ferroelectrics, J. Appl. Phys. 79 (12) (1996) 9250–9257.
[80] William L. Warren, Karel Vanheusden, Duane Dimos, Gordon E. Pike, Bruce A. Tuttle, Oxygen vacancy motion in perovskite oxides, J. Am. Ceram. Soc. 79 (2) (1996) 536–538.
[81] JF Scott, Matthew Dawber, Oxygen-vacancy ordering as a fatigue mechanism in perovskite ferroelectrics, Appl. Phys. Lett. 76 (25) (2000) 3801–3803.
[82] Maxim I. Morozov, Dragan Damjanovic, Hardening-softening transition in fe-doped pb (zr, ti) o 3 ceramics and evolution of the third harmonic of the polarization response, J. Appl. Phys. 104 (3) (2008), 034107.
[83] LX Zhang, W. Chen, X. Ren, Large recoverable electrostrain in mn-doped (ba, sr) ti o 3 ceramics, Appl. Phys. Lett. 85 (23) (2004) 5658–5660.
[84] Julia Glaum, Torsten Granzow, Ljubomira Ana Schmitt, Hans-Joachim Kleebe, Jürgen Rödel, Temperature and driving field dependence of fatigue processes in pzt bulk ceramics, Acta Mater. 59 (15) (2011) 6083–6092.
[85] Nina Balke, Doru C. Lupascu, Torsten Granzow, Jürgen Rödel, Fatigue of lead zirconate titanate ceramics. i: Unipolar and dc loading, J. Am. Ceram. Soc. 90 (4) (2007) 1081–1087.
[86] U. Robels, G. Arlt, Domain wall clamping in ferroelectrics by orientation of defects, J. Appl. Phys. 73 (7) (1993) 3454–3460.
[87] Doru C. Lupascu, Yuri A. Genenko, Nina Balke, Aging in ferroelectrics, J. Am. Ceram. Soc. 89 (1) (2006) 224–229.
[88] Xiaobing Ren, Large electric-field-induced strain in ferroelectric crystals by point-defect-mediated reversible domain switching, Nat. Mater. 3 (2) (2004) 91–94.
[89] EI Bondarenko, Vyu Topolov, AV Turik, The role of 90 domain wall displacements in forming physical properties of perovskite ferroelectric ceramics, Ferroelectr. Lett. Sect. 13 (1) (1991) 13–19.
[90] Dragan Damjanovic, Marlyse Demartin, Contribution of the irreversible displacement of domain walls to the piezoelectric effect in barium titanate and lead zirconate titanate ceramics, J. Phys.: Condens. Matter 9 (23) (1997) 4943.
[91] Fei Li, Li Jin, Zhuo Xu, Shujun Zhang, Electrostrictive effect in ferroelectrics: An alternative approach to improve piezoelectricity, Appl. Phys. Rev. 1 (1) (2014), 011103.
[92] Takaaki Tsurumi, Yutaka Kumano, Naoki Ohashi, Tadashi Takenaka, Osamu Fukunaga, 90° domain reorientation and electric-field-induced strain of tetragonal lead zirconate titanate ceramics, Jpn. J. Appl. Phys. 36 (9S) (1997) 5970.
[93] Ting Zheng, Jiagang Wu, Dingquan Xiao, Jianguo Zhu, Recent development in lead-free perovskite piezoelectric bulk materials, Prog. Mater. Sci. 98 (2018) 552–624.
[94] Bastola Narayan, Jaskaran Singh Malhotra, Rishikesh Pandey, Krishna Yaddanapudi, Pavan Nukala, Brahim Dkhil, Anatoliy Senyshyn, Rajeev Ranjan, Electrostrain in excess of 1% in polycrystalline piezoelectrics, Nat. Mater. 17 (5) (2018) 427–431.
[95] Jaffe Hans, Piezoelectric ceramics, J. Am. Ceram. Soc. 41 (11) (1958) 494–498.
[96] Thomas R. Shrout, Shujun J. Zhang, Lead-free piezoelectric ceramics: alternatives for pzt? J. Electroceram. 19 (1) (2007) 113–126.
[97] Seung-Eek Park, Thomas R. Shrout, Ultrahigh strain and piezoelectric behavior in relaxor based ferroelectric single crystals, J. Appl. Phys. 82 (4) (1997) 1804–1811.

_____
_____